ABSTRACT

Title of dissertation: Air Bubble Entrainment by Breaking Bow Waves Simulated by a 2D+T Technique

Mohammadreza Tavakolinejad
Doctor of Philosophy, 2010

Dissertation directed by: Professor James H. Duncan
Department of Mechanical Engineering

Experimental studies of air entrainment by breaking bow waves are essential for advancing the understanding of these flows and creating valid models. This experimental research is part of a larger project whose broad goal is to improve our understanding of the dynamics of breaking bow waves including the entrainment of air bubbles into the flow and the generation of turbulence and vorticity. A mechanical wave maker creates waves similar to those formed at the bow of a moving ship, utilizing the 2D+T approximation. The primary mechanisms for air entrainment are the impact of the plunging wave jet and individual droplets in the splash region on the free surface. The air entrainment process is observed in small scale stationary model experiments, and the air bubbles are entrained in spatially periodic bubble clouds. The specific objectives of this project are to develop a shadowgraph technique for measurement of bubble size distributions and motions and to measure and analyze the void fraction as a function of the equivalent forward speed of the ship model. Three key bubble characteristics that will be emphasized

and studied in particular detail are bubble distributions and motions, void fractions and relationships between the properties of bubble and the geometrical characteristics of the wave. The air entrainment in ship bow waves simulated by a 2D+T technique and the methods used to analyze these phenomena are all novel aspects of this particular study and should provide a valuable set of data and analyses for the study of breaking bow wave mechanics.

Air Bubble Entrainment by Breaking Bow Waves Simulated by a 2D+T Technique

by

Mohammadreza Tavakolinejad

Dissertation submitted to the Faculty of the Graduate School of the
University of Maryland, College Park in partial fulfillment
of the requirements for the degree of
Doctor of Philosophy
2010

Advisory Committee:
Professor James H. Duncan, Chair/Advisor
Professor Kenneth Kiger
Professor Peter Bernard
Professor Elias Balaras
Professor Panagiotis Dimitrakopoulos

Dedication

To my parents

,

To Maryam for your understanding and support throughout

and

To our beloved son Amir Mehdi

Acknowledgments

I would like to express my deepest gratitude and sincere thanks to Dr. James H. Duncan for his encouragement, support and guidance during the course of this study. Over past several years, Dr. Duncan has shown many of the best academic qualities which I admire and respect deeply. He always offered good advice, wouldn't let me produce any work that wasn't excellent and gave me the space to make this project truly my own. I am deeply indebted to him for being able to reach this point. I would also like to thank Dr. Kenneth Kiger, Dr. Peter Bernard, Dr. Elias Balaras and Dr. Panagiotis Dimitrakopoulos for serving on my dissertation committee.

I am very grateful to my senior colleague Dr. Mostafa Shakeri who was instumental in making the 2D+T wave maker a reality and provided invaluable guidance and assistance. I also wish to thank my co-workers and colleagues in Hydrodynamics Lab, Dr. Eric Maxiener, Dr. Jamie Diorio, Dr. Xinan Liu, and Christine Ikeda. Every successful lab requires cooperation amongst its members, regardless of how inter-related their research is. It has been a lot of fun working with you.

Many thanks go out to my wife, Maryam, my son, Amir Mehdi, and our parents without whom I would never have been able to pursue this work.

Table of Contents

List of Figures

Chapter 1

Introduction

Ship bow waves have been an active area of research for many years. As the ship speed is increased, these waves begin to break at moderate speeds (about 16.5 knots in the present experiments) where they form splling breakers. The breakers become stronger as the ship speed is increased further and begin to plunge at high speeds (above about 22 knots in the present experiments). The strength of these plunging breakers also increases with futher increases in ship speed. Breaking bow waves are important in a number of ways. First, they cause a drag on the ship and this drag must, of course, be overcome by the ship's propulsion system. Second, large breaking waves such as these entrain air bubbles which create underwater sound. For naval ships, this sound is important because it can interfere with shipboard sonar systems and may be detectable by external sonar systems. Third, the breakers create bubbly wakes that extend far behind the ship. These bubbly flows are detectable by external active sonar systems and so make the ship vulnerable to attack. The white water, indicative of air bubble entrainment, in the flow field of a naval ship is shown in Figure 1.1.

In this study, we explore the generation of bubbles by breaking ship bow waves in a series of laboratory experiments. There are two main difficulties in designing these laboratory experiments. First, it is important that the experiments

Figure 1.1: Example of bow waves created by a US Navy Frigate.

be performed at relatively large scale. This is necessary since in order to entrain air and make bubbles that are similar to small scale, the water flow must have sufficient kinetic energy to overcome surface tension. In small scale, three-dimensional ship model testing, it is well know, that surface tension can make weak, non-entraining spilling breakers in the laboratory where at corresponding conditions in the field, the wave might create vigorous air entrainment. The second difficulty is that the experiments should be performed in water with sea salt concentrations similar to that found in the open ocean, about 35 parts per thousand. This is necessary because the presence of salt dramatically increases the number of small bubbles in an entrainment event. Salt water is corrosive and can easily damage laboratory equipment.

In this thesis, a series of experiments on the entrainment of air bubbles by breaking waves is described. The bow waves are simulated using a technique know as 2D+T (two dimensions plus time). In this technique, a wave maker with a

flexible surface (called the wave board) was programmed so that it created a time series of surface shapes that simulated the line of intersection between one side of the hull of a slender ship model moving at constant speed and an imaginary vertical plane oriented normal to the ship model track. This wave maker simulates a large three-dimensional ship model with a draft of 0.91 meters and a length of 21 m and produces waves with lengths for about 2 m, considerably larger than in typical ship model tests, even at the worlds largest ship model basins. Further, the wave tank in the present work was filled with artificial sea water at a salt concentration of 35 parts per thousand while almost all ship model basins are filled with fresh water.

The organization of this thesis is as follows. In Chapter 2, the literature on breaking waves and the associated air entrainment is reviewed. This review includes previous work on breaking bow waves as well as breaking waves in the open ocean and on beaches. The experimental setup and techniques employed in the present research are described in detail in Chapter 3 and 4, respectively. This is followed by a description and dicussion of the experimental results in Chapter 5. Finally, in Chapter 6, the conclusions of the study are given.

Chapter 2

Literature Review and Overview

There are two major types of breakers: plunging and spilling. The most dramatic breakers are plunging breakers. For these waves, the breaking commences when a forward-moving sheet of water, referred to as the jet, plunges down from the crest onto the front face of the wave causing splashing, air entrainment, and turbulence. In spilling breakers, turbulence appears spontaneously at the crest due to poorly understood mechanisms. This turbulent fluid then spills down the front face of the wave, entraining air and creating water drops as it spills. In waves with short wavelengths, surface tension tends to prevent drop and bubble formation. Waves can break in open deep water due to a variety of effects including inherent instabilities of deep water waves, wave-wave interaction, wave-current interaction, wind-wave interaction, or steepening due to external bodies such as ships. These latter breakers are somewhat simpler than wind waves since, in a calm sea, the forcing motion is well defined and there is no vorticity in the water except for that found in the breaking zone itself.

2.1 Wave Research

Research in the behaviour of non breaking waves has benefited from well-developed potential flow theories. Wave breaking, however, includes a highly com-

plex vortical fluid motion that cannot be adequately modeled with potential flow. There are no closed form analytical theories available to describe the flow, thus researchers have typically resorted to theoretical models and numerical methods. Longuet-Higgins & Turner (1974) developed a model for a spilling breaker. They considered an entraining plume model of the breaking zone, originating from the wave crest and riding down the front face of the wave. Later, Peregrine & Svendsen (1978) proposed a model for the flow field in steady and quasi-steady breaking flows. Longuet-Higgins and Turner's model may be applicable to the initial stages of the wave breaking, which is inherently unsteady, and that of Peregrine and Svendsen to the later stage, in which a quasi-steady flow has developed. Based on Peregrine and Svendsen's model, Battjes and Sakai (1981) investigated the turbulent wake induced by a breaking wave generated by a submerged hydrofoil. The dynamics of the steady breaking waves generated above a submerged hydrofoil were first explored experimentally by Duncan (1981, 1983), who made systematic measurements of the breaker shape and the mean flow in the wake of the breaker. He determined the resistance associated with the breaker and found that this resistance was proportional to the component of the weight of the breaking region that was tangent to the front face of the wave. Cointe & Tulin (1994) presented a theory of steady breakers based on the experimental results of Duncan (1981, 1983). They modeled the breaking zone as a weak eddy remaining in place on the forward face of the wave by shear stresses from the underlying flow. It was assumed that these stresses balance the down slope component of the weight of the breaking region as was found experimentally by Duncan (1981 and 1983). Lin & Rockwell (1994) measured the flow

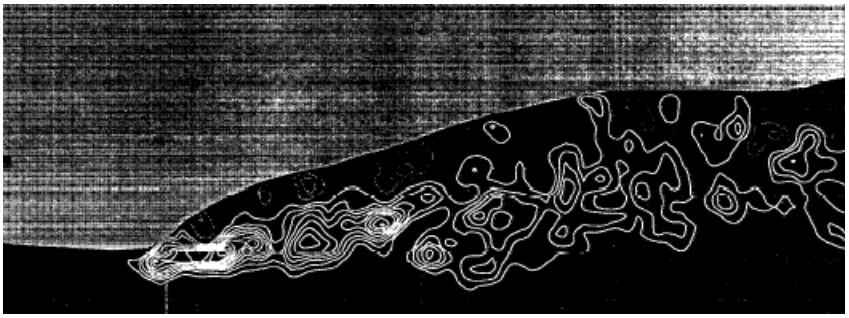

Figure 2.1: The vorticity field which is dominated by positive vorticity with high levels in the mixing layer and low levels of negative vorticity in the region close to the free surface. From Lin & Rockwell (1994).

structure of a stationary spilling breaker that was generated by a submerged hydrofoil. They used high-image-density particle image velocimetry to provide the shape of the free surface and the velocity field beneath it. The vorticity field from Lin and Rockwell's work, shown in Figure 2.1, is dominated by positive vorticity with high levels occurring in the mixing layer between the nearly stationary breaking region at the surface and the upslope laminar flow underneath it. Low levels of negative vorticity are detectable only in the region adjacent to the free surface. Coherent concentrations of vorticity are evident in the upstream region of the mixing layer.

Later, Lin & Rockwell (1995) studied all stages of the evolution of a quasi steady breaker from the onset of a capillary pattern to a fully developed breaking wave, using the same technique. A flow field in the toe region for a breaking wave length of 0.15 m is shown in Figure 2.2. Note that the leading edge of the breaking region is located near the minimum surface height in the trough, indicating that this is a strong breaker for the given flow speed (Duncan 1981).

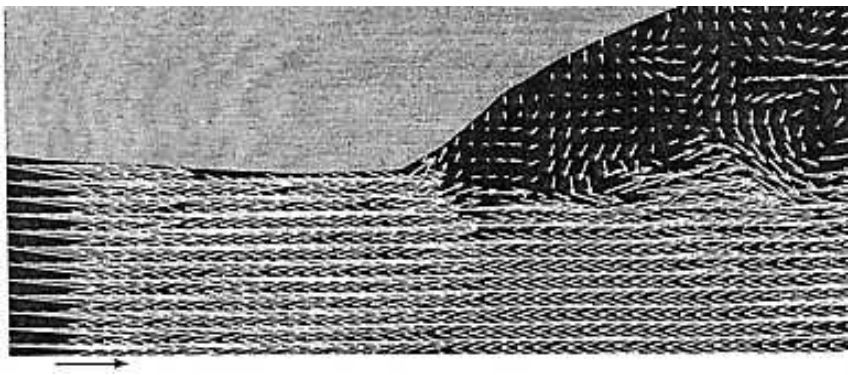

Figure 2.2: A flow field of the toe region for wavelength of 0.15 m by Lin & Rockwell (1995).

2.2 Breaking Bow Wave Research

The two primary components of ship resistance are friction and wave making, which can be thought of as shear and normal forces, respectively. Friction results from the development of a viscous boundary layer around the hull and can be modeled to first order as flow over a flat plate with area equal to that of the ship's wetted surface. Wave making resistance results primarily from the dynamics pressure the water exerts on the hull as the ship as the ship moves through the water. These waves transport energy away from the ship. William Froude was the first to appreciate the separate components of ship resistance and advocated the use of towing tanks to determine the resistance of ships. Froude's innovations roughly coincided with the fundamental studies of linear and nonlinear water waves by Stokes (1847), only a decade earlier. In 1887, Lord Kelvin (William Thomson) derived the pattern of waves created by a moving infinitesimal disturbance, known as the Kelvin wave pattern, shown in Figure 2.3. The Kelvin wave pattern is comprised of divergent

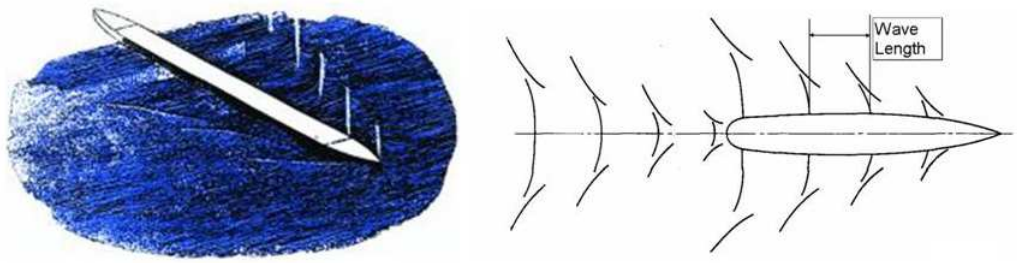

Figure 2.3: Kelvin wave pattern (as drawn by William Froude)

(roughly perpendicular to direction of motion) and transverse (following the motion) waves. A decade later, Michell (1898) developed the first analytical expression for wave resistance using a technique commonly known as thin-ship theory. This technique models the ship as a straight line of pressure sources moving through a calm, inviscid fluid. Additional developments by Stokes, Osborne Reynolds and Lord Rayleigh in the 1870's completed the basic linear theory of ship waves that is still used today.

The wave pattern around the bow of a ship mainly depends on the shape of the ship, the draft and the Froude number. For blunt shapes, breaking occurs ahead of the bow, whereas for fine ships with a sharp stem, the free surface flow, after passing the stem,rises along the hull surface downstream of the stem, and then falls down. A comprehensive experimental study of the divergent bow waves were made by Inui (1970) and his colleagues in Tokyo; see also Inui et al. (1979) and Miyata (1980). Miyata claimed that these waves are non dispersive and nonlinear and called them free surface shock waves. Nonlinear wave formation depends on the configuration of the ship hull. Baba (1969) noticed the singular free surface phenomena around

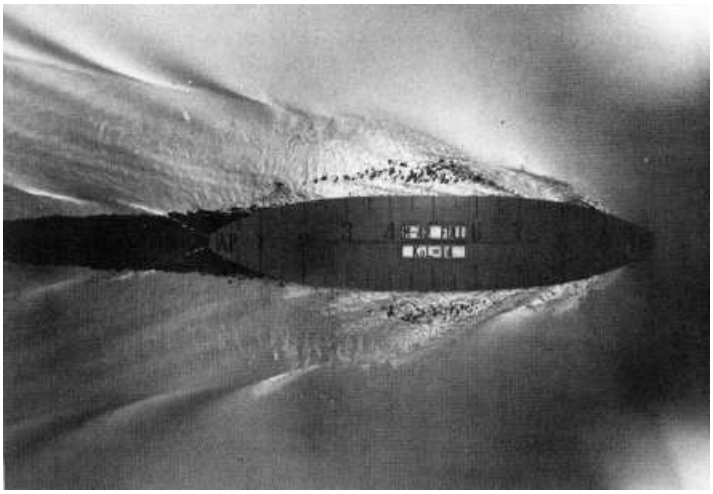

Figure 2.4: Wave patterns around a fine ship model with the draft of 0.105 advancing at Fn = 0.267. The water surface, covered with an aluminum powder film, is split near and behind the model.

the bow of the ship and interpreted that as the breakdown of waves. Miyata & Inui (1984) have reviewed and summarized most research done on the ship-generated waves by that time. They have done a comprehensive experimental and numerical research on the free surface flow structure and wave pattern around several ship models. They used aluminum powder for visualization purposes and consequently they were able to observe wave patterns around the models. A typical wave pattern of a fine ship model being towed in their tank is shown in Figure 2.4. In their experiments, they observed the bow waves of sharp-ended models and found that the strength of the breakers and the slope of the forward face of the bow waves increased with an increase in Froude number.

The flow field in three-dimensional breakers, observed around ship bows were not quantitatively studied in detail until the late 1990s, when Particle Image Ve-

locimetry (PIV) techniques came in to play. Perhaps the first detailed study of the structure of the flow field within the breaking waves generated by a ship model was made by Dong et al. (1997). In their experiments, PIV was employed to obtain velocity distributions in the near field of a ship model bow. The results show that the formation of a breaking bow wave involves considerable production of vorticity originating from the toe of the breaker; similar to what was already reported for two-dimensional spilling breakers (Banner & Peregrine 1993; Lin & Rockwell 1994, 1995; Dabiri & Gharib 1997). In the bow waves, most of the vorticity remains close to the forward face of the wave. Ship generated waves have a powerful counter-rotating vertical structure concentrated near the wave crest. Vorticity with opposite signs are much stronger than their two-dimensional counterpart. The vorticity generated at the wave crest is fed into the flow behind in a series of distinct filaments that create a series of elongated bumps on the free surface. In the larger Froude number case of the study, the bow wave plunges on the forward face of the wave and creates a bubbly wake. Roth et al. (1999) also conducted an experimental investigation of the flow field around a ship model. In their experiments, PIV was used to obtain velocity distributions in the near field of the models and measurements were repeated many times at several locations in order to obtain statistical information about the turbulent flow field of the breaker. They found that the average vorticity contours are in many respects qualitatively similar to the instantaneous vorticity contours for an unsteady two-dimensional spilling breaker that is dominated by surface tension (Figure 2.5).

A series of studies by Waniewski et al. (1997, 2001 and 2002) simulated

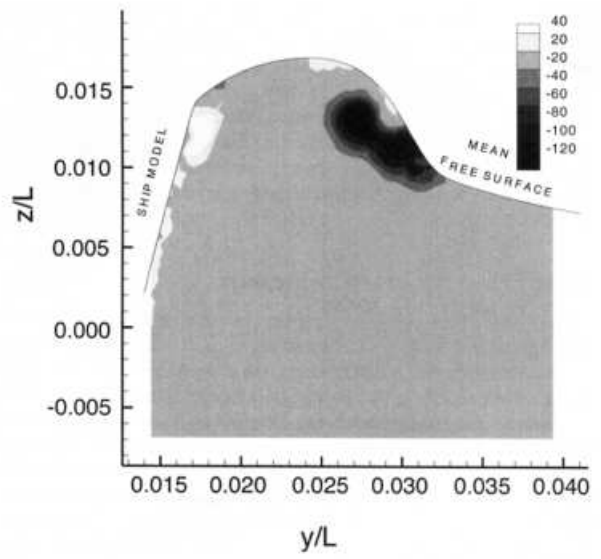

Figure 2.5: Contours of average vorticity in a tilted plane through the breaking bow wave of a ship model. Negative vorticity is directed into the page. Fr = $U/\sqrt{gL}$ = 0.3, where U = 2.51 m/s is the model speed and L = 7.01 m is the model length. From Roth et al. 1999.

a plunging bow wave by placing a deflecting plate in a supercritical free-surface flow. Surface profiles of the resulting waves were measured and used to investigate scaling and dependence on geometric parameters. In general, the profiles of for all conditions agreed near the leading edge of the plate but deviate significantly thereafter. Scaling was typically done as an empirical function of Froude number, Reynolds number and draft (Figure 2.6). Air entrainment in the wave was also investigated using impedance probes. Surface disturbances were observed on the plunging jet that are qualitatively similar to those described by Longuet-Higgins (1995).

Surface disturbances downstream of the breaking bow waves are addressed in great detail by Olivieri et al. (2007), who were primarily interested in the phenomena

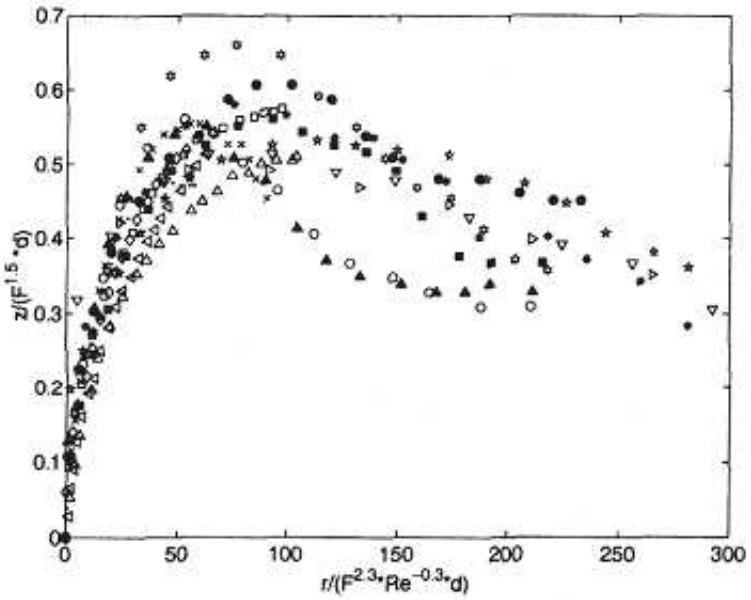

Figure 2.6: : Nondimensional bow wave profile data comparing towing tank data (open symbols) and flume data (closed symbols). From Waniewski et al. (2002).

of "scars" , sudden changes in surface elevation forming streamwise streaks within the wave pattern (Figure 2.7). Results showed that these streaks are the result of counter-rotating vortex pairs generated by the breaking bow waves. The downward flow between the vortices creates a depression in the surface, which appears as a scar. Near surface counter-rotating vortex pairs are known to be a source of instability and surface striations in other flows as well (Sarpkaya and Suthon, 1991).

2.3 2D+T Approximation

The 2D+T (Two Dimensions plus Time) approximation is a method for simplifying a three-dimensional system using a two-dimensional model. For ship waves,

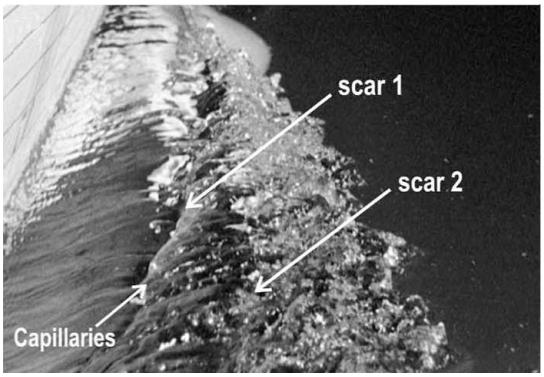

Figure 2.7: Presence of scars in the shoulder wave of a ship model (from Olivieri et al. 2007).

three-dimensional bow flow can be approximated by a two-dimensional, time evolving flow in which the hull is replaced by a deforming wall which at any time t ($t = 0$ is the moment of passage of the stem at the mean water level) takes on the shape of the cross section of one side of the hull at the streamwise (x) location corresponding to $x = Ut$ where U is the equivalent speed of the three-dimensional ship model. This method is applicable only to ships with fine bows moving at constant forward speed and only divergent wave components are produced. The flow is unaware of any longitudinal effects such as the stagnation point at the bow that would result in elevated water upstream of the hull. The impact of the stagnation point on upstream elevation is substantial for blunt-bow ships such as tankers; however, for narrow bows, the effect is relatively weak and thus not a major source of error. Previous studies by Tulin & Wu (1997) and Shakeri et al. (2009a) have accounted for this with a small longitudinal shift of the resulting wave pattern. Tulin & Wu (1997) used 2D+T technique for calculations of a Wigley hull. Figure 2.8 shows

a comparison of the wave pattern for a ship hull. The same individual divergent waves, bow and stern, can be seen in each calculation, and their origins and extent match well. It shows the prominent rooster tail behind the stern and the resulting diverging waves. There are differences between the two patterns. The 2D+T waves are less dispersive, and transverse waves are absent. A comparison has been made for a typical Wigley hull with the exactly fully nonlinear 3D calculation of Raven at MARIN, as shown in Figure 2.8. The general appearance of the multi-wave system is identical in each simulation (splash, three divergent bow waves, rooster tail, two divergent stern waves on each side of the hull). The origin of each feature and general extent are similar. However, the crests of the 2D+T waves are much sharper. For typical fine ship slenderness, the crest of the divergent bow waves tends to be straight and their inclination decreases with increasing Froude number.

The similarity between breaking bow waves and two-dimensional deep-water breaking waves when examined in a 2D+T context was explored experimentally by Duncan (1999). In this work, a traditional plunging-type wave maker was used to create a series of short wavelength spilling breakers generated from dispersively focused wave packets. These waves were carefully observed and measured and plotted in a 2D+T manner, i.e., in the plot each successive wave profile in time was plotted at a location shifted upward and to the left by fixed succesive distances. As can be seen in (Figure 2.9), the resulting surface shape show a strong resemblance to a breaking bow wave on the starboard side of the ship model.

The success of the Duncan (1999) study led to the construction of a 2D+T wave maker in the Hydrodynamics Laboratory at the University of Maryland. A

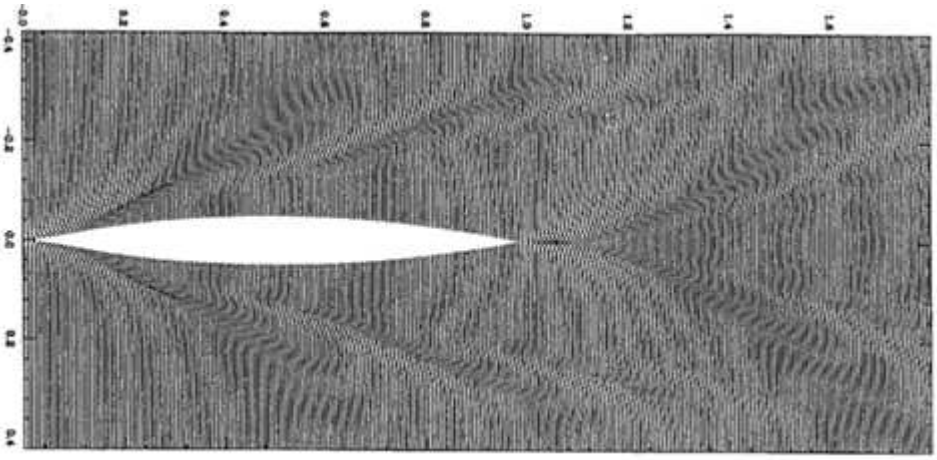

(a)

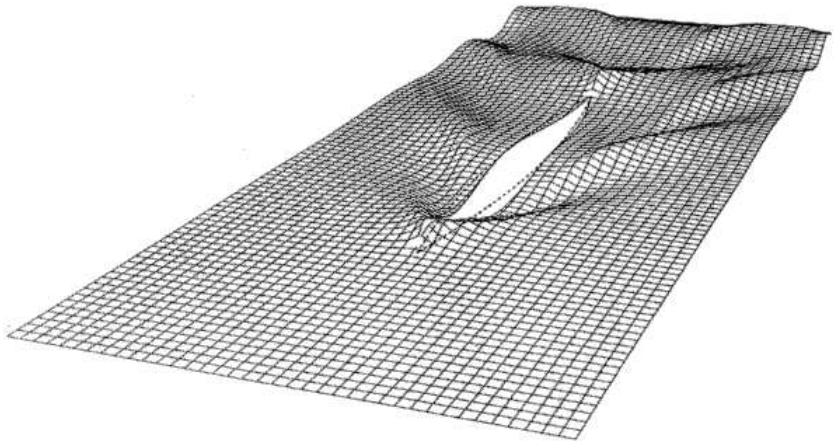

(b)

Figure 2.8: A comparison between (a) 2D+T: L/B = L/d = 10; FL = 0.30, and (b) exact nonlinear (RAPID) wave prediction. The RAPID calculation is by Dr. Hoyte Raven of MARIN.

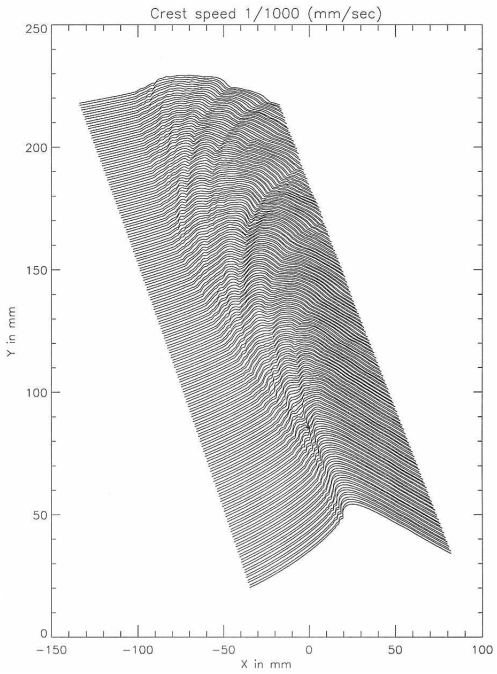

(a)

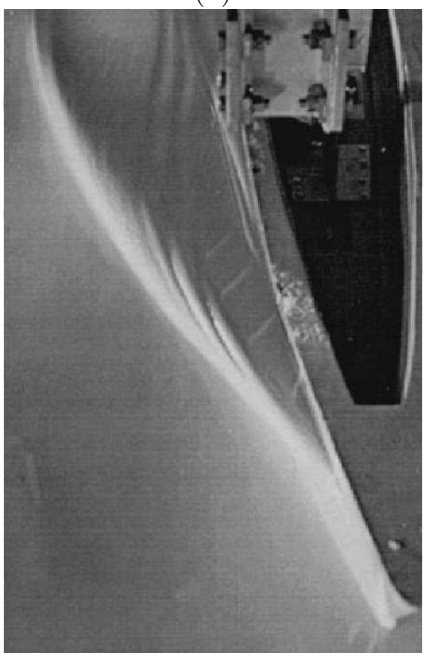

(b)

Figure 2.9: Comparison of 2-D wave profiles with a 3-D wave. (a) 3-D representation a spilling dispersively focused breaker using 2-D wave profiles (from Duncan et al. 1999) compiled according to 2D+T technique. (b) Overhead view of model test bow wave (from Dong 1997).

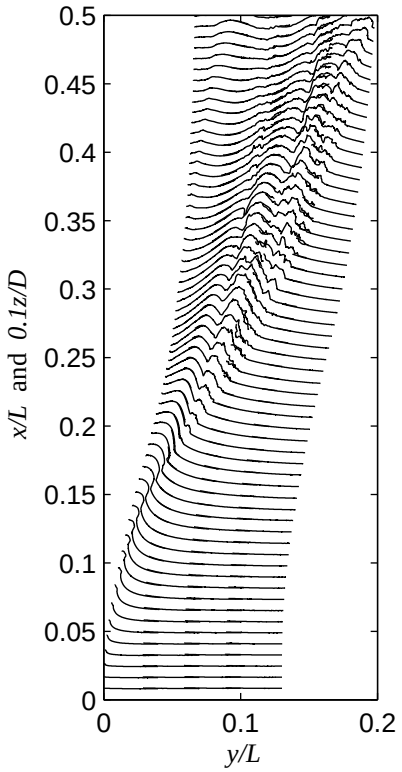

Figure 2.10: 3-D representation of a plunging bow wave created by a 2D+T wave maker (from Shakeri, 2009a). Profiles compiled by offsetting each 2-D surface profile by a fixed distance along the vertical axis.

detailed description of this device can be found in Section 3.1. Shakeri (2005) and Shakeri et al. (2009a) used the wave maker to simulate waves from a naval ship hull form (Model 5415 from NSWC Carderock). Using a similar plotting technique as Figure 2.9, profiles from a plunging breaker were plotted in a 3-D representation in Figure 2.10. In addition, comparison of the maximum height of the water contact line in the bow region with data from 3-D model tests and the theoretical considerations of Noblesse et al. (2006) are presented.

The contact point of the water surface on the surface of the wave maker were

tracked and the rise of the wave was found to increase with increasing ship speed. As the point of maximum water height moved away from the wave maker, thus becoming the crest of the wave, it moved at about 1.8 times that of the speed of the wave board (i.e. transverse speed of the hull surface) at high Froude numbers. The water jet produced by the plunging breaker entrained significant amounts of air as it crashed into the upstream water surface. Comparisons with three-dimensional model experiments were made in Shakeri et al. (2009b). The 2D+T wave maker was used to simulate bow waves produced by the R/V Athena (Model 5365 from NSWC Carderock). These waves were then compared with previous towing tank tests. The shape the contact lines for the 2D+T and three-dimensional model data sets were found to be quite similar (see Figure 2.11) for the highest Froude numbers, but the profiles tend to diverge downstream of the bow region point. As mentioned previously, a small longitudinal shift in the data was needed to account for the stagnation point of the three-dimensional model. The similarity of the wave profiles between the two sets of data improved with increasing Froude numbers as is to be expected with the 2D+T approximation.

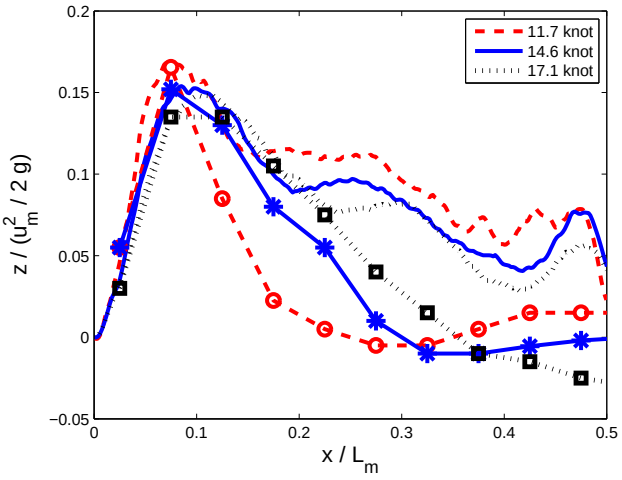

Figure 2.11: Contact line and wave profile measurements of R/V Athena hull using 2D+T wave maker (lines without data points) as compared with 3-D tank data (lines with data points). From Shakeri (2009b).

2.4 Air Entrainment and Bubble Production

The interest in bubble entrainment and behavior in breaking ship bow waves stems from ship detection issues. The bubbles entrained by the breakers enter the wake of the ship and this bubbly wake can last for very long distances downstream. Various acoustic sensors are able to detect bubbly flows, thus making the ship vulnerable to attack via its long bubbly wake. In examining the literature, it was found that there has been very little research on air entrainment in breaking bow waves. Thus, in the following we review primarily air entrainment in breaking waves in open water and on beaches.

The breaking process may or may not entrain air. In particular, in short wavelength breakers (say, wavelength less than 1 m) the crest region is dominated by

surface tension. When the wave length is short enough, the surface tension prevents overturning motions of the water surface and air entrainment is suppressed (Banner and Peregrine 1993). Lamarre and Melville (1991), among others, suggested that as the wave length increases, inertial effects dominate over surface tension effects and the breaking process produces air entrainment and for the wave heights of 50 mm or more; the effects of surface tension and viscosity on this process can be reasonably neglected (Couriel et al. 1998). At the sea surface, the entrained air generates whitecaps which are visible for wavelengths of about 1 m and longer, (Melville, 1996).

In deep water, the breakers are generally described as spilling and plunging breaking waves. In a spilling wave, the breaking process may be started by the appearance of a rough surface, or by the appearance of a small jet at the wave crest (Duncan, 2001). After this initial stage, a small region of turbulence forms at the crest of the wave and this region grows as water spills down the face of the wave (Duncan et al. 1994). In a plunging breaking wave, the first stage is the formation of a water jet at the wave crest. Thereafter, the falling water jet collides with the undisturbed water on the forward face of the wave and two processes occur simultaneously: the creation of a cavity of entrapped air beneath the water jet, and the water splash up (Bonmarin, 1989) upstream of the jet impact site. The air cavity entrapped by the jet is unstable and collapses, evolving into a bubble cloud. Simultaneously, the splash up created by the jet impact also entrains air resulting in a second cloud of bubbles.

Air entrainment can play an critical role in the dynamics of breaking waves.

The breaking process can dissipate up to about 40% of the initial wave energy and between 30% and 50% of the dissipated energy is used initially to force air below the water surface (Lamarre and Melville, 1991 and Hoque, 2002). In naturally occurring breaking waves on beaches and in the open ocean, air entrainment is an important phenomenon primarily due to its role in enhancing transfer processes between the atmosphere and the ocean. Bubbles can carry air down to depths on the order of the wave height and dramatically increase the interfacial area between the air an water, thereby increasing the mass transfer rate. There have been several studies comparing the bubble size distribution beneath breaking waves in freshwater and saltwater. Cartmill and Su (1993), Haines and Johnson (1995), Loewen, et al. (1996) and recently Blenkinsopp and Chaplin (2007) observed that the shape of the bubble size distributions for bubbles larger than $r \sim 1.0mm$ was the same in freshwater and saltwater; however, they found that a greater number of small bubbles (bubble smaller than $r \sim 1.0mm$) per unit volume occurred in saltwater than in freshwater.

Many previous authors have made estimates of void fraction in the bubbly flow beneath breaking waves in either the laboratory or the field (Loewen et al. 1996; Deane 1997; Vagle & Farmer 1998; Kalvoda et al. 2003). However, these measurements have generally been taken at a single often undefined location in the flow using instruments that average void fractions over regions and intervals that are not small in comparison with the wave's characteristic length and time scales. Several researchers including Hwung et al. (1992), Hoque (2002), Cox & Shin (2003) and Hoque & Aoki (2005) have carried out more detailed laboratory investigations of the void fraction field in breaking waves, providing useful information about

the vertical and horizontal distributions of void fraction. Lamarre (1993) used a conductivity probe to produce contour plots of the time-varying void fraction field beneath both two- and three-dimensional focused laboratory breakers as well as making some further measurements in deep water ocean waves. The results showed that the bubble plumes generated by breaking waves undergo rapid transformations and lose 95% of their initially entrained air volume during the first wave period.

The interpretation of the present measurements calls for an appreciation of scale effects. Deane & Stokes (1999, 2002) measured the size distribution beneath breaking waves in a laboratory flume (filled by seawater) and in the open ocean. They observed two primary mechanisms responsible for air entrainment in laboratory breaking waves; larger bubbles with a radius greater than 1 mm are formed by the fragmentation of the air vortex, while smaller bubbles are formed by the impact and subsequent splashing of the overturning jet. It seems probable that the volume of air trapped within the vortex and then entrained into the water column depends predominantly on the geometry of the overturning wave. They also found a change in the size distribution slope at $r \sim 1.0$ mm. They found that the bubble density (number of bubbles per m^3 per micrometer radius increment) was proportional to the bubble radius to the power of -3/2 for small bubbles (r less than 1.0mm) and to the power of -10/3 for large bubbles. Based on Deane and Stocks (1999, 2002), Blenkinsopp and Chaplin (2007) argued that the bubble size distribution of large bubbles will be similar at all scales because the same bubble creation mechanisms operate in the laboratory and in the field. Therefore, it is expected that laboratory studies of large transient bubbles conducted in freshwater will be applicable not only

to the open ocean but also to waves in fresh water under similar breaking conditions (Leifer et al. 2007).

Oguz et al. (1995) and Prosperetti & Oguz (1997) developed potential flow models of an impacting planar jet and falling water mass, respectively, and showed that, for strong impacts, the effects of surface tension and viscosity were negligible and the process of air entrainment was dominated by gravity and inertia effects. They suggested that the volume of air entrained by a single jet impact was dependent on the jet Froude number. Based on these studies it seems reasonable to assume that there should be no significant scale effects associated with the plunging jet entrainment mechanism and that the total volume of entrained air will scale geometrically. These findings suggest that the more important effects of scale are probably linked to the subsequent processes of bubble fragmentation, coalescence and rise. However, in air entrainment in breaking waves, scale (wavelength) has a dramatic effect on the geometrical and kinematic characteristics of the wave crest as it approaches breaking and the shape of the surface over the turbulent breaking region. Through these effects, scale will certainly affect even the initial amount of air entrained by the breaker.

Detailed knowledge of the distribution of entrained air and the behavior of the entrained bubble clouds would contribute to a better understanding of wave breaking in general as well as the influence of air entrainment on these processes. However, largely due to the practical difficulties of making measurements in a violent two-phase flow, the existing information is limited.

Chapter 3

Experimental Setup

3.1 Test Facilities

3.1.1 The Wave Tank

The experiments are carried out in a wave tank that is 14.80 m long, 1.15 m wide, and 2.20 m deep (water depth 1.83 m). A schematic of the wave tank is shown in Figure 3.1. The tank is supported by a row of steel columns on either side with 1.2 m spacing between columns. The side walls of the tank are made of 3.5-cm-thick clear acrylic plates to allow for flow visualization and optical measurements. The acrylic plates are supported by the steel columns and a set of horizontally oriented steel beams at several heights. The wave maker has an effective keel depth of 0.91 m, and the total water depth used all experiments reported herein was 1.83 m.

The 2D+T wave maker occupies about 2.8 m of the tank length at one end. This leaves about 12 m from the retracted position of the wave board (the mid plane of the equivalent ship) to the far end of the tank. The waves are expected to break and generate bubbles close to the wave maker. To allow sufficient time before reflected waves from the far end of the tank interfere with the flow and bubble measurements, the tank must be sufficiently long. As is shown below, in the present experiment the reflected wave will not arrive at the measurement site before a time

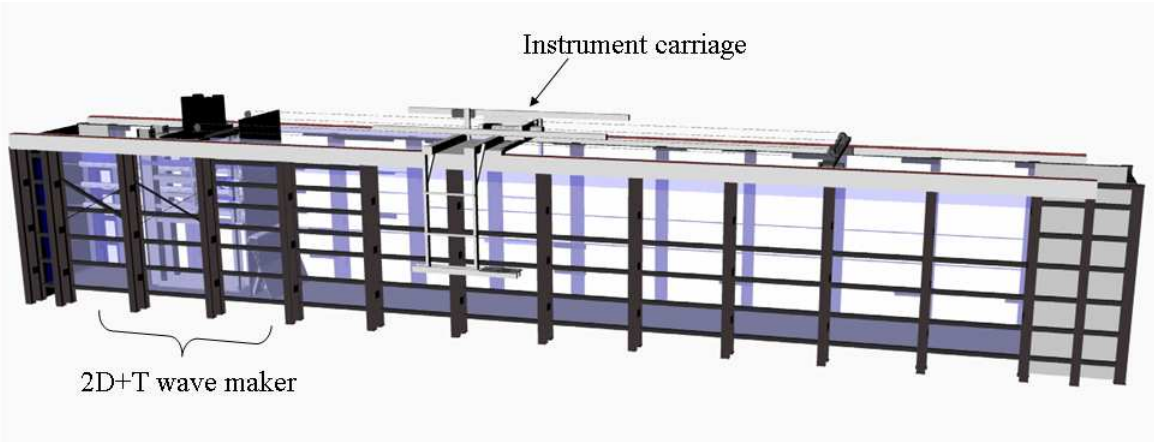

Figure 3.1: A schematic showing the tank and the wave maker.

equivalent to the passage of the stern in the full, three-dimensional model. The equivalent time of the passage of the stern of the ship model (ΔT_m) is given by

$$\Delta T_m = \frac{L_m}{U_m} = \frac{1}{F_r}\sqrt{\frac{L_m}{g}} \tag{3.1}$$

where g is gravity, L_m is the equivalent 3D ship model length, U_m is the equivalent 3D ship model forward speed, and $F_r = U_m/\sqrt{gL_m} = U_s/\sqrt{gL_s}$ is the Froude number and U_s and L_s are the equivalent full-scale ship speed and ship length, respectively. Using the above equation at $U_s = 27.5$ knots (the faster equivalent ship speed for the tests described herein, $F_r = 0.379$), we find $\Delta T_m = 1.931$ s. Also with $U_s = 22.5$ knots (the slower ship speed for the experiments described herein, $F_r = 0.310$) we find $\Delta T_m = 2.361$ s. Observations of the simulated bow waves have shown that the dominant wave component is about 2 m long. Using the linear dispersion relationship for deep water gravity waves, the group (energy) velocity of

these waves is

$$c = \frac{1}{2}\sqrt{\frac{g}{k}} = \frac{1}{2}\sqrt{\frac{g\lambda}{2\pi}} = 0.88\text{m/s}. \tag{3.2}$$

At this speed, a wave can traverse the 12-m-long distance from the wave maker to the end of the tank and the 12-m-long return in a time of $T_r = 27s$. This is about four times the model time scale, ΔT_m, even at the slower equivalent ship speed studied herein. Thus, these reflected waves are not expected to affect the measurements before the equivalent time of the passage of the stern. The highest possible surface wave speed in a tank of water of depth H is $\sqrt{gH}$ or 4.24 m/s for the present case with $H = 1.83$ m. This is both the energy and phase speed of a wave whose length is many times greater than the water depth. At this speed, a wave can traverse the 12-m-long distance from the wave maker to the end of the tank and the 12-m-long return in a time of $\Delta T_w = 5.66$ s which is longer thanΔT_m , even at the slower equivalent three-dimensional ship model speed. Thus, for the range of Froude numbers used for the experiments described herein, waves reflected from the far end of the tank are not expected to influence the measurements before the equivalent time of passage of the stern of the 3D ship model.

3.1.2 The 2D+T wave generation system

A schematic drawing of the wave maker is shown in Figure 3.2. The wave maker is powered by four servomotors which through gear reducers, drive four vertically oriented shafts. Each shaft drives a toothed pulley, which drives a piston through a rack and pinion system. The pistons, in turn, drive horizontally oriented drive

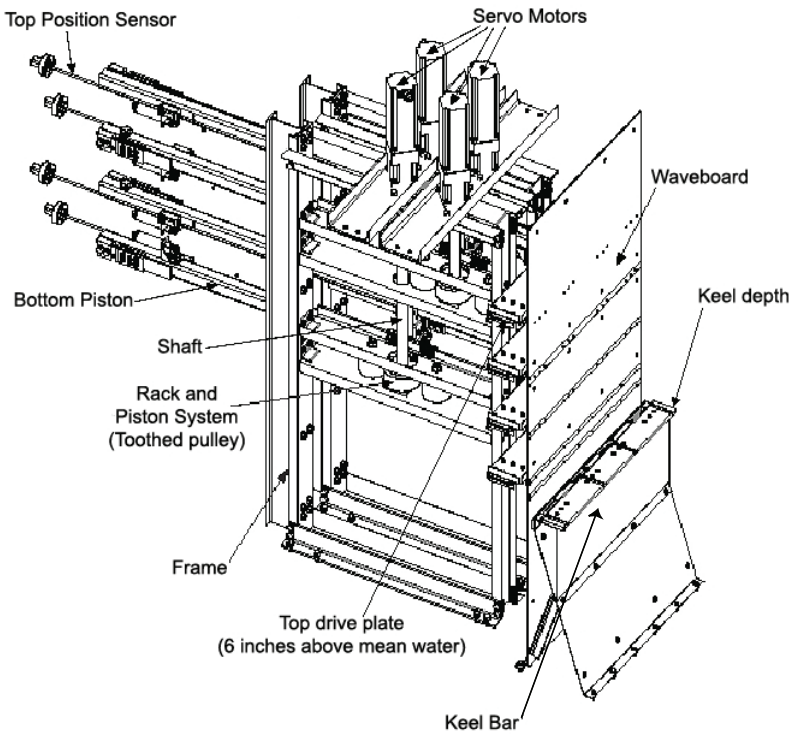

Figure 3.2: A schematic drawing of the wave maker designed and manufactured by MTS Systems Corporation.

plates that are as wide as the tank (1.14 m) and are guided along the tank walls by tracks. Position sensors and motor-shaft optical encoders are used in a computer-based feed back control system to achieve the desired motion of each piston. The feedback system adjusts the velocity of each drive piston in real time to achieve the desired wave board motion. The frame of the device is bolted to the bottom and sidewalls of the tank. Most of the device is submerged and is made of appropriate materials to resist corrosion. The main component of the 2D+T wave maker is the flexible wave board which is attached to the four drive plates via hinges. The wave board, which spans the width of the wave tank, is constructed from interleaved

1/16-inch-thick stainless steel plates of various lengths. The plates are slotted and riveted together in such a way that does not allow any flow of water through the wave board via a straight path. The stainless steel plates are thin enough to bend elastically under the differential action of the pistons. Each piston is attached to a different layer of stainless steel so that as the pistons move out at different speeds, the changing distance between the hinge points is accommodated by the stainless steel plates sliding relative to each other.

The keel depth of the 2D+T wave maker is created by bending the wave board over a fixed horizontal surface, called the keel bar, that spans the width of the tank. The keel bar depth serves as the effective draft, d_m, for the model. The keel bar is supported by a steel structure which is bolted to the floor of the tank. A Delrine block forms the top surface of the keel bar where it comes in contact with the wave board. This block is used to prevent the wave board from being scratched or otherwise damaged as it slides over the keel bar. For all tests in this study, the top surface of the keel bar is fixed at a depth of 0.91 m (36 inches) below the free surface.

In the tests, the 2D+T wave maker simulates the actual shape of half of a ship model (say the starboard side) from stem to mid-ship, aft of which the ship is assumed to be effectively parallel up to the stern. Even if this section is not parallel on the actual ship, it likely has negligible influence on the bow waves and can be safely ignored. As shown in Figure 3.3, the wave board is extended and bent at each time step, t, to mimic the corresponding half hull shape at a given longitudinal location, given by $x = Ut$. Figure 3.4 shows four photographs of the wave maker in

operation in the wave tank.

As mentioned above, the 2D+T wave maker is used to simulate the 5415 ship model built at the Naval Surface Warfare Center, Carderock. The 5415 hull profile was modified in two ways for use in the 2D+T simulations. First, the bulb that appears below the model keel depth was removed. This is necessary since the 2D+T approximation requires a slender bow while the bulb has a very blunt profile. Second, the stem region of the 5415 hull form was modified as is explained below. Figure 3.5(a) shows a plan view of the stem region at the mean water line. As can be seen in the figure, the stem of the 5415 hull shape has a small rounded nose. Simulation of this nose shape with the 2D+T wave maker would require the wave board to accelerate from zero to finite speed in one wave-maker control time step. When the wave maker attempts to create this motion it sets up an oscillation in the velocity of the drive channels and this in turn creates short wavelength surface waves. To remedy this problem the rounded stem was replaced with the sharp stem created from a third order polynomial as shown in Figure 3.5(a). Profiles of the wavemaker input to the four drive channels are given in Figure 3.5(b). Measurement of the time histories of the positions of the four drive channels for three runs at the highest equivalent ship speed indicates that the wavemaker reproduces these profiles with an rms error of at most 6 mm during the piston displacements which range from 1.44 m for the top drive channel to 0.87 m for the bottom drive channel. The corresponding run-to-run repeatability of the wave maker drive channel motion was within ± 0.8 mm rms at any instant during a run.

The 5415 ship model is a destroyer type hull. The beam to draft ratio of the

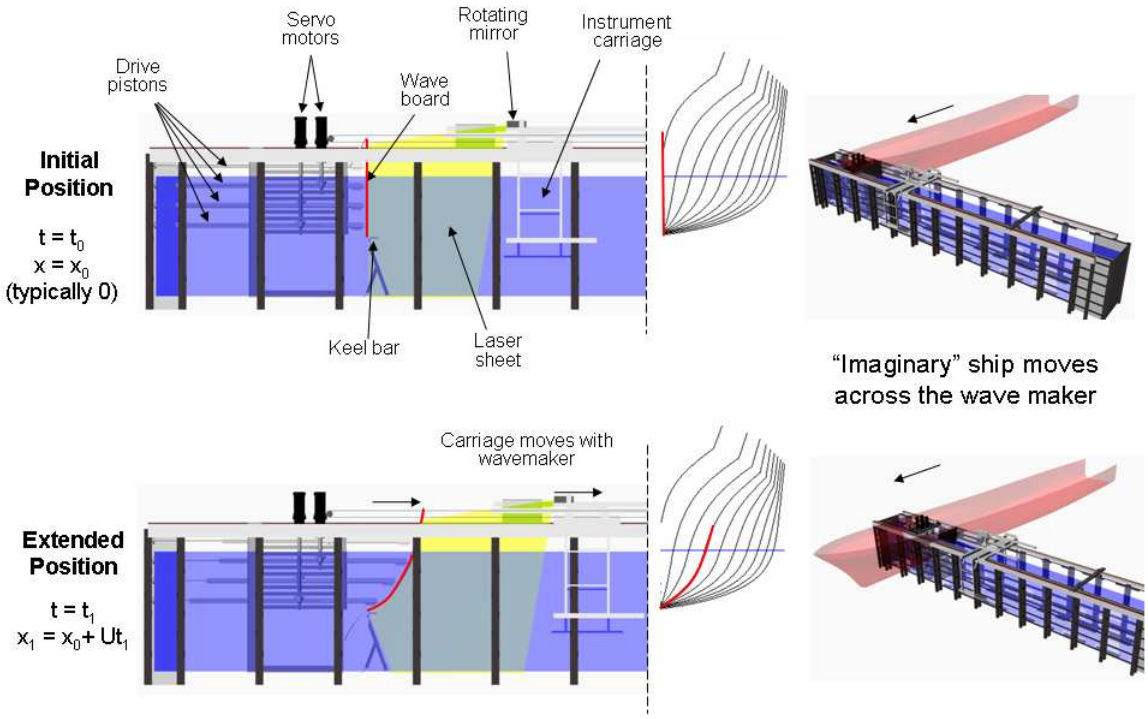

Figure 3.3: Overview of the 2D+T technique. The shape of the wave board at each time simulates the shape of the line of intersection of the port side of an imaginary ship model and the sidewall of the wave tank as the ship model moves forward at constant speed. In the top row of drawings, the wave board is fully retracted and the stem of the imaginary ship model is just touching the sidewall of the wave tank. In the bottom row of drawings, the wave board is in an extended position simulating the shape of the hull-tank wall line of intersection when the imaginary model has moved further into the tank. (From Maxeiner E. 2009).

5415 model is 3.11 and the length to draft ratio is 23.11. Thus, with a draft of 0.91 m, the half-beam of the 2D+T model and the equivalent 3D model is 1.41 m and the equivalent 3D model length is 21.03 m.

3.1.3 Instrument carriage

An instrument carriage rides on rails mounted on top of the tank. This system consists of the drive assembly, cables, tracks, instrument carriage, and position sensor. The carriage is controlled by the same computer and software that controls the wave maker. The carriage is powered by a servomotor which drives a horizontally oriented shaft. The motor and drive shaft are mounted on top of the tank about 8 m from the retracted position of the wave board. The drive system can supply force to the carriage in both forward and backward directions. The carriage is supported by four hydrostatic oil bearings that ride on precision rails, one on either side of the tank. When high-pressure oil is supplied to the bearings, a thin film of oil is forced between the bearings and the tracks. This oil layer dramatically reduces vibration and friction levels when the carriage is in motion.

In previous measurements of the bow wave profiles, the camera and light sheet optics for a laser-induced fluorescence measurement system were mounted on the carriage which was set to follow the motion of the top drive channel of the wave maker during each run. In the present measurements, the shadowgraph bubble-measurement system was mounted on the carriage which was held at a fixed location in the tank during each run.

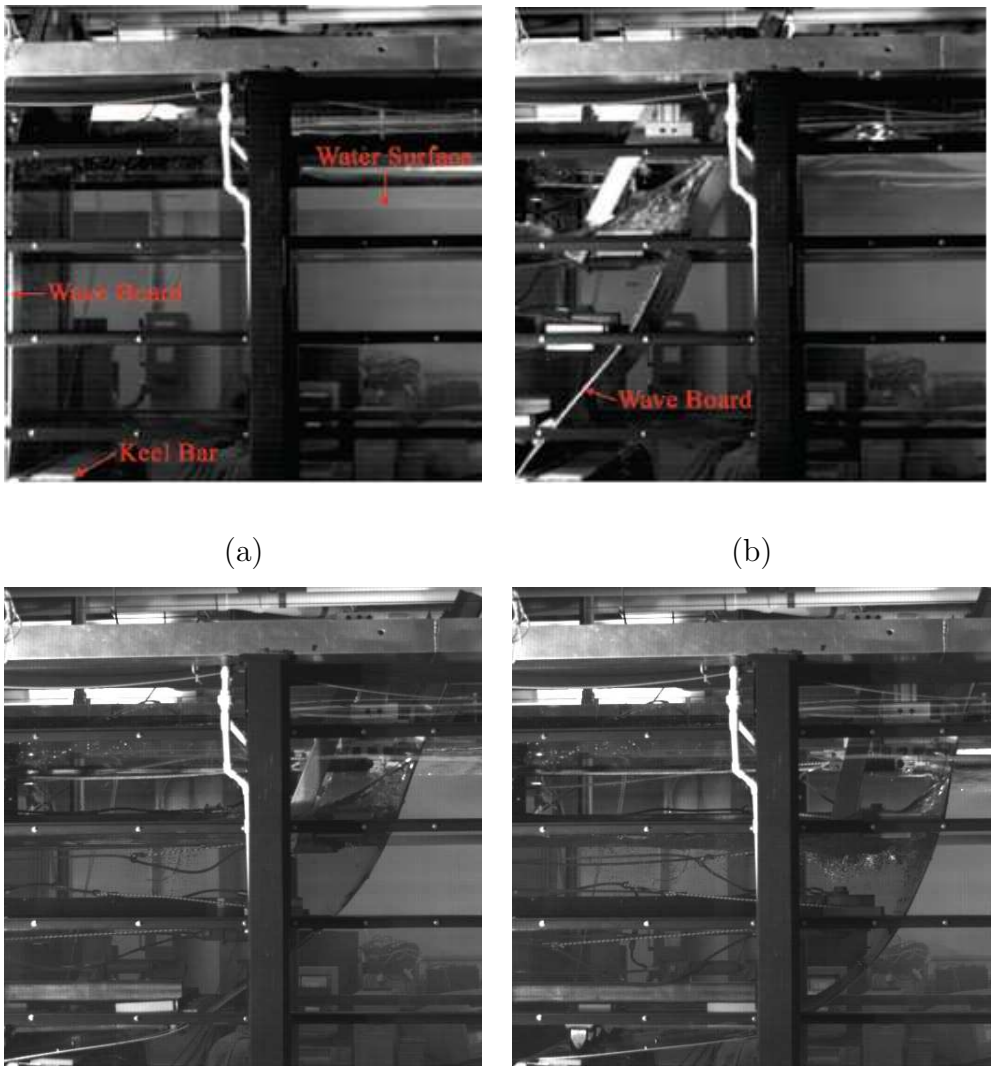

(a) (b)

(c) (d)

Figure 3.4: Photographs of the 2D+T wave maker in operation at four different times for equivalent ship speed of 16:5 knots. The time of each photograph relative to the start of the wave maker motion is (a) 0 , (b) 0.59 s, (c) 1.17 s, (d) 1.76 s.

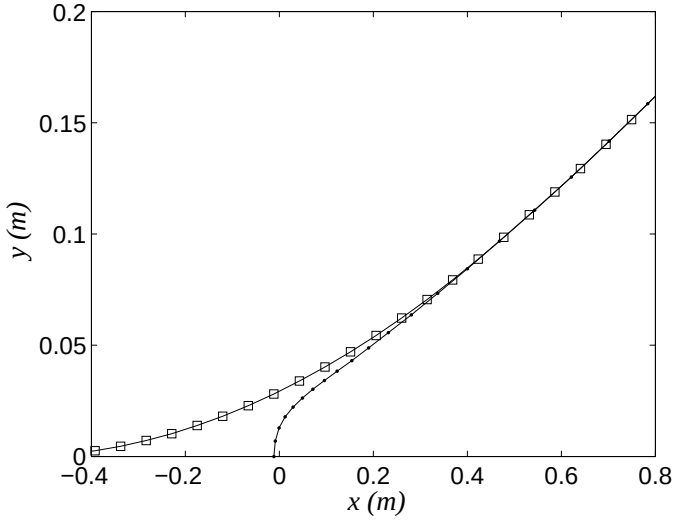

(a)

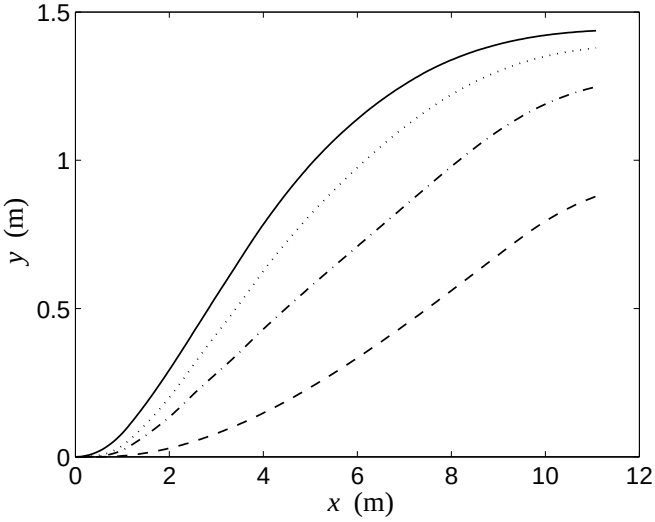

(b)

Figure 3.5: Profiles of the 5415 hull form in the horizontal (x-y) plane. (a) Profile of the starboard side of the stem region of the 5415 hull form at the water line and the approximation to it used in the 2D+T wave maker: • - waterline profile of the 5415 hull form, • - waterline profile of the equivalent hull form used by the 2D+T wave maker. (b) Profiles of the starboard side of the 5415 model from stem to midships at the elevations of the four drive channels of the 2D+T wave maker. The wave maker input signals are obtained by converting the horizontal axis to time via the transformation $t = x/U$. —— drive channel 1, $\cdots\cdots$ drive channel 2 , – · – · –drive channel 3 , — — — drive channel 4 .

3.1.4 Water treatment

In order to obtain bubble populations that are similar to those generated by breaking bow waves of ocean going ships, laboratory experiments must be performed in salt water and surfact levels in the tank must be controlled. The following describes the procedures used to prepare and treat the water in the present experiments.

At the beginning of each measurement series, the tank is filled with tap water through two cartridge filters and a diatomaceous earth filter. Hypochlorite is then added to the water (10 ppm) to neutralize organic materials. In order to create simulated sea water 1,500 Lb of Instant Ocean salt was mixed with the tank water. The resultant tank water had a density of 1.025 and a salt concentration of 35 parts per thousand. This artificial seawater is the same as that used in the Baltimore Aquarium.

In order to keep the water clean and relatively free of surfactants, a recirculation skimmer/filtration system was used. In this system, the surface water is removed through a surface skimmer. The skimmer has a cylindrical shape and is mounted horizontally on the side wall of the tank at the same height as the undisturbed water surface at the far end of the tank from the wave maker. Water enters the skimmer through a 2 cm high by 1.2 m long slot with a smooth lower edge (See Figure 3.6). The skimmer was positions so that the lower edge of the slot was about 2 mm below the mean free water surface in the tank. Water from the skimmer flows to a small tank and from there is pumped through a diatomaceous earth filter and

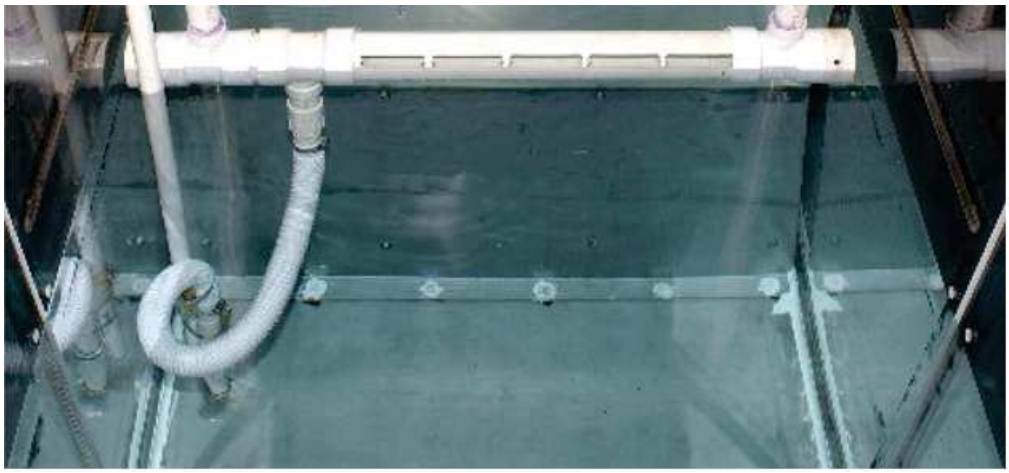

Figure 3.6: A picture of the skimmer system.

sent back into the wave tank at a point in the tank bottom near the wave maker. When fresh water was needed, tap water is sent through a separate filter before entering the wave tank. There is second diatomaceous filter whose suction and return lines are both below the water surface in the region behind the wave board. This filter is used to remove particulates that are generated by corrosion and operation of the wave maker. The filter/skimming systems are run nearly continuously during the experiments in order to maintain a low surfactant level. However, they are turned off about five minutes before each run of the wave maker on order to reduce residual tank water motions.

3.2 Experimental techniques

In order to make qualitative observations of the air entrainment process, movies were taken with the high-speed movie camera looking under the free sur-

face through the clear side walls of the wave tank. White back-light illumination was used for these movies. Figure 3.7 shows a sequence of two photographs extracted from a movie taken during the experiment with an equivalent ship speed of 25 knots. The camera is mounted on the instrument carriage and is looking up toward the free surface from below with a horizontal field of view of about 1.2 m. The instrument carriage is moving along the tank with the approximate speed of the breaking wave. The most important features seen in the air entrainment process are two clouds of bubbles under the free surface after the jet impacts the forward face of the wave and the splash forms. The cloud closest to the wave maker (the left cloud of bubbles Figure 3.7(a) is due to air entrapped by the plunging jet and the other cloud results from the impact of the splash. The cloud from the splash moves away from the wave maker at a higher speed than the cloud due to the plunging jet; therefore, the separation between the clouds increases as time goes on, see Figure 3.7(b).

Photographs of the bubble clouds were also taken with a stationary camera looking horizontaly with a field of view of about 2.2 m (wider than the field of view for the images discussed above). The camera was located 2 m from the inital position of the wave board as shown in the schematic in Figure 3.8. The corresponding photographs in Figure 3.9 show the bubble clouds for an equivalent ship speed of 27.5 knots at two times corresponding to equivalent positions of $0.375L_m$ and $0.50L_m$ downstream of the stem. Also shown are the theoretical shapes of the hull at these streamwise locations. The two clouds of bubbles, the left one from the entrapment under the crest at jet impact and the right one from the splash, can clearly be seen in the images. Comparison of the images shows the rapidly increasing separation of

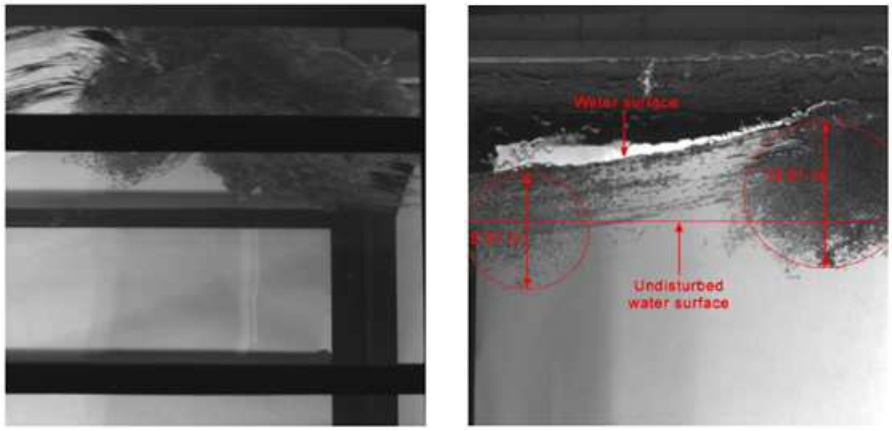

(a) (b)

Figure 3.7: Air entrainment process at two different times for equivalent ship speed of 25 knots.

the two clouds.

3.2.1 Available methods for measuring bubble sizes, bubble velocities and void fraction

In the current investigation, the generated wave, breaks by the formation of a plunging jet and creates a turbulent two-phase flow. The flow field beneath the breaker can be measured by different techniques depending on the void fraction in different stages in breaking process. In the first stage, big irregular shaped bubbles entrap and the void fraction is high. In the second stage, big bubbles rise up due to buoyancy force and leave the water field and small bubbles of the order of a few tens of microns will be left in the flow. A variety of techniques have been developed by researchers during the past several decades for measuring bubble size and velocity

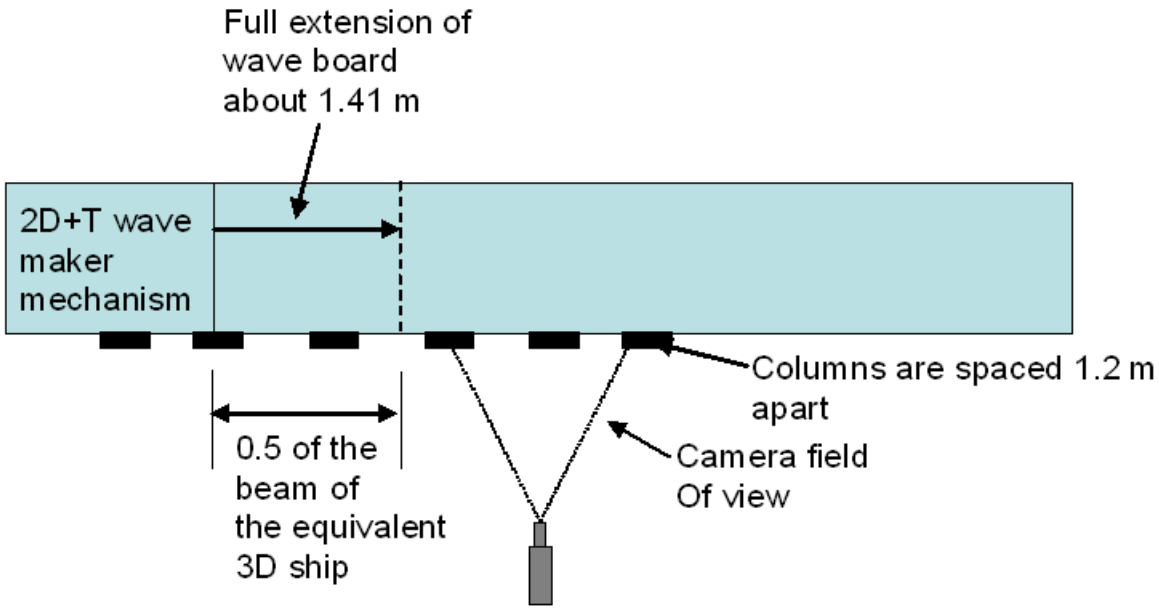

Figure 3.8: The schematic view of white light movie.

distributions within a flow.

In the early stage of the breaking process,void fractions and bubble distributions can be measured with an impedance measurement technique. This technique measures over a large poorly defined volume and has very poor spatial resolution; however, it is practically a technique capable of making measurements at high void fractions that are expected close to the breaking event. Theoretical analysis is used to determine the characteristics of the bubble population. Stokes & Deane (1999) developed an optical method for measuring bubble distributions at this stage. The system is consisted of a submerged camera, optical components, and a strobe light mounted within a transparent sealed case with a diameter of 11.4 cm. The case is then immersed in the interrogation flow field to perform bubble measurements.

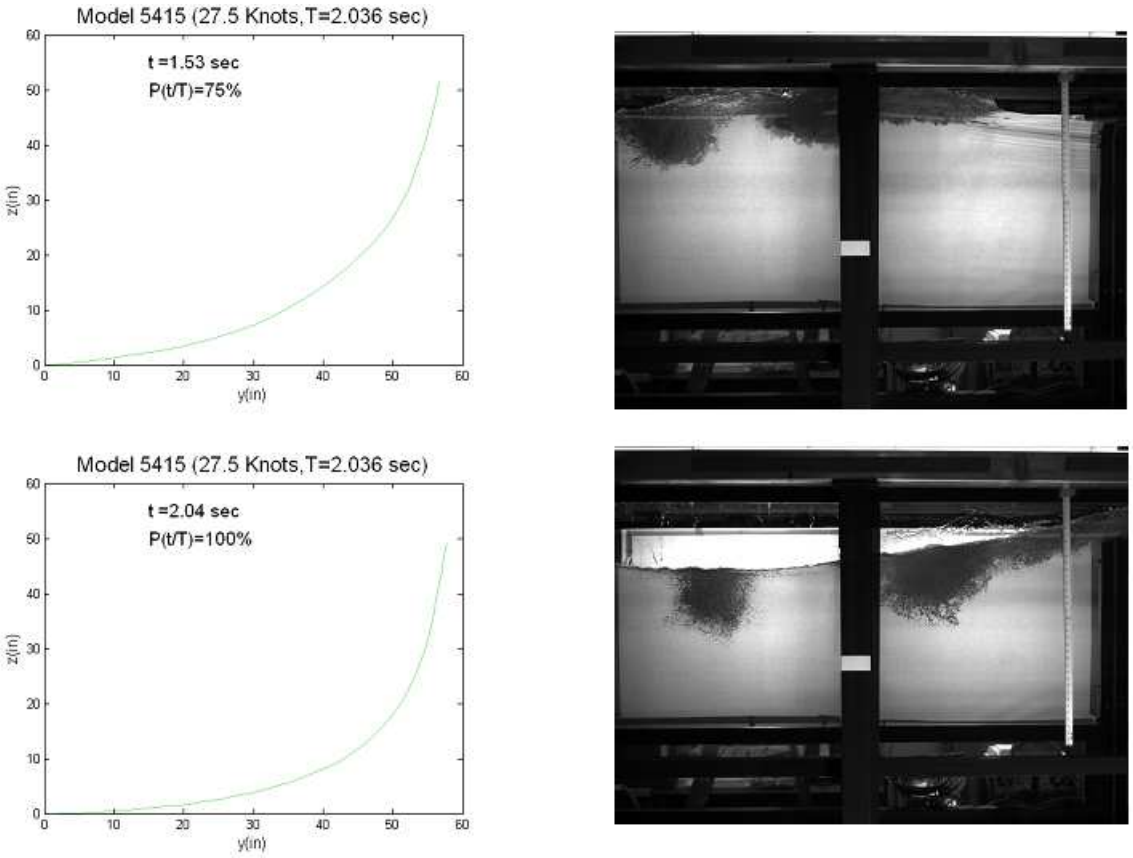

Figure 3.9: Air entrainment process at two times for an equivalent ship speed of 27.5 knots and the corresponding waveboard shape at each time. The photographs and profiles correspond to streamwise positions of $0.375L_m$ and $0.50L_m$ (midship) from the stem in the top and bottom rows, respectively.

The advantage of this system is that it does not have to look through a dense cloud of bubbles to take photographs of the area of interest. The disadvantage of this method is that it is strongly intrusive. In the second stage, acoustical methods are appropriate for void fractions from 10^{-8} to 10^{-3} and bubble sizes ranging from tens of micrometers to a few millimeters. For higher void fractions and bubble sizes, they seem to be impractical (Stokes & Deane 1999). In addition, they do not perform measurements very well in the region close to the free surface since acoustical waves are reflected by the interface at the free surface. As a result, useful information may not be extracted from the measurements in the vicinity of the free surface (Vagle & Farmer 1998). Acoustical methods only provide general information about the void fraction in space in the entire field. However, they have a good resolution in time. These techniques are unable to make any bubble size and velocity measurements. For this stage, where the void fraction is reasonable for photographic techniques, a shadowgraph technique is used to capture the flow field and bubble distributions. The shadpwgraph technique can provide information about void fraction as well as size distributions and velocity. In this work shadowgraph technique is chosen as explaned in the next section.

3.2.2 Shadowgraph measurement system

The shadowgraph system used to measure the bubbles is shown in Figure 3.10 and Figure 3.11. This system is similar to that developed by Jahne and Geiβler (1994). The light used for the imaging is created by a double-pulsed Nd:YAG PIV

laser. The laser head and the power supply remain on table on the floor beside the tank. The laser produces pairs of 9-ns-long pulses of green light (532 nm wavelength) with an energy of 160 mJ per pulse. The light is directed through two sets of half-wave plates and polarizing beam splitters to reduce and control the beam intensity. The light is then directed through two spherical lenses to focus the beam. At the focal point of these lenses, a pin hole with 200 micron diameter is used as a spatial filter and after that the light is passed through two achromatic doublet lenses which expand and collimate the beam. These two lenses are separated by a distance equal to the sum of their focal lengths. A periscope consisting of two mirrors facing eachother and tilted 45° from the horizontal in same direction sends the beam to the top of the tank and from there to the carriage. Two other mirrors, which are mounted on the carriage, are used to send the beam across the tank and vertically downward. The bubble measurements are made across a narrow section of the tank formed by placing a vertically oriented 1.8-m-by-1.2-m lexan plate in the tank 10 cm from one of the tank side walls, see Figure 3.11. The Lexan plate is attached to the instrument carriage and stainless steal bars are used as supports to keep the plate vertical. A sealed box 10 cm wide, 30 cm long and 45 cm deep is attached to the lexan plate on the side farthest from the near wall of the tank. A beam splitter and a mirror are mounted on a vertical traverse, which is in turn mounted to the instrument carriage, see Figure 3.11. The mirror and beam splitter can move up and down inside the box.

The beam encounters the splitter first and half of the light is reflected horizontally across the 10-cm gap between the lexan plate and the sidewall of the tank

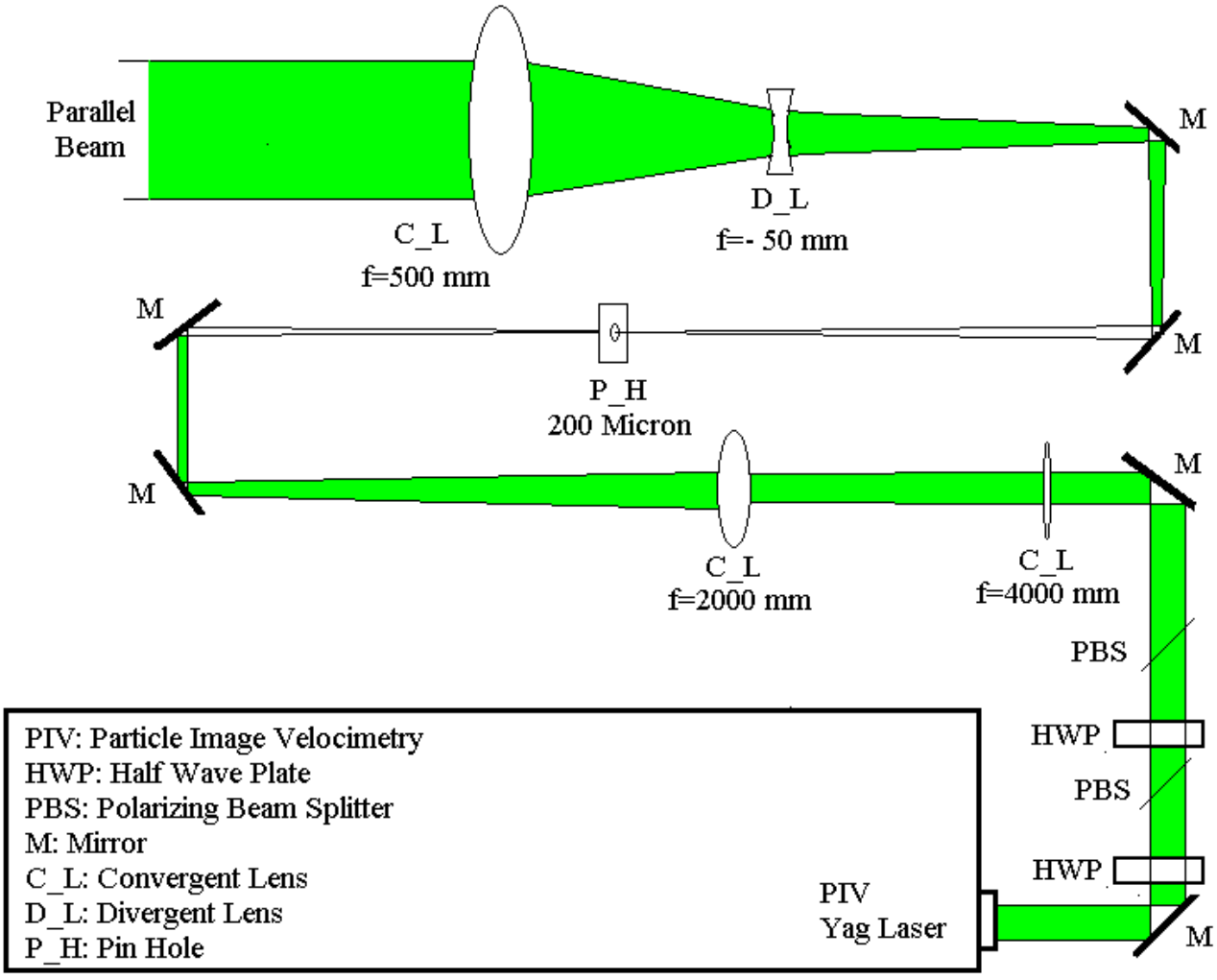

Figure 3.10: : A schematic showing the laser and optical devices used to create the exapnded parallel light beam.

while the remaining light continues downward to the mirror where it is also reflected toward the 10-cm gap. After passing through the gap horizontally, the light beams enter two Nikon 200 mm Microscope lenses with magnification of one to one at minimum focal distance connected to two PIV CCD cameras. The two light beams and cameras are used to reduce the number of experimental runs. The lenses are focused on the vertical center plane inside the 10-cm gap. The cameras (Kodak Megaplus ES 2020) have an image plane of 1600 horizontal pixels by 1200 vertical pixels and are shuttered to capture 14 image pairs per second. The two images in each pair are captured with a very small time delay. A timing signal is produced by the cameras at the beginning of each image pair. This signal is sent to a function generator which sends two pulses to the trigger input of the laser. The time delays for the two pulses from the function generator are adjusted so that one light pulse occurs in each image with a time delay between the two pulses of typically 2 ms. The result of the above system is a double-pulsed movie of shadowgraph images of the bubbles.

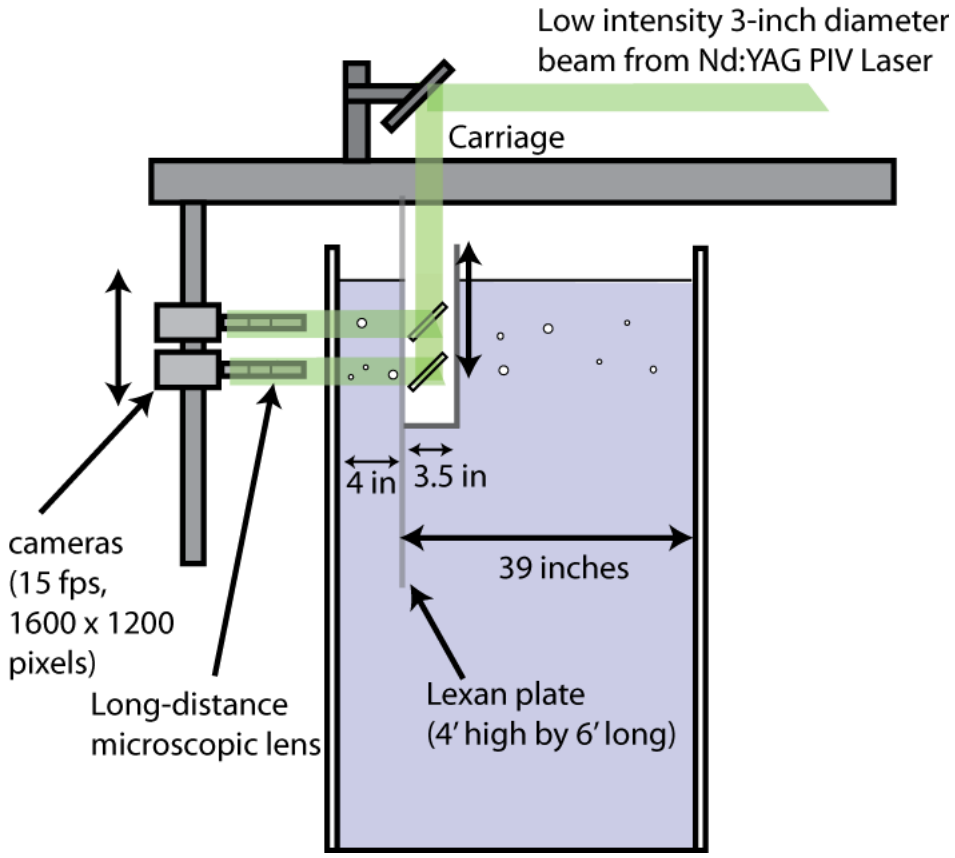

Figure 3.11: A schematic showing an end view of the tank (facing the wave board) along with the lexan plate, the cameras, the mirrors and the beam splitter.

Chapter 4

Measurement Techniques

Shadowgraph measurements of the bubble distributions created by the 2D+T wave maker were performend at two equivalent ship speeds, 22.5 knots and 27.5 knots. A white light photograph of the bubble distribution a the 22.5 knot speed is shown in Figure 4.1. At this speed, there is a weak plunging breaking and there is a relatively uniform bubble distribution in a narrow band near the surface. A corresponding photograph of the bubble distribution at the 27.5-knot speed is shown in Figure 4.2.

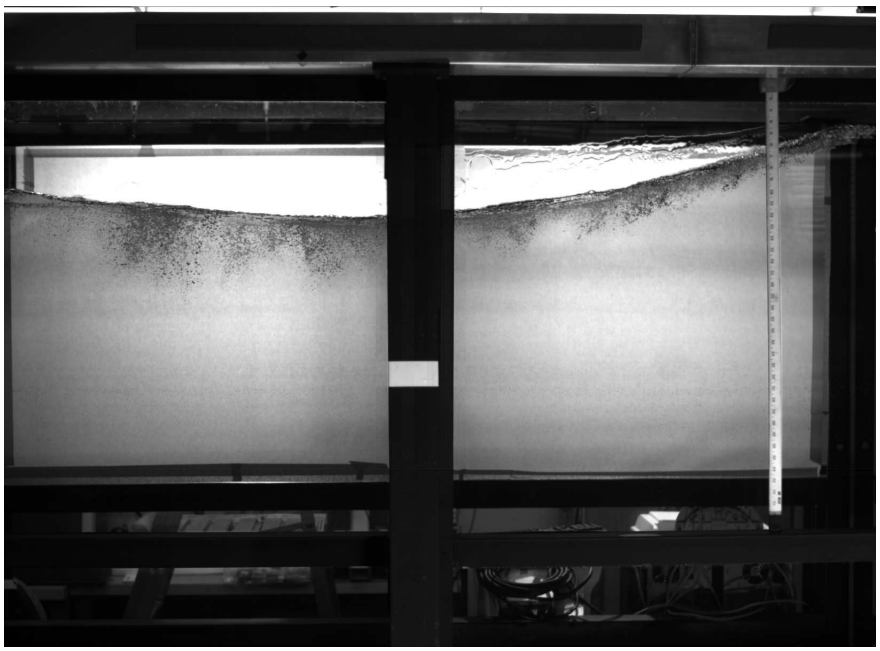

Figure 4.1: A sample white light image for 22.5 knots 2.5 seconds after starting the wavemaker.

At this speed, there are two clouds of bubbles, the first cloud (on the left) created by the air entrapped under the crest by the plunging jet and the second cloud (on

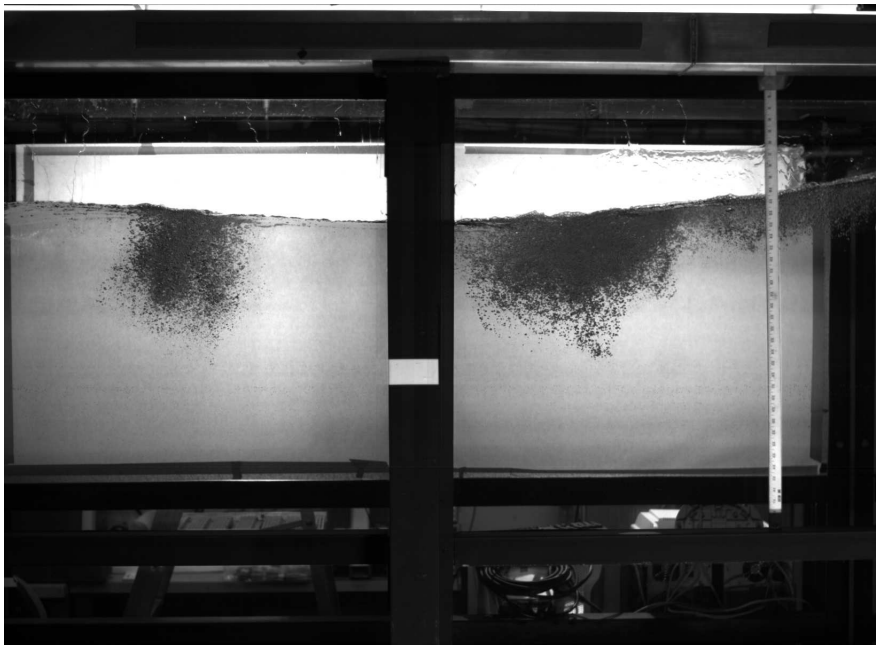

Figure 4.2: A sample white light image for 27.5 knots 2.5 seconds after starting the wavemaker.

the right) entrained by the splash created by the jet impact. This section gives a summary of the detials of the techniques and procedures used to measure these bubbles.

4.1 Instrument calibration

The objective of the optical setup described in the previous subsection is to obtain the diameters and velocities of the bubbles from each image pair. A two-step calibration procedure was required. In the first step of the calibration, a ruler was inserted into the focal plane and imaged to calibrate the viewing area in terms of pixels per millimeter. The viewing area, was fixed at 11.84 mm by 8.88 mm (135 pixels/mm) for all measurements. In the second step, targets of known physical

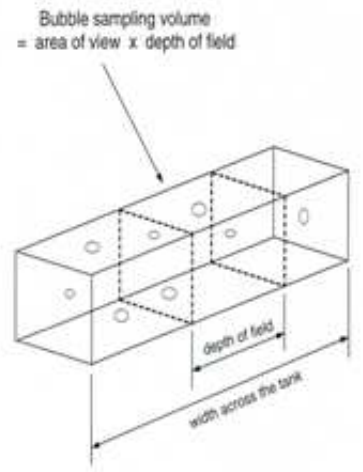

Figure 4.3: Bubble Sampling Volume.

sizes were imaged in and out of the focal plane of the camera lenses to determine how the distance from the focal plane affects the focus and the computed size of the targets in comparison with their actual sizes. This data is used with the field of view of the image to determine the measurement volume, which varies with target or bubble diameter, see discussion below and Figure 4.3.

The target is a Patterson globe reticle consisting of glass slide with 9 black circles of diameters from 21 μm to 450 μm etched onto its surface. The target is first attached to a motorized linear traverse system (Neat 310 Programmable Stepping MotorController) and placed in the span-wise center of the tank in the camera's field of view below the water surface. The camera is focused on the target, and this point becomes the focal plane. The target is then moved both toward and away from the camera in small finite steps out of the focal plane using the linear traverser. At each step, an image of the target is taken. As the target moves out of the focal plane, the

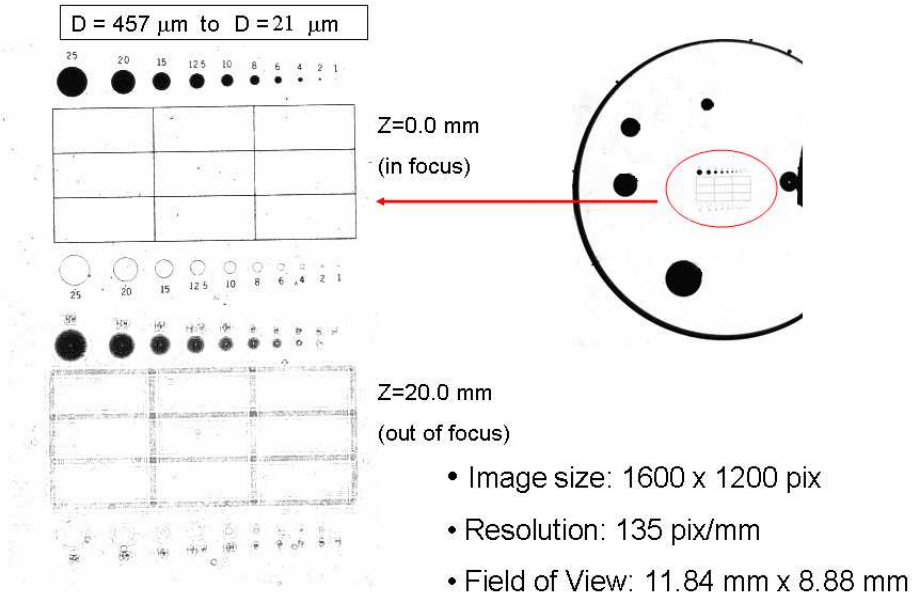

Figure 4.4: Two sample images of the calibration target. In the top image, the target is in the focal plane of the camera lens. In the bottom image, the target is 20 mm from the focal plane.

circles, which are sharp black dots in the focal plane, fade to grey intensities with fuzzy edges. Fresnel intensity patterns are also visible. The radius and intensity of the circles were determined using an axisymmetric two-dimensional function fit to the image intensity pattern. This function is of the form:

$$F = A_0(1 - tanh(A_1(\sqrt{(x - x_0)^2 + (y - y_0)^2} - A_2)) \tag{4.1}$$

Where the A_n parameters and the position parameters x_0 and y_0 are modified through a nonlinear least-squares method to obtain a best fit to the image data. These A_n parameters are: A_0 intensity, A_1 Sharpness , $A_2 = d/2$ radius, where d is the diameter. Sample images of the calibration target in and out of the focal plane of the camera lens are shown in Figure 4.4.

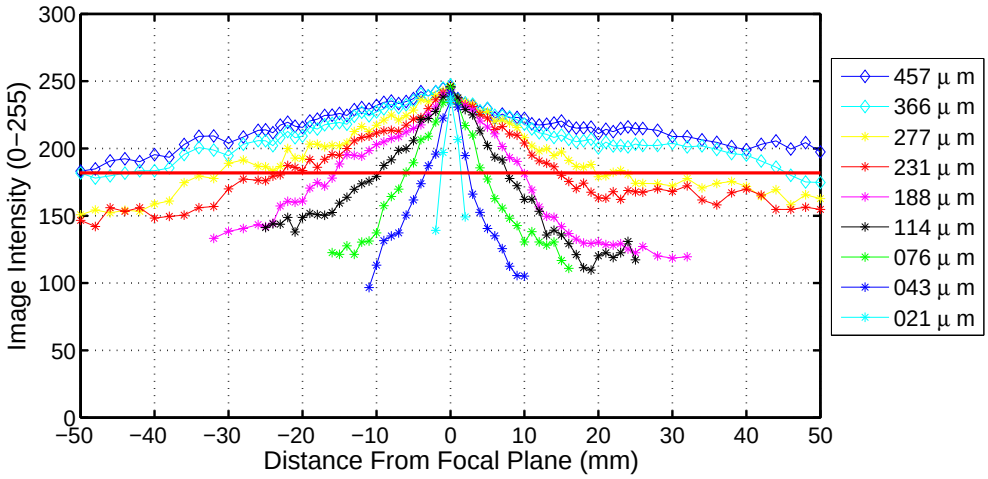

Figure 4.5: Intensity of the images of the various dots on a Patterson globe reticle as a function of distance of the recticle from the focal plane of the lens.

Figure 4.5 shows a plot of the average intensity of each dot (given as 255 - $\bar{I}$, where $\bar{I}$ is the average intensity of any dot, which ranges from 0 to 255) on the calibration target versus distance (x) from the focal plane ($x = 0$) of the camera lens. As can be seen in the figure, the intensities of all dots decrease as the reticle is moved out of the focal plane in either direction. This effect occurs more rapidly for the smaller dots than the larger ones. Figure 4.6 shows the effect of the target distance from the focal plane on the computed normalized diameters d/d_0, where d is the diameter of the image of a dot with the target at any distance (x) from the focal plane ($x = 0$) and d_0 is the similar diameter with the target at the focal plane. As can be seen from the figure, d/d_0 increases with increasing distance from the focal plane and this effect more rapidley for the smaller dots.

Careful analysis of the data in Figures 4.5 and 4.6 shows that limiting the

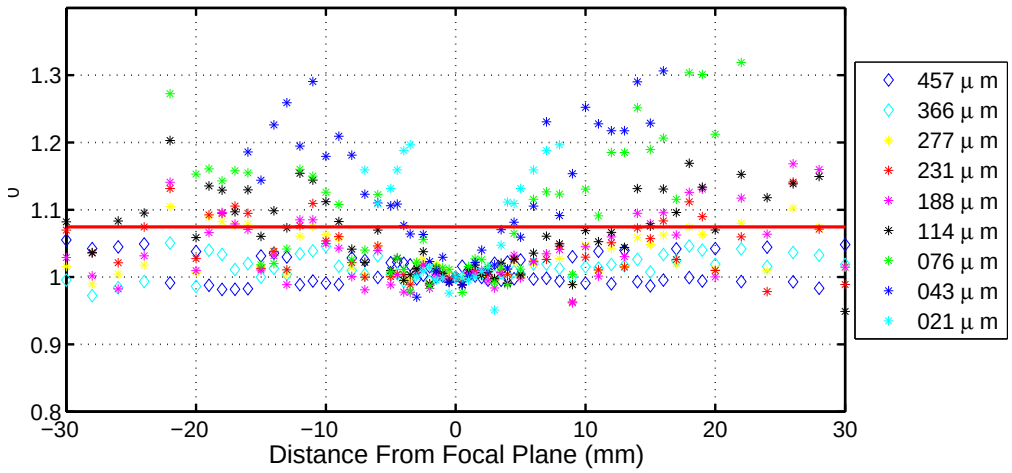

Figure 4.6: Normalized diameter of the images of the dots on the Patterson globe reticle as a function of the distance of the reticle from the focal plane. For all the data points below the red line, the image intensity was greater than or equal to 180.

dot (or bubble) images analyzed to those with intensities greater than or equal to the same value for all dot diameters results a maximum error in the estimation of the dot diameter from the images. This maxium error increases with decreasing intensity threshold. In the present work, the limiting intensity value was chosen as 180 (see the horizontal line in Figure 4.6), which resulted in a maximum error in estimation of dot diameter of 8% .

As can be seen in Figure 4.6, the range of x values for which the dot intensity values are above the threshold increases with increasing dot diameter. This range of x values is called depth of field (DOF). A plot the depth of field versus dot (bubble) diameter corresponding to the intensity threshold of 180 is shown in Figure 4.7. As can be seen, the maximum error in measure the depth of field is 6.3%. Using this

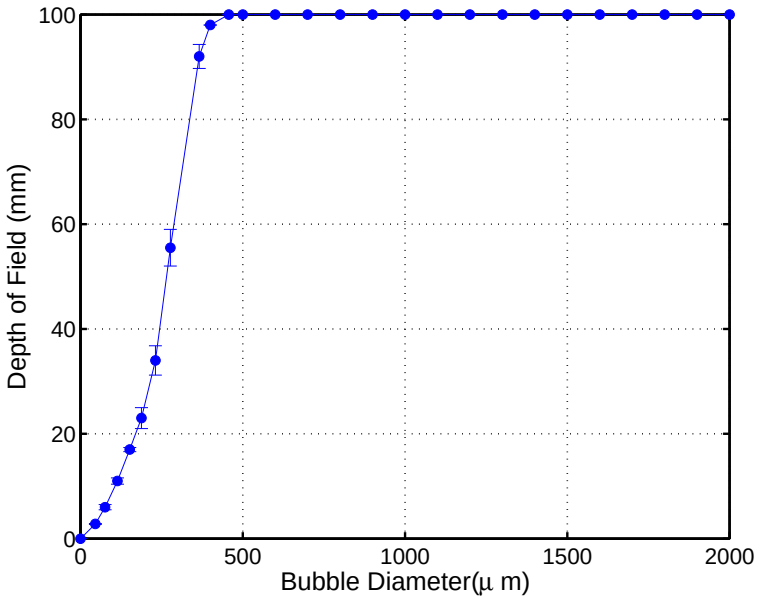

Figure 4.7: Depth of field (DOF) versus dot or bubble diameter (d).The vertical error bars indicate the error in the depth of field.

curve, the fluid sample volume (VOF) for each bubble size is given by:

$$VOF = A_v \times DOF \tag{4.2}$$

where A_v is the area of the field of view of the camera.

4.2 Sample air bubble measurements

To determine the characteristics of the entrained air in the wake of breaking wave, the tank and optics were configured as shown in Section 3.2. A sample image of a shadowgraph of bubbles from a breaking wave is shown in Figure 4.8 where the bubbles are the black dots. Note the similarity of the in-focus and out-of-focus bubble images to the in-focus and out-of-focus images of the dots on Patterson

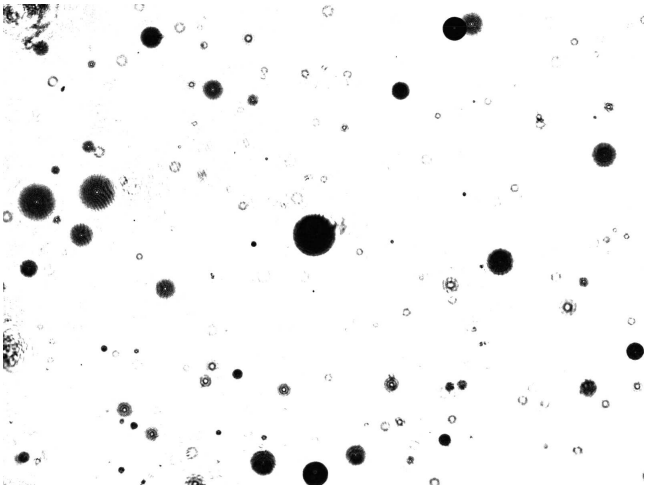

Figure 4.8: A sample shadowgraph image for 27.5 knot, t=3.15 sec at 336 cm away from the wave board and 8cm below.

reticle shown in Figure 4.4. Images like the one in Figure 4.8 were processed using a Matlab program to determine the radius and intensity level of each bubble image using the two-dimensional function fit described in Section 4.1. Through visual examination of the bubble images, the majority of the bubble images were circular, indicating that the bubbles themselves were very likely to be spherical. Shown in Figure 4.9 is an image of a bubble close to the focal plane. Also shown is a plot of the intensity (255 is completely black and zero is white) and a plot of the resulting nonlinear surface fit of Equation 4.1 to the bubble. As can be seen from the figure, the sides of the intensity plot are very steep and the top is a flat plateau-like form. The corresponding plot of Equation 4.1 is very similar to the image data. This is indicative of a sharply focused bubble which is confirmed by the high intensity value of the plateau.

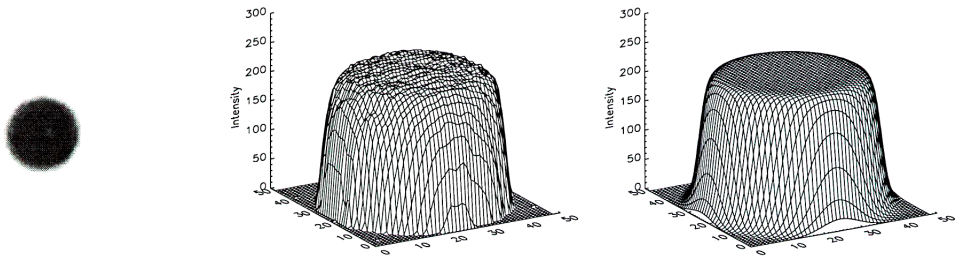

Figure 4.9: Intensity graph of a sample bubble close to the focal plane before and after fit a function.

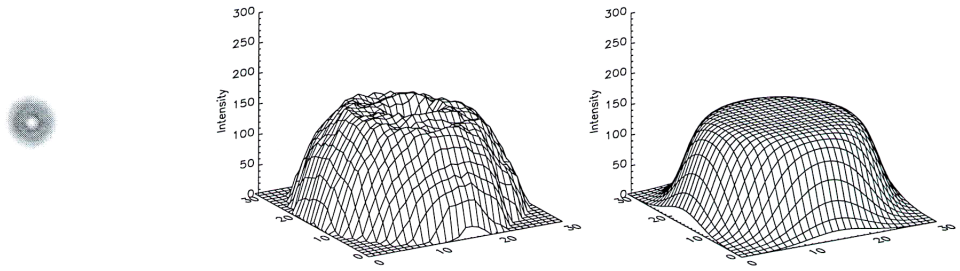

Figure 4.10: Intensity graph of a sample bubble away from focal plane before and after fit a function.

Shown in Figure 4.10 is an identical set of figures except that the imaged bubble is out of the focal plane. Here the sides of the intensity pattern are gently sloped and the top has a lower intensity value than the in-focus bubble and contains a divot in the center. This formation is indicative of a bubble that is out of the focal plane. Because the bubble position, radius and intensity are computed based on the nonlinear fit of Equation 4.1 to the intensity plot, the importance of the fit is easily seen. Figure 4.9 and Figure 4.10 illustrate the ability of Equation 4.1 to apply to

bubbles at all focal depths. Using Equation 4.1 and the depth of focus calibration data of Figure 4.7, the statistics for the bubbles imaged within the correct depth of focus were determined.

4.3 Velocity Measurements

Bubble velocities are determined in two step procedure. In the first step, a bubble in first image of one image pair is selected and the location of this bubble in the second image is determined to pixel accuracy as its approximate position. This is accomplished by correlation between images to find the nearest bubble with the same size and same intensity. This method utilizes a square interrogation window that has a length of 1.2 times the bubble diameter around each bubble. The idea behind this method is to make a copy of the interrogation window, and displace this copy to each x and y location corresponding to the expected displacement of the bubbles, which is 5 times of the bubble diameter in both the x and y directions in the second image. For each set of displacements, the first interrogation window is correlated with the new position of the interrogation window in the second image. The results of this are summed, and the largest total is the best estimate of the average displacement of the interrogation window.

The second step is accomplished by determining the position of each bubble image to sub-pixel accuracy by fitting Equation 4.1 to the intensity data obtained from the first step are used as the approximate position of each bubble. The bubble velocity is computed from the displacement between bubble positions in two images

and the known time delay.

The accuracy of this method was determined by using a sample image which is include several bubbles with different sizes (30 μ m to 1 mm) and giving it the known displacement of 20 pixels at each directions (x and y) to create the second image . Two above steps were applied to compute the new position of the bubbles.The accuracy of this method is based on the size of the bubble. For large bubbles, this method is more accurate compared to the small ones. For the smallest bubble accuracy is 0.1 pixel ,so for 20 pixels displacement the error is 0.5 %. Since at this time, the approximate position of each bubble is known this part of work is much faster than the initial one.

4.4 Experimental Test Matrix

Since the field of view for the bubble measurement is small (8.88mm X 11.9mm), we need to take bubble measurements at many locations vertically and along the tank to cover the whole bubbly area. In this experiment, there will be two equivalent ship speeds studied, 22.5 knots and 27.5 knots. The side view of the tank is shown in Figure 4.11 for both speeds, with the resulting bubble clouds visible. Also shown on the images are the measurement grids for the bubble measurements (shadowgraph movies were taken at line intersections). For the first cloud of bubbles downstream of the waveboard at 27.5 knots, there needs to be 9 measurement points in both the y- and z-directions. However, for the second cloud of bubbles downstream of the waveboard, there needs to be 14 sections in the y-direction and 9 sections in the

z-direction. For 22.5 knots, since the distribution of bubbles are roughly uniform and shallow there needs to be the same points of measurement in y-direction but 5 sections in z-direction.

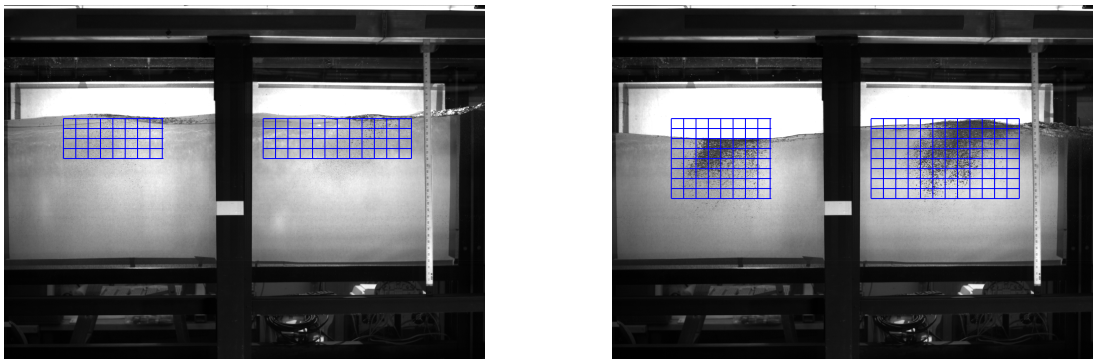

(a) (b)

Figure 4.11: Measurement regions for (a) 22.5knots and (b) 27.5 knots..

Chapter 5

Results and Discussions

The air bubble data was taken and processed to determine the detailed distributions and behavior of the air bubbles entrained by breaking bow waves. In the following, the 2D+T bow wave generation process as shown by previous surface profile measurements is presented first. This is followed by a description of the results of tests of the repeatability of the waves and bubble distributions. Finally, the main experimental results of the present work, including bubble distributions, void fractions, mean bubble diameters and bubble velocity fields are presented.

5.1 The 2D+T bow wave generation process

Casual observation of the bubbly flow created by the bow waves simulated by the 2D+T wave maker indicate that the number of bubbles and depth of penetration of the bubble clouds increase with the equivalent ship speed corresponding to the wave maker motion. In these first measurements of the bubbles produced by 2D+T bow waves, cases with plunging breakers and substantial air entrainment were chosen. The first condition corresponds to an equivalent ship speed of 22.5 knots where a weak plunging breaker is found. This breaker has a small plunging jet; if the equivalent ship speed of the wave maker is reduced to below 20 knots, a strong spilling breaker is found. The second condition is for an equivalent ship

speed of 27.5 knots, the highest ship speed available with the 2D+T wave maker. At this speed, a very strong plunging breaker with a large plunging jet is found.

In Shakeri (2005), water surface profiles were measured with a cinematic LIF technique as described there and in the following paragraph. Due to the large horizontal extent of the breaking process, movies were recorded in zones of about 80 cm in width with zone one next to the wave board and zone two starting at about 70 cm away from the wave board.

In the LIF technique, the wave was illuminated with a light sheet from an argon-ion laser operating at 7 W. The light sheet was oriented vertically along the center plane of the tank. Fluorescein dye was mixed into the tank water. The camera (Phantom v9, Vision Research) was set to record 1632×1200-pixel images with 8-bit grey levels at 256 images per second. The camera and light-sheet optics were mounted on the instrument carriage. The intersection of the light sheet and the water surface was viewed by the camera from the side and above the water surface. Wave profiles were extracted from each image using gradient-based edge-detection methods. A detailed description of this measurement system and the data-processing methods can be found in Shakeri (2005) and Shakeri et al. (2009).

LIF photographs taken from the high-speed movies are given in Figure 5.1 and 5.3. These images show various aspects of the wave generation process for 22.5-knot and 27.5-knot equivalent ship speeds at zone1. For both speeds, the selected photographs were taken at 0.0, 0.371, 0.586 and 0.738 s after the start of the wave maker motion, corresponding to $x/L = 0.0$, $x/L = 0.054$, $x/L = 0.091$ and $x/L = 0.144$, respectively. The images in Figure 5.2 and 5.4 show various aspects

of the waves after breaking point for both speeds in zone 2. The photographs were taken 0.816, 0.926, 1.020 and 1.160 s after the start of the wave maker motion, corresponding to $x/L = 0.181$, $x/L = 0.181$, $x/L = 0.227$ and $x/L = 0.285$, respectively. Detailed examination of the zone 1 photographs for the 22.5-knots and 27.5-knots speed cases indicate that there is a plunging jet that produces the main part of the air entrainment in both cases. The size and apparent strength of the main jet increases with the equivalent ship model speed. Though the motion of the wave maker is highly two-dimensional, three dimensionality begins to appear in the free surface after the jet formation process is well underway. This three-dimensionality appears first as ripples on the underside of the jet and the jet tip. Later, after jet impact, the flow becomes fully turbulent and three-dimensional. During this time, the cylinder of air entrapped under the crest at the moment of jet impact breaks down into a cloud of bubbles. Also, a splash region is formed ahead of the jet impact site and drops and bubbles formed, see Figure 5.2(c) and (d) for the 22.5-knot case and Figure 5.4(c) and (d) for the 27.5-knot case. The splash goes as high as the wave crest and becomes more violent as the equivalent ship speed increases (Shakeri 2005). Its likely that a portion of the water in the splash comes from the jet which bounces off the front face of the wave. No specific measurement has yet been made to quantify the source of the water in the splash.

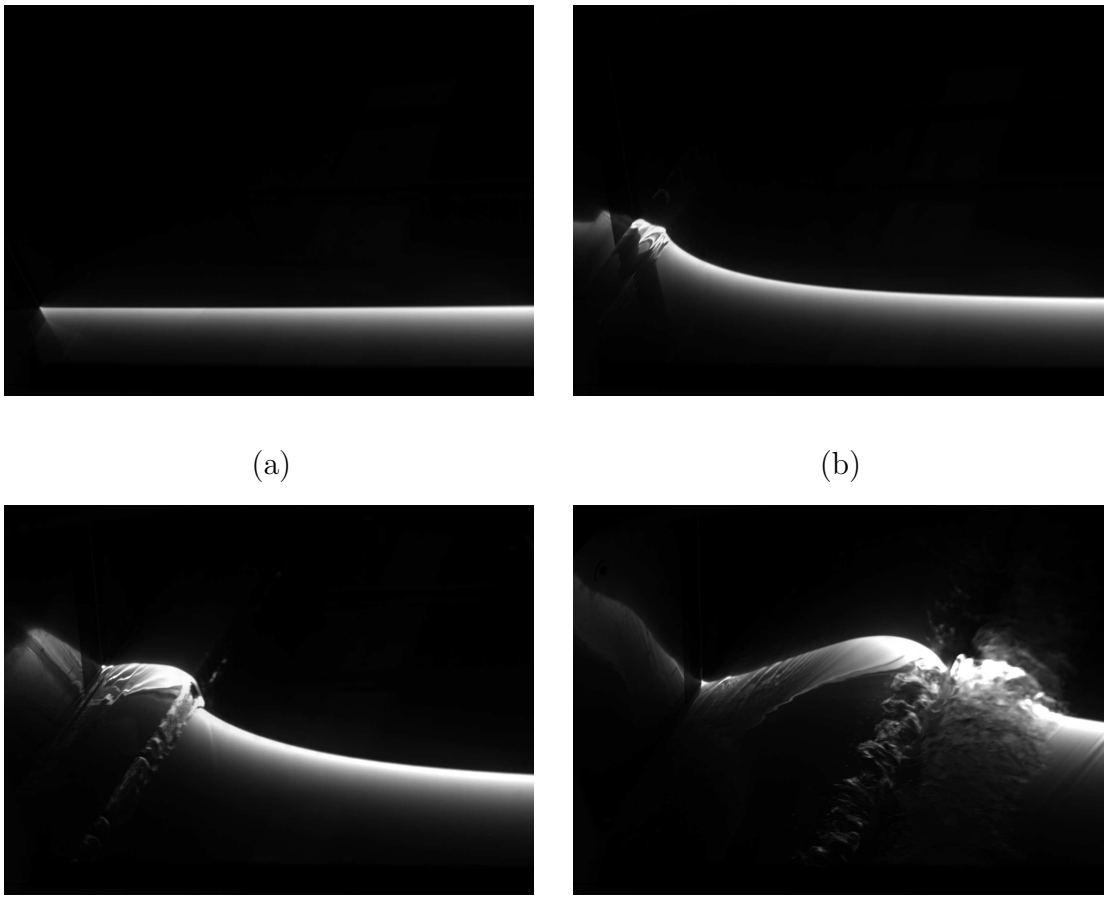

Figure 5.1: LIF images of the wave formation process at four different position along the ship hull in zone 1 ((a) $x/L = 0.0$, (b) $x/L = 0.054$, (c) $x/L = 0.091$ and (d) $x/L = 0.144$) for an equivalent ship speed of 22.5 knots. Each image shows a 70×45 cm section. The high-contrast boundary between the black region on the top of each image and the lighter region on the bottom is the intersection of the laser light sheet and the water surface. The light source for the intensity pattern below this high-contrast boundary is the glowing dye within the subsurface portion of the light sheet. This light either serves to illuminate features like the portion of the plunging jet between the camera and the light sheet as seen in (c) or creates a varied intensity pattern as the subsurface light sheet is viewed through the curved water surface between the camera and the light sheet. More details can be found in Shakeri (2005).

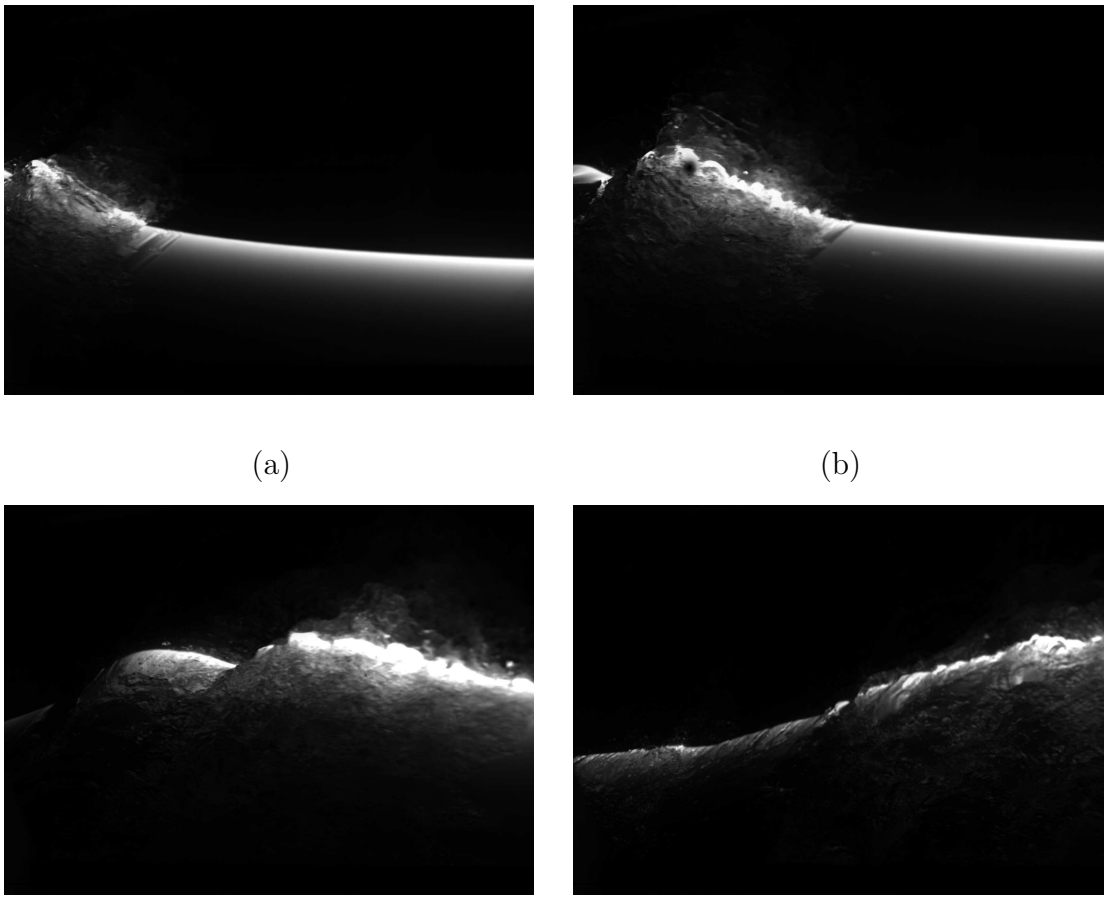

(a) (b)

(c) (d)

Figure 5.2: LIF images showing the splash formation process for an equivalent ship speed of 22.5 knots at four different position along the ship hull, zone 2 ((a) $x/L = 0.181$, (b) $x/L = 0.181$ (c) $x/L = 0.227$ and (d) $x/L = 0.285$))

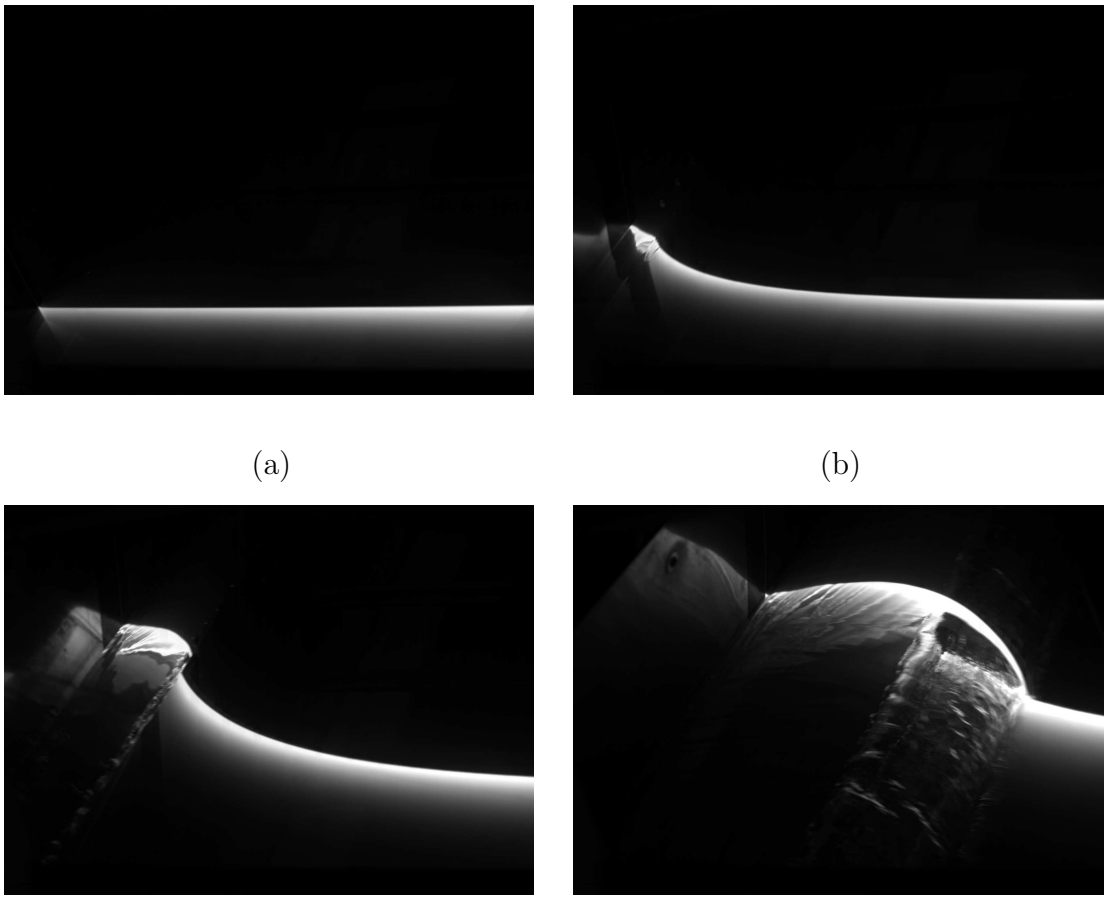

(a) (b)

(c) (d)

Figure 5.3: LIF images of the wave formation process at four different position along the ship hull, zone 1 ((a) $x/L = 0.0$, (b) $x/L = 0.054$, (c) $x/L = 0.091$ and (d) $x/L = 0.144$) for an equivalent ship speed of 27.5 knots.

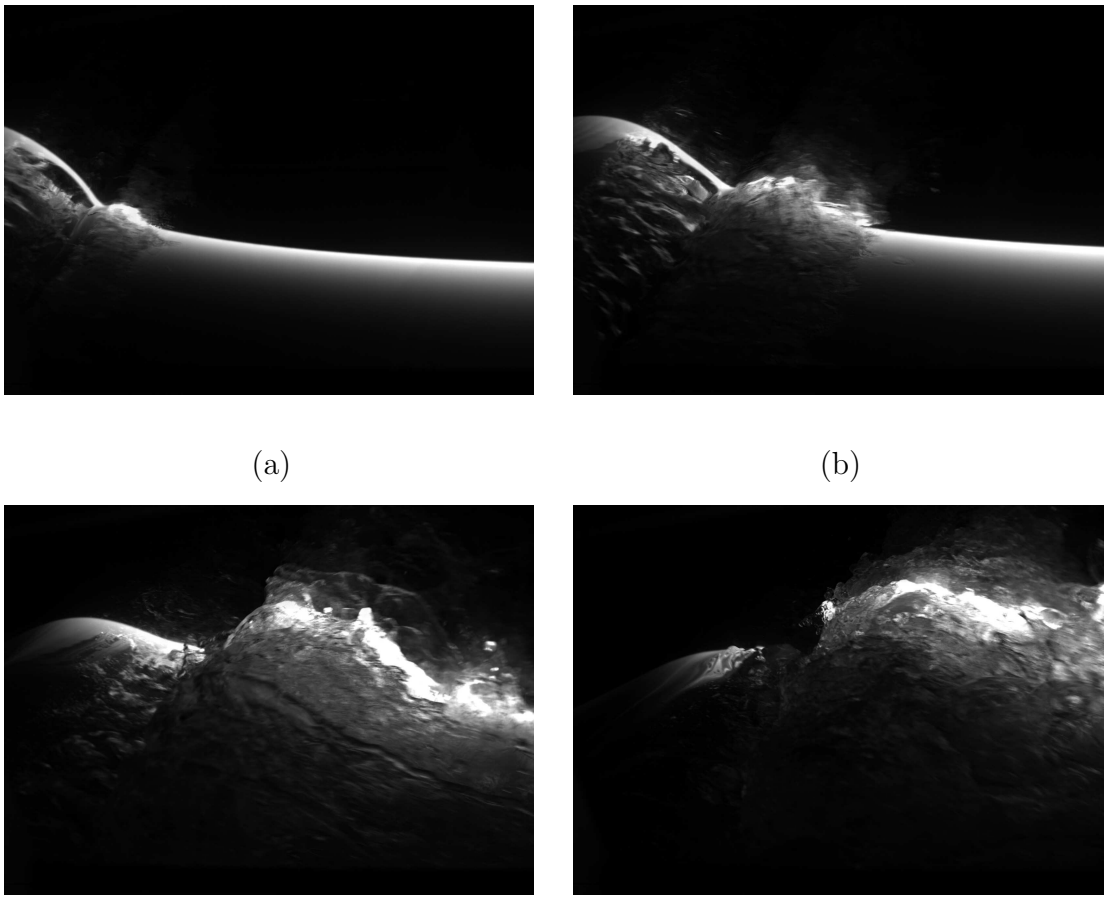

(a) (b)

(c) (d)

Figure 5.4: LIF images of the splash formation process for an equivalent ship speed of 27.5 knots at four different position along the ship hull, zone 2 ((a) $x/L = 0.157$, (b) $x/L = 0.181$ (c) $x/L = 0.227$ and (d) $x/L = 0.285$.

5.2 Repeatability

In order to obtain bubble measurements over the breaking wave and to obtain statistically significant data, the bubble measurements have to be done for many runs for the same breaking wave. Thus, the repeatability of the breaking wave is exceedingly important. In Shakeri (2005), the repeatability of the wave profiles was measured. To this end, wave measurements at each equivalent ship speed were repeated three times and the resulting profiles compared. Three such measured profiles are plotted in Figure 5.5 for the case with equivalent ship speed of 27.5 knots. In addition to the curves from individual runs, curves obtained by averaging the data from the three runs are also presented.

As can be seen in the figures, in regions before the plunging jet impact or away from the ensuing turbulent impact site and splash, the three realizations of the wave profile are nearly identical (to with ± 0.8 mm rms at any instant during a run) and nearly equal to the average profile except for the regions around the jet tip where there are only slight deviations. This shows that the wave maker produces highly repeatable wave motions from run to run. In the impact and splash regions turbulence is created and this adds randomness to the surface profile shapes. Thus, there is a larger run-to-run variation in these regions. To ensure that the same repeatability was encountered in the present experiments, the position versus time of the four drive channels of the wave maker was recorded in every run of the wave maker. It was found that the run to run variations of the difference between the actual drive channel displacement and the desired displacement never varied by

more than 0.8 mm rms at any instant during a run.

The bubble measurements for each ship speed were taken at approximately 200 y-z locations. Since there were only two measurement cameras, this requires 100 experimental runs for each ship speed even if only one bubble image is used at each x-y-z location along the equivalent ship model hull. Since it is only possible to have about 12 runs per day (due to the long wait time required between runs), the time needed to obtain the bubble measurements is prohibitive. Also, subsequent image processing time is long as well. Because of these difficulties, it is important to take only as few repetitions of measurements at each location as are needed to obtain appropriate bubble statistics. In order to determine the number of runs required, repeatability tests with 15 runs were taken for two different x-y-z locations for the 27.5 knot case. At the positions and times chosen, each shadowgraph image contains about 100 bubbles and this is typical of most measurement locations in the subsequent experiments. Figure 5.6 and 5.6 show plots of the average number of bubbles measured versus bubble diameter at the two locations. In each plot, curves are shown for averages of the data from 3, 5, 10 and 15 runs. As can be seen in each plot, the curves obtained from the various numbers of runs are quite close to one another and the maximum error between the curves for the average of three runs compared to the curve for the average of 15 runs occurs at the smallest bubble size and is about 3 bubbles out of 27. Given the relatively small error between the data for 3 runs and 15 runs and the large cost in increasing the number of runs, it was decided to repeat all measurements three times in the subsequent measurement program.

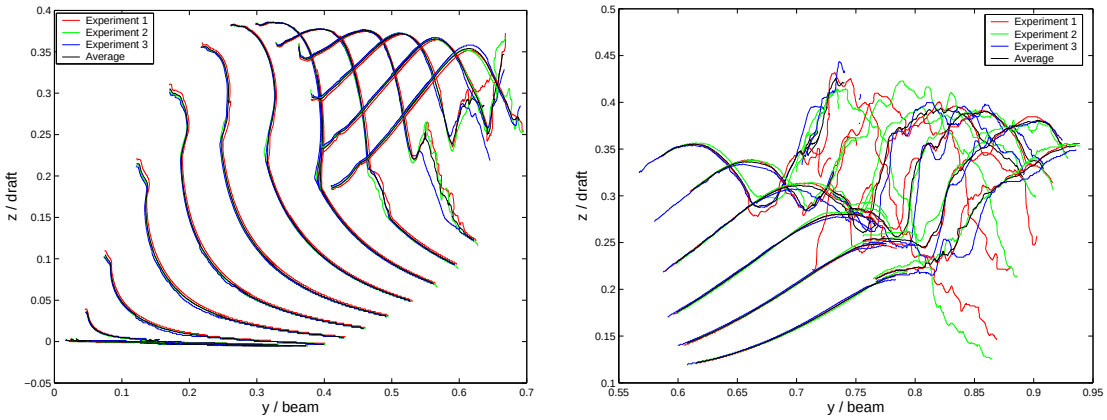

(a) (b)

Figure 5.5: Profile histories of the bow wave generated by the 2D+T wave maker at equivalent ship speed of 27.5 knots from three different runs along with the averaged profile from (a) plunging zone (b) Splash zone ; Time interval between the profiles is 0.078 s; beam(b)=2.82 m and draft(d)=0.914 m.(Shakeri 2005)

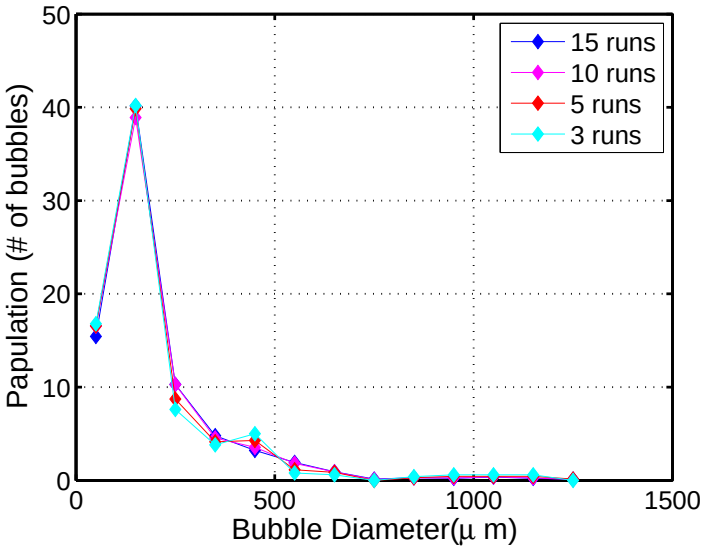

Figure 5.6: Bubble distributions for $U_s = 27.5$ knots at 275 cm away from initial position of the wave maker, 12 cm below the undisturbed water level at $x/L = 0.75$.

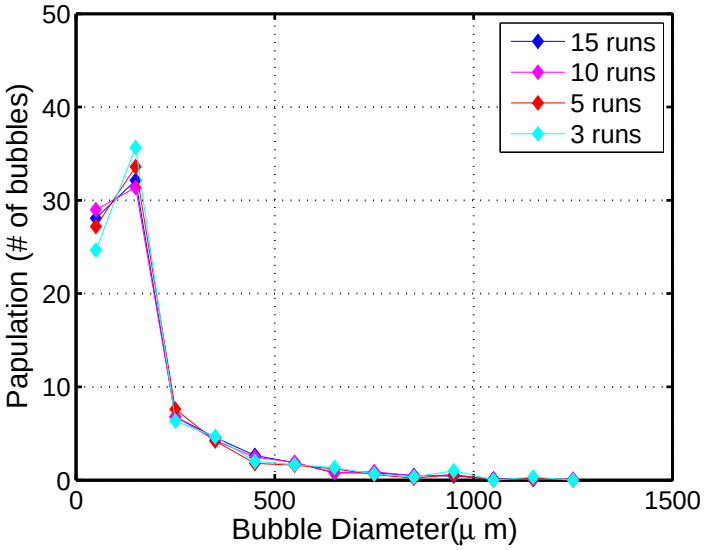

Figure 5.7: Bubble distributions for U_s=27.5knots at 377 cm away from initial position of the wave maker, 08 cm below the undisturbed water level at $x/L = 0.75$.

5.3 Bubble measurements

For each of the two equivalent ship speeds used in this study (22.5 knots and 27.5 knots), the measurements were taken at many locations. As described in chapter 4, at each ship speed, these measurement locations were clustered in two measurement areas that were selected to cover the main parts (bubble clouds) of the bubbly flows. A total of about 90 image pairs were taken during each experimental run at each measurement location and at least three runs were performed for each measurement position, see previous section. From each image pair, the diameter, position, and velocity of the bubbles were measured as described in Chapter 4. In the following, the bubble size distributions are given and discussed first in Section 5.3.1. This followed by void fractions, mean diameters and velocities in Section 5.3.2, Section 5.3.3 and Section 5.3.4 respectively.

5.3.1 Bubble size distributions

The distribution with bubble diameter of the number of bubbles averaged over three runs and over all measurement locations in a given cloud as measured directly from the images are shown in Figure 5.8 . The plots for the first and second clouds for 27.5 knots are shown in Figure 5.8(a) and (b), respectively, while those for 22.5 knots are shown in Figure 5.8(c) and (d), respectively. In each distribution, the number of bubbles measured with diameters in the range to was used with . The raw bubble number distribution was computed from the size estimates by counting bubbles which lay in a chosen range of diameters. The distributions in Figure 5.8 were normalized by the total number of bubbles in each cloud. The data is given for $x/L = 1.00$, corresponding to the location of the stern in the equivalent three-dimensional ship model.

In the raw data plotted in Figure 5.8, the measurement volume is equal to the image area times the depth of field, which varies with bubble diameter, see Section 4.2.1. In order to obtain distributions with the same measurement volume for all bubble diameters (Figure 5.9), the raw data at each bubble diameter in Figure 5.8 is first multiplied by the total number of bubbles measured and then multiplied by the ratio V_T/V where, V_T is the measurement volume for the largest bubbles, $V_T = A_v \times d_T$ where A_v is the area of the field of view of the image and $d_T = 100$ mm (the total measurement depth) and $V = A_v \times d_z$, where d_z is the depth of field for each bubble diameter. The shape of the depth of field curve in Figure 4.7 indicates that the density of small bubbles will increase relative to the density of the larger

bubbles due to this data manipulation. Finally, the corrected distribution is divided by the total number of bubbles corrected for depth of field to obtain the probability density distribution. The maximum error in computing this probability density distribution is 6.3% which is come from the error in the depth of field measurement. Figure 5.9 shows the probability density distributions at $x/L = 1.00$ for 27.5 knots (subplots (a) and (b)) and 22.5 knots (subplots (c) and (d)) for the first and second clouds. Also shown in each plot are curves of the lognormal distribution,

$$P(d) = \frac{exp[-\frac{1}{2}(\frac{ln(d)-m}{s})^2]}{sd\sqrt{2\pi}} \tag{5.1}$$

fitted to the experimental data, where d is the bubble diameter,m is the mean diameter and s^2 is the variance as computer from the experimental data. The blue curves are the lognormal distribution fitted to the experimental data. As can be seen from the figure, the lognormal distribution is fairly good fit to the data for 22.5 knots but not as good for the 27.5 knot data.

The number density of bubbles n_d is the number of bubbles per unit volume which have diameter in the range d to $d + \delta d$, and is therefore a function of the chosen diameter increment (bin width) δd as well as the bubble diameter .

Figures 5.10 to 5.13 show the number density of bubbles for $\delta d = 40\mu\ m$ for five different positions along the ship hull (x/L = 0.5, 0.63, 0.75, 0.87, 1.0), with Figures 5.10 and 5.11 for the first and second cloud, respectively, for the 27.5-knot speed, and Figures 5.12 and 5.13 for the first and second cloud, respectively, for the 22.5-knot speed. The number density of bubbles is obtained from the probability

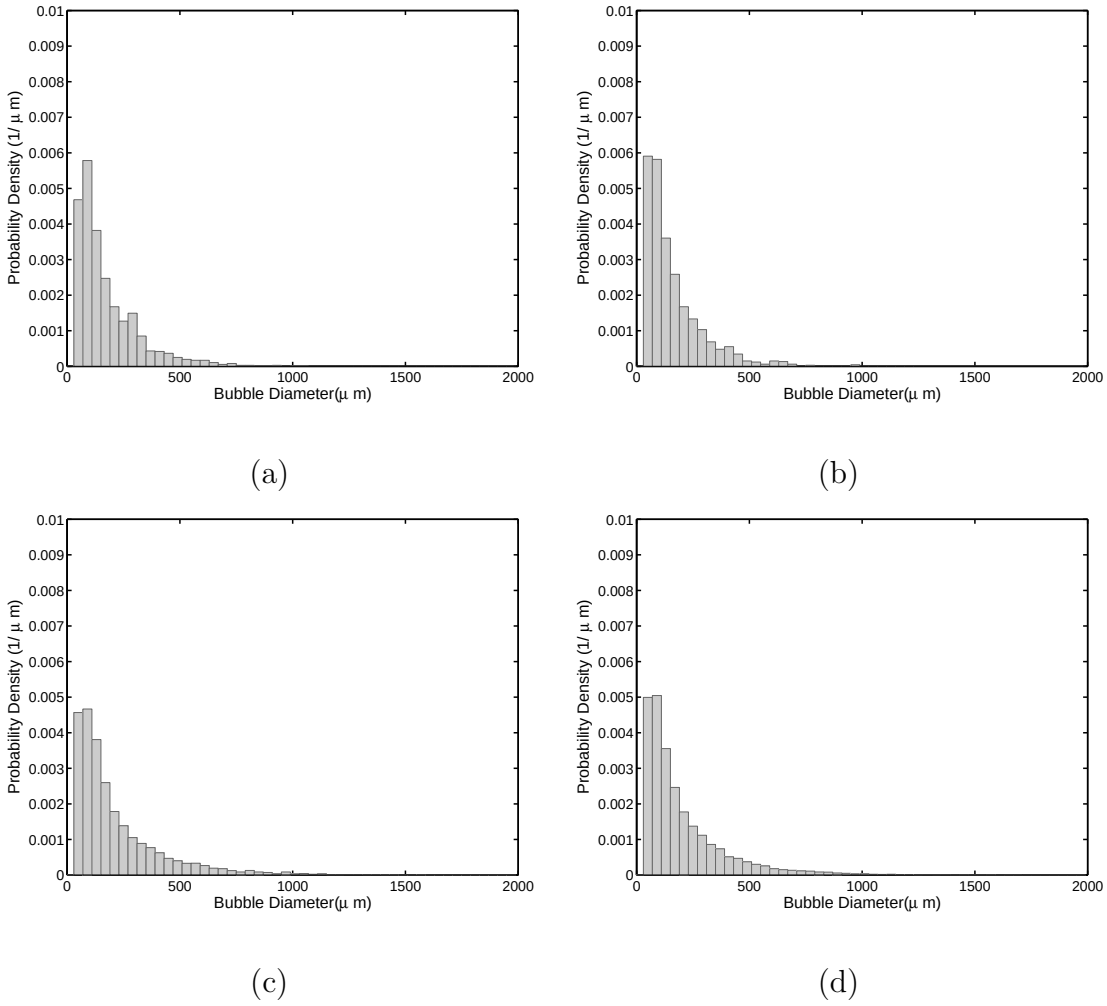

Figure 5.8: Raw bubble distributions directly from shadowgraph images at the stern ($x/L = 1.00$) for two ship speeds for the first and second clouds. (a) 27.5 knots, first cloud, (b) 27.5 knots, second cloud, (c) 22.5 knots, first cloud, (d) 22.5 knots, second cloud.

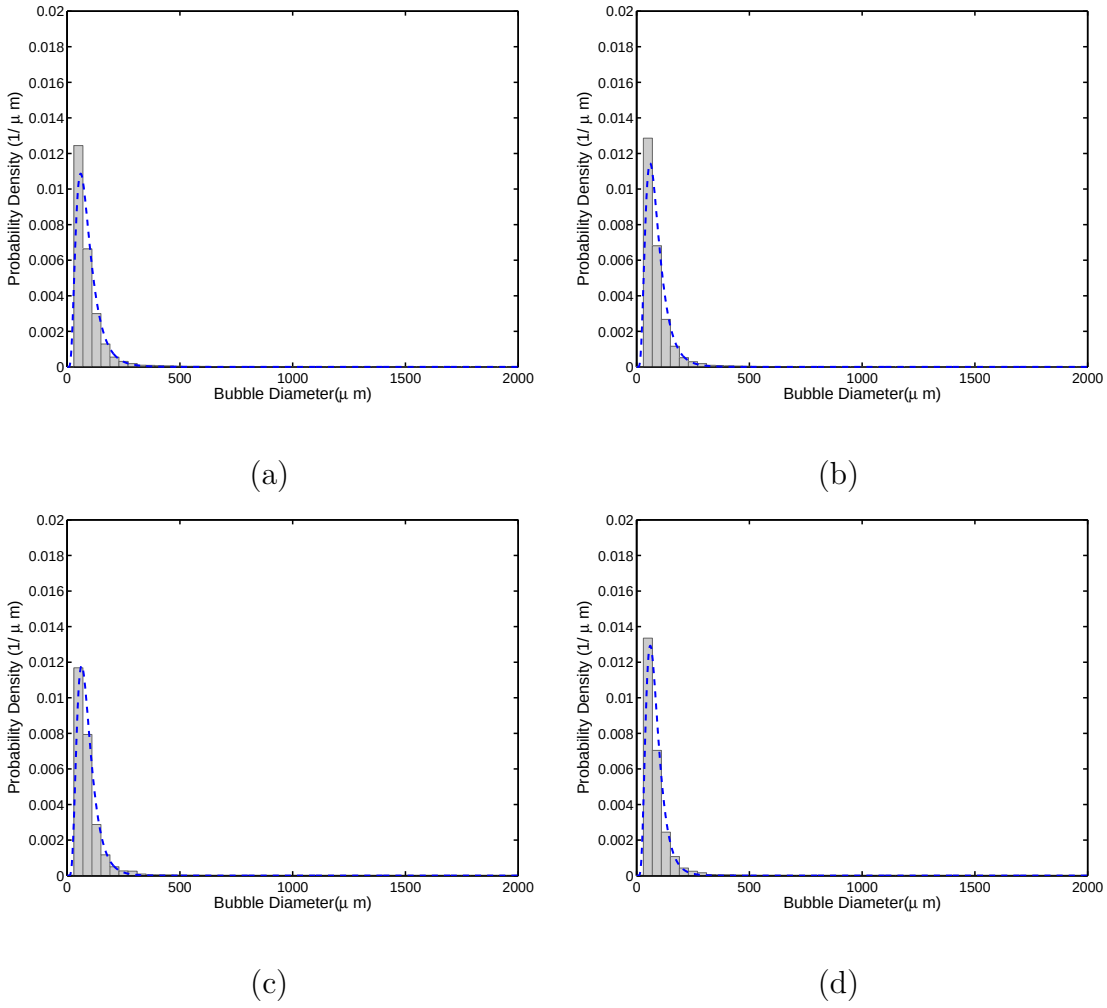

Figure 5.9: Bubble distributions after applying the depth of field correction to the data in Figure 5.9 ($x/L = 1.00$) for two ship speeds for the first and second clouds. (a) 27.5 knots, first cloud, (b) 27.5 knots, second cloud, (c) 22.5 knots, first cloud, (d) 22.5 knots, second cloud. The blue curves are the lognormal distribution fitted to the corrected experimental data.

density distributions like those in Figure 5.10 by multiplying by the total number of bubbles time the ratio of one cubic meter to V_T. Also shown in each plot are curves of the lognormal distribution (red curves),

$$nP(d) = \left(\frac{exp[-\frac{1}{2}(\frac{ln(d)-m}{s})^2]}{sd\sqrt{2\pi} \times V_t}\right) \times n_t \tag{5.2}$$

fitted to the experimental data, where d is the bubble diameter, m is the mean diameter and $s^2$is the variance as computer from the experimental data,n_t is total number of bubbles at each case and V_t is total measurement volume. Again, it can be seen the lognormal distribution is a better fit to the data for the 22.5-knot ship speed than it is for the 27.5-knot ship speed.

Figure 5.14 and 5.15 show log-log plots of the bubble size distributions (the data given in Figure 5.10 to 5.11) for the first and second bubble clouds, respectively, at five different positions along the ship hull for the 27.5-knot case. In log-log coordinates, the bubble distributions show two distinct regions ($d < d_H$ and $d > d_H$) where the data roughly follows separate straight lines. Straight lines in log-log coordinates imply

$$n_d = n_0 \left(\frac{d}{d_H}\right)^{\alpha} \qquad 20\mu\text{m} \leq d < d_H \tag{5.3}$$

$$n_d = n_0 \left(\frac{d}{d_H}\right)^{\beta} \qquad d_H < d \leq 2000\mu\text{m} \tag{5.4}$$

where d_H is the intersection of the straight lines and n_0 is the value of n at the intersection point. (It should be kept in mind that the lognormal distribution would

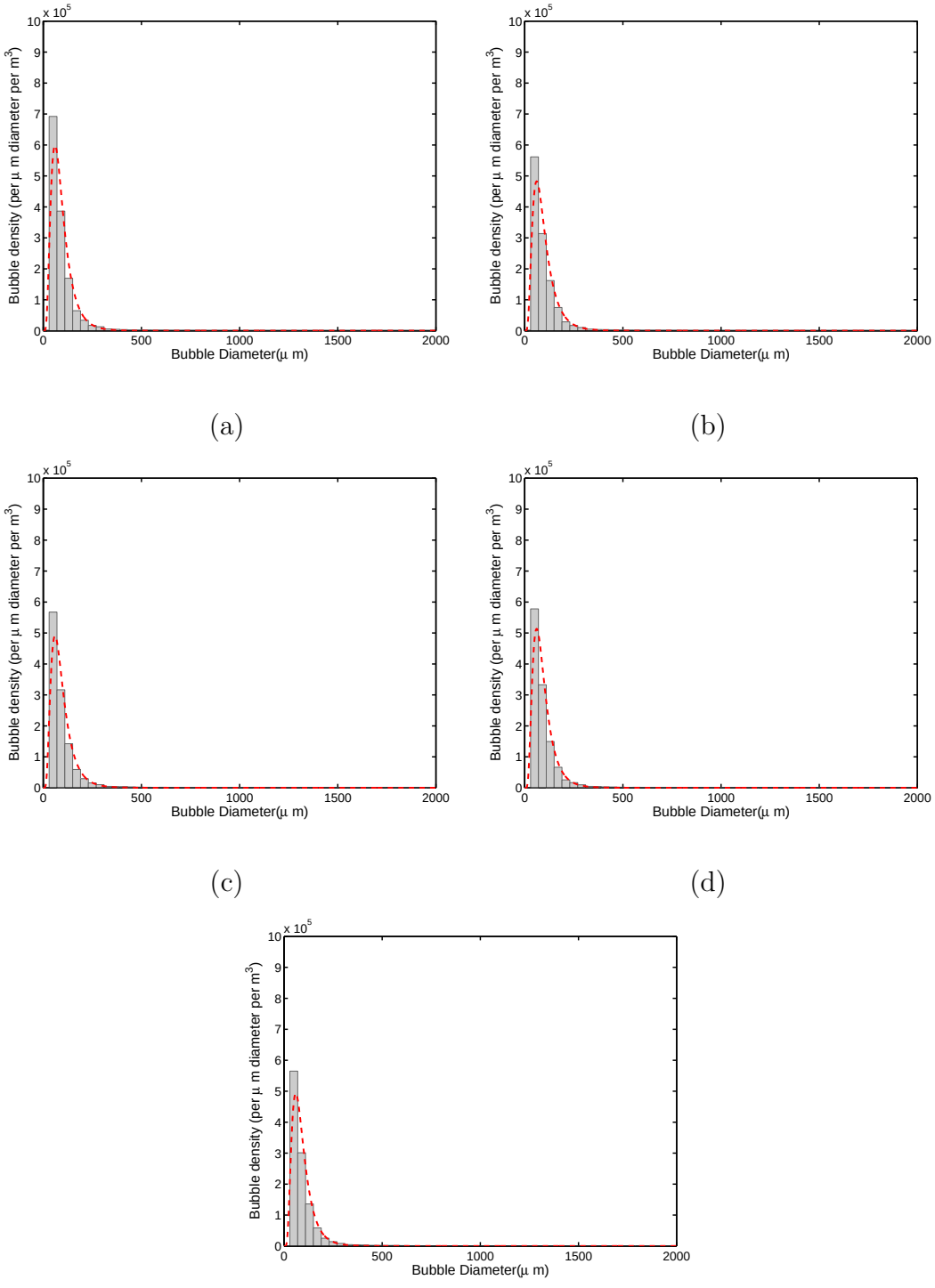

Figure 5.10: Bubble density distributions for a ship speed of 27.5 knots in the first cloud at five times corresponding to five positions along the ship hull ((a) $x/L = 0.5$, (b) $x/L = 0.63$, (c) $x/L = 0.75$, (d) $x/L = 0.87$, (d) $x/L = 1.00$). The red curves are the lognormal distribution fitted to the experimental data.

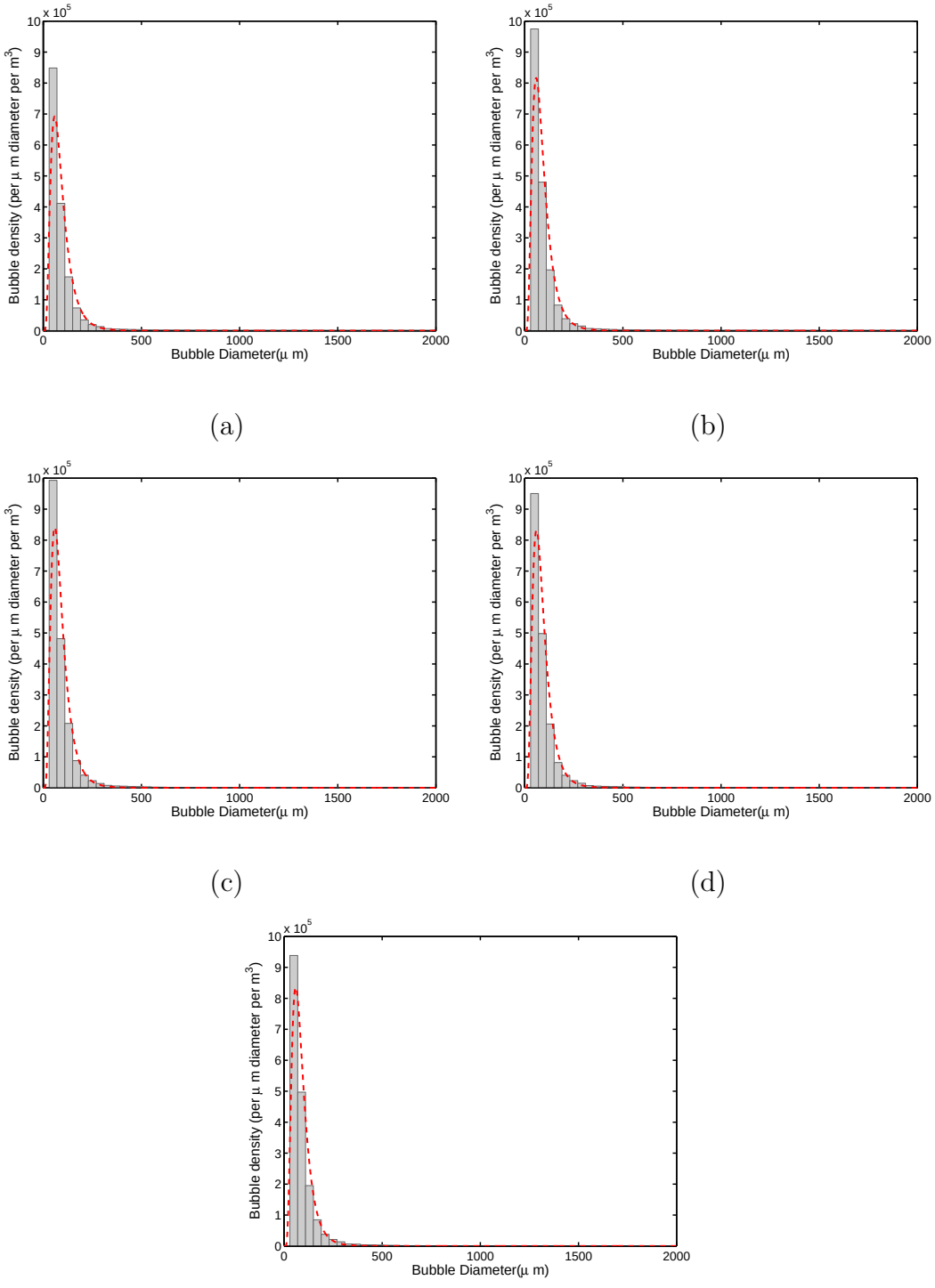

Figure 5.11: Bubble density distributions for a ship speed of 27.5 knots in the second cloud at five times corresponding to five positions along the ship hull ((a) $x/L = 0.5$, (b) $x/L = 0.63$, (c) $x/L = 0.75$, (d) $x/L = 0.87$, (d) $x/L = 1.00$). The red curves are the lognormal distribution fitted to the experimental data.

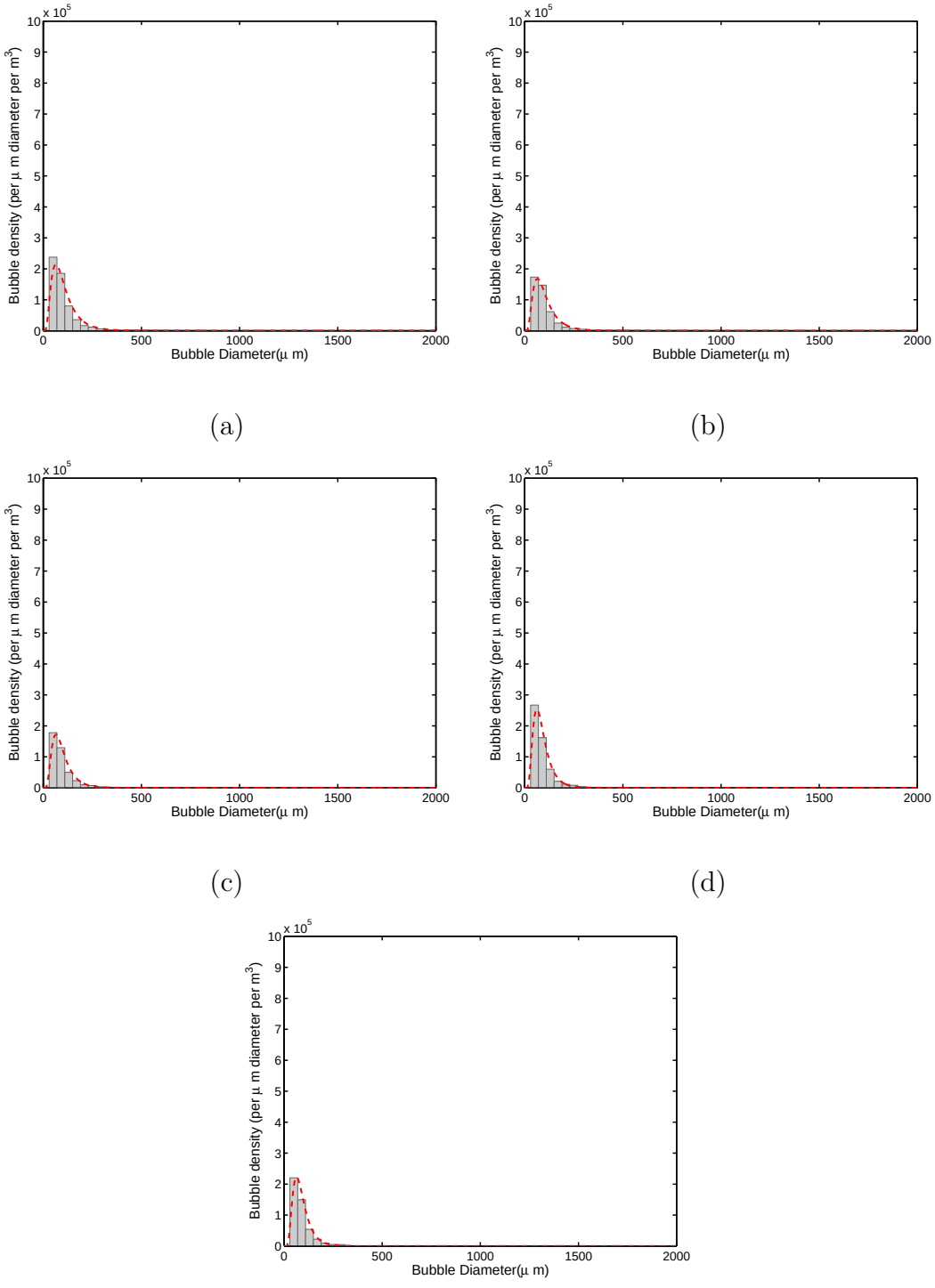

Figure 5.12: Bubble density distributions for a ship speed of 22.5 knots in the first cloud at five times corresponding to five positions along the ship hull ((a) $x/L = 0.5$, (b) $x/L = 0.63$, (c) $x/L = 0.75$, (d) $x/L = 0.87$, (d) $x/L = 1.00$). The red curves are the lognormal distribution fitted to the experimental data.

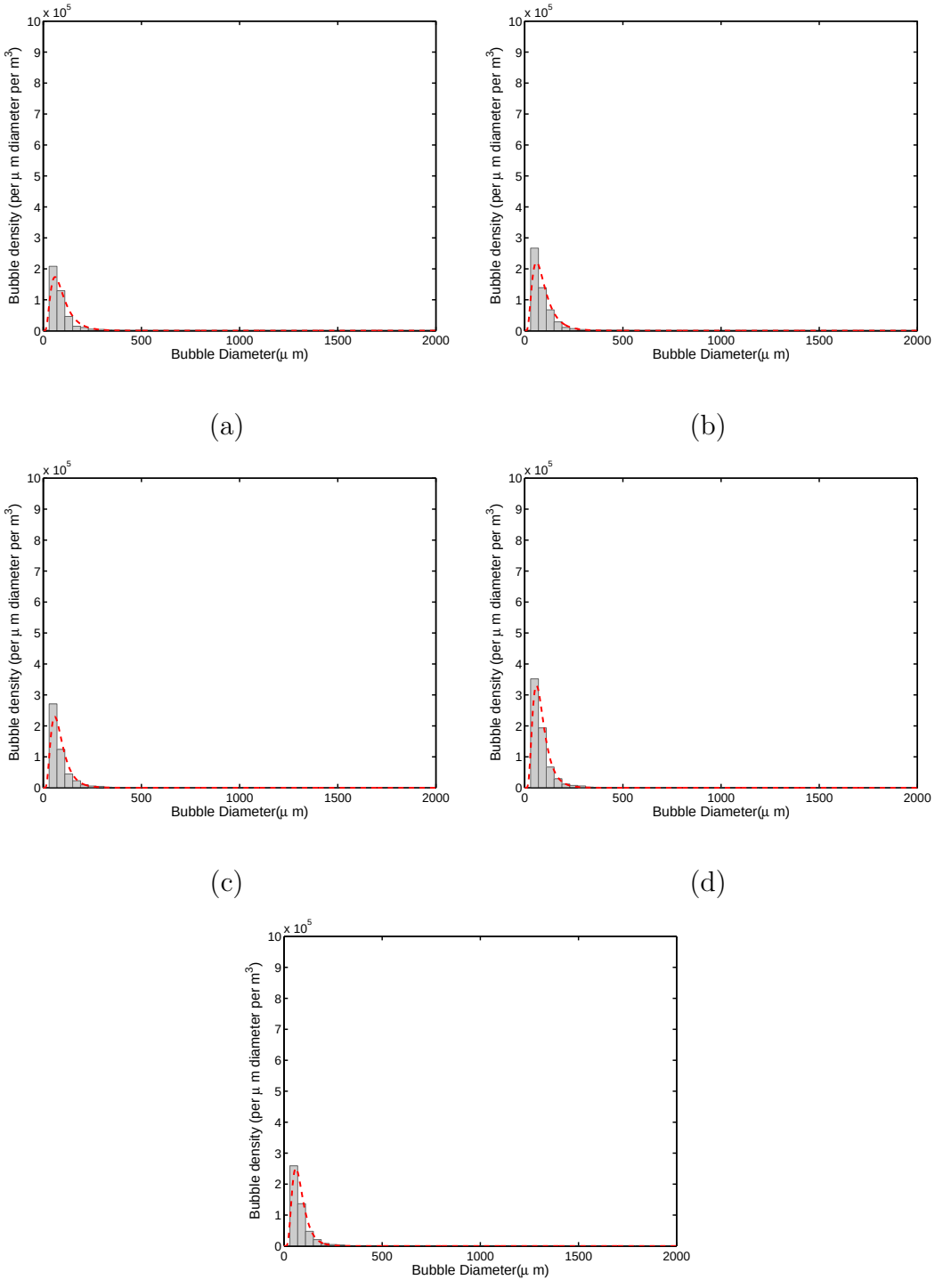

Figure 5.13: Bubble density distributions for a ship speed of 22.5 knots in the second cloud at five times corresponding to five positions along the ship hull ((a) $x/L = 0.5$, (b) $x/L = 0.63$, (c) $x/L = 0.75$, (d) $x/L = 0.87$, (d) $x/L = 1.00$). The red curves are the lognormal distribution fitted to the experimental data.

appear as a single straight line in a log-log plot.) Similarly shaped bubble density distributions were found in deep-water dispersively focused plunging breakers by Deane and Stokes (2001). In the two regions of the bubble density distribution values of α and β were obtained by least squares fit of a straight line to the log-log data in the appropriate range of d with the boundary (d_H) between the two regions (called the large-bubble region and the small-bubble region) determined by an iteration method. In this method, d_H is given an initial guess (typically about 1,000 μm), the data in the two regions is segregated and the straight lines are fitted to the data in the two regions. Next, the value of d at the intersection point of the two straight lines is computed and used as a revised value of d_H. The original data set is then segregated into two regions with the revised d_H. The procedure is repeated until the difference between the newly computed value of d_H and the previously computed value of d_H do not differ by more than 3 μm. The final values of α, β and n_0 are then obtained from the fitted functions.

Plots of d_H and n_0 versus x/L for $U_s = 27.5$ knots are shown in Figure 5.16 (a) and (b), respectively. Data is given for the first and second bubble clouds in each plot. As can be seen from the figure, d_H decreases linearly with x/L and has nearly same value for both clouds for all x/L. The value of d_H decreases slightly from about 875 μm at $x/L = 0.5$ to about 800 μm at $x/L = 1.0$. The n_0 versus x/L data also form nearly straight lines for each bubble cloud. Again the lines are nearly horizontal; however, the values of n_0 are considerably larger for the second bubble cloud, about 800 for the second cloud and about 600 for the second cloud . n_0 is the number of bubbles per unit volume at $d = d_H$ and data show that there are about

30% more bubbles per unit volume of this diameter in the second cloud. In order to examine the differences in the bubble distribution in the two clouds, Figure 5.17(a) show a log-log plot of the bubble density versus d for $U_s = 27.5$ knots at $x/L = 1.0$ for the two clouds. A magnified view of the intersection point is given in Figure Figure 5.17(b). As can be seen in the plots, the values of d at the intersection point for the two clouds are nearly the same while the value of n are quite different.

Figure 5.18 and 5.19 show the bubble size distributions on log-log plots for five different positions along the ship hull for the 22.5-knot equivalent ship speed at the first and second clouds. At this speed, since there are few bubbles larger than 1 mm at each position along the ship hull, the bubble distribution forms nearly a single straight line indicating a power law with exponent a as drawn in the plot.

Given the fit of the two power laws to the bubble density distributions for the 27.5 knot case and the single power law for the 22.5-knot case, we now consider the variation of the power law exponents with x/L. For the 27.5-knot case, the variation of the power-law exponents α and β with distance along the hull (x/L) are shown in Figures 5.20(a) and (b), respectively. Each plot contains data for both the first and second clouds. The values of α for the first (second) bubble cloud shown in Figure 5.20(a) (the exponent for $d < d_H$) start at -2.8 (-2.75) at $x/L = 0.5$ and decrease very slowly, reaching -2.75 (-2.95) by $x/L = 1.0$. The straight lines in the plot (separate lines for the first and second bubble clouds) are least-squares fits to the data. The fact that α is nearly independent of x/L in both clouds indicates that though these small bubbles may move about due to the fluid motion, the effect of buoyancy is insufficient to cause them to leave the flow through the free

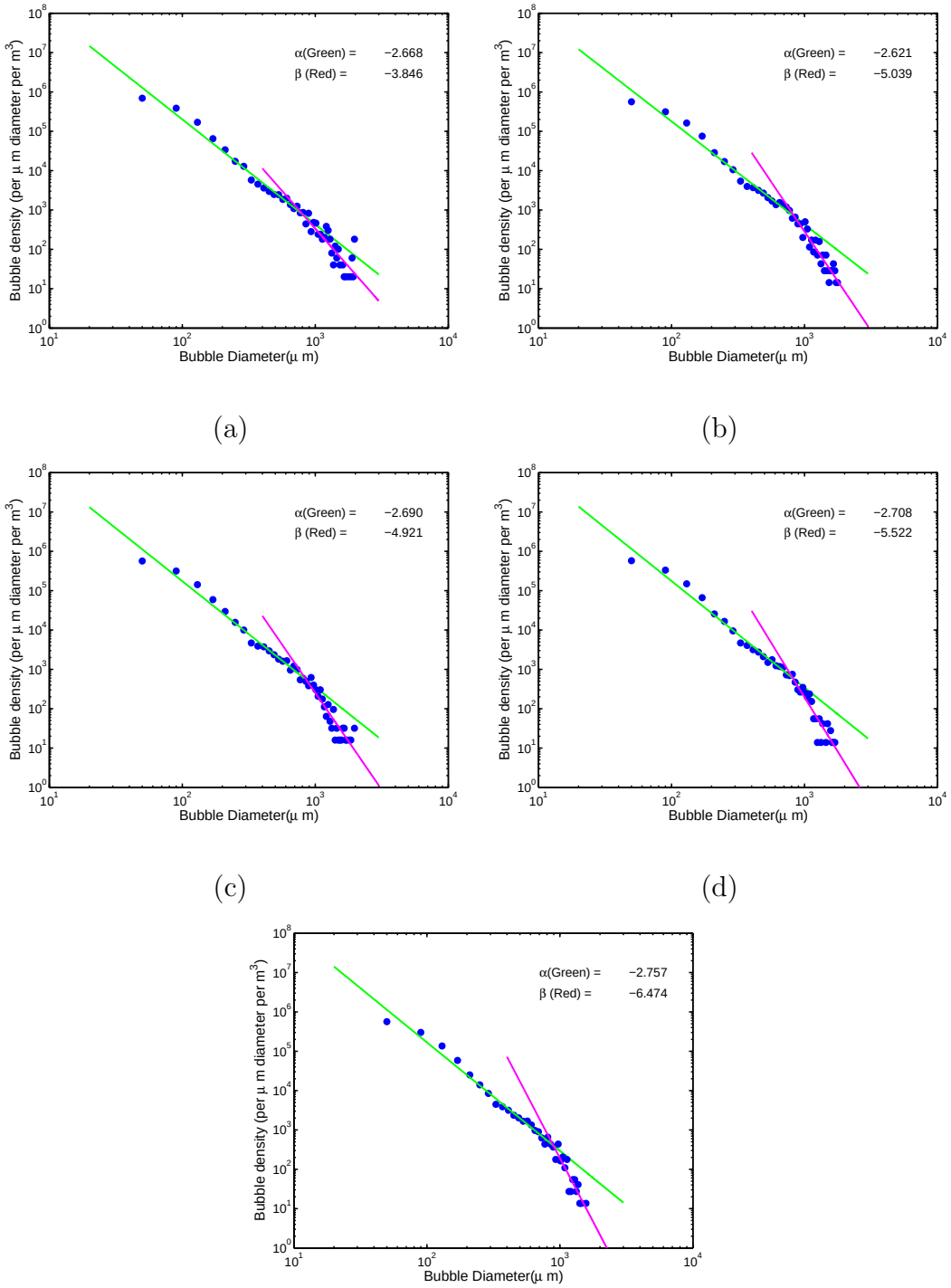

Figure 5.14: Bubble density distributions in log scales for a ship speed of 27.5 knots in the first cloud at five times corresponding to five positions along the ship hull ((a) $x/L = 0.5$, (b) $x/L = 0.63$, (c) $x/L = 0.75$, (d) $x/L = 0.87$, (d) $x/L = 1.00$).

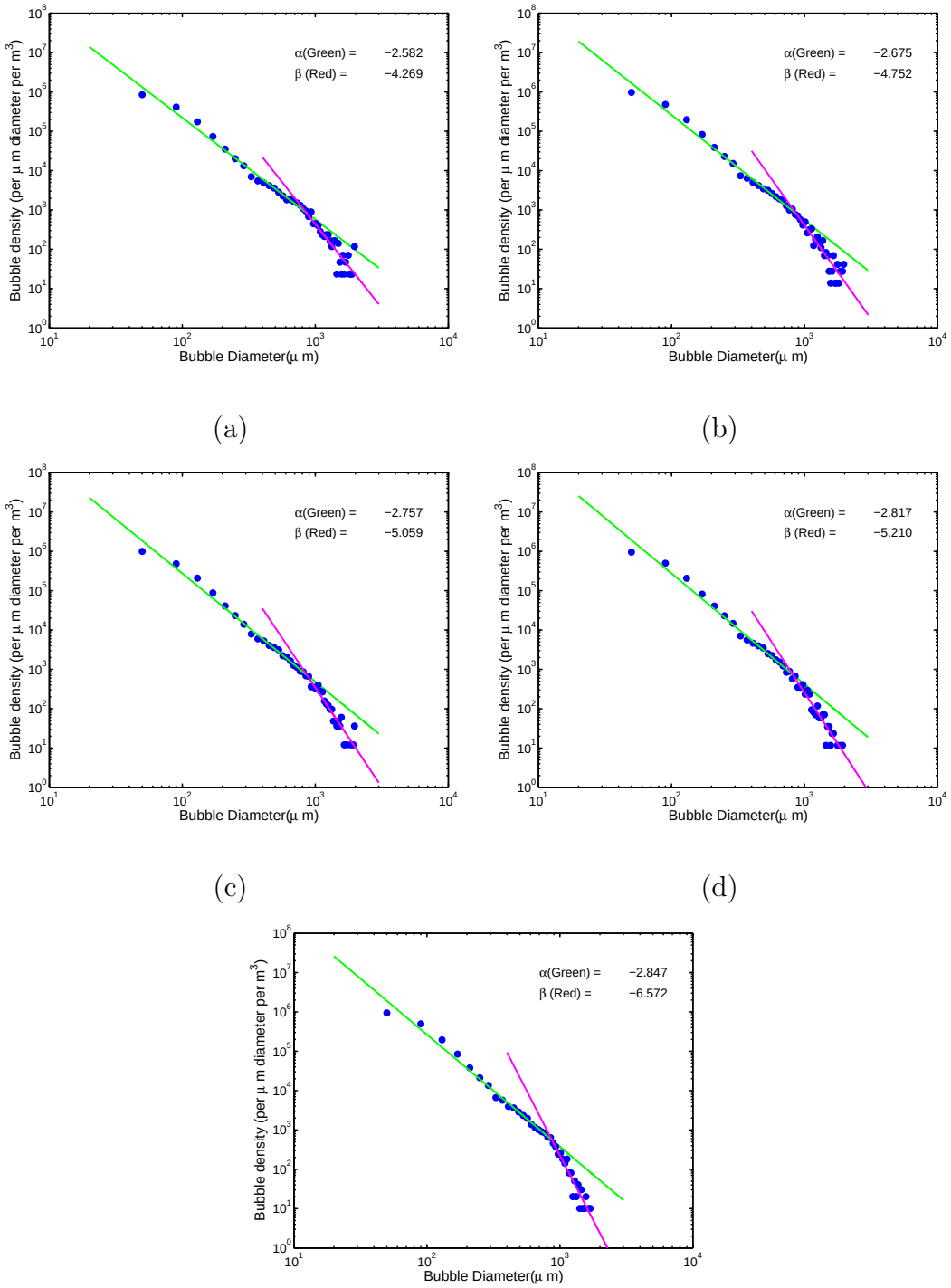

Figure 5.15: Bubble density distributions in log scales for a ship speed of 27.5 knots in the second cloud at five times corresponding to five positions along the ship hull ((a) $x/L = 0.5$, (b) $x/L = 0.63$, (c) $x/L = 0.75$, (d) $x/L = 0.87$, (d) $x/L = 1.00$).

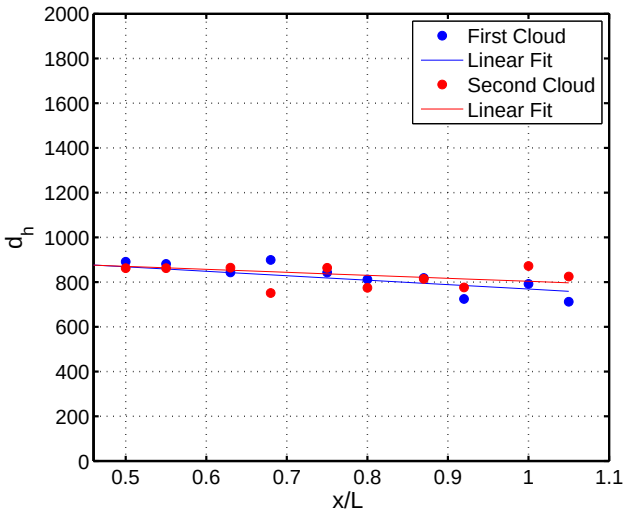

(a)

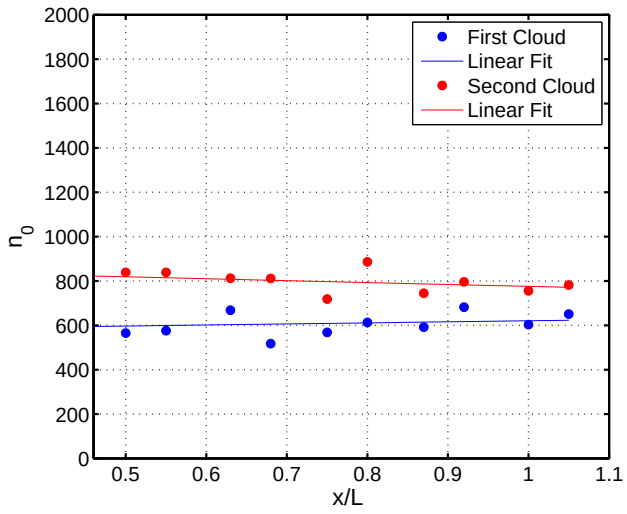

(b)

Figure 5.16: Variation of d_H (subplot (a)) and n_0 (subplot (b)) with distance along the ship hull (x/L) for the 27.5-knot equivalent ship speed for the first and second clouds.

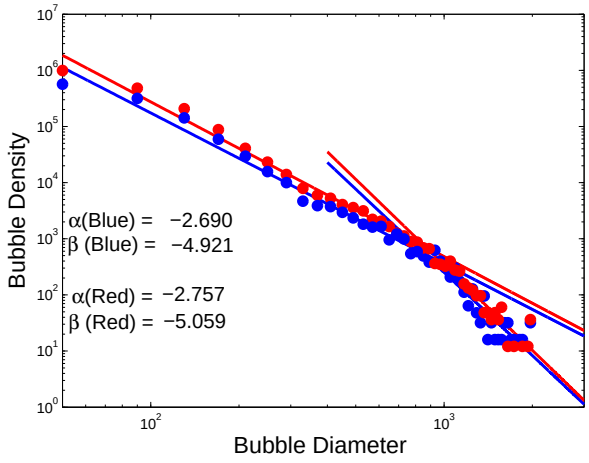

(a)

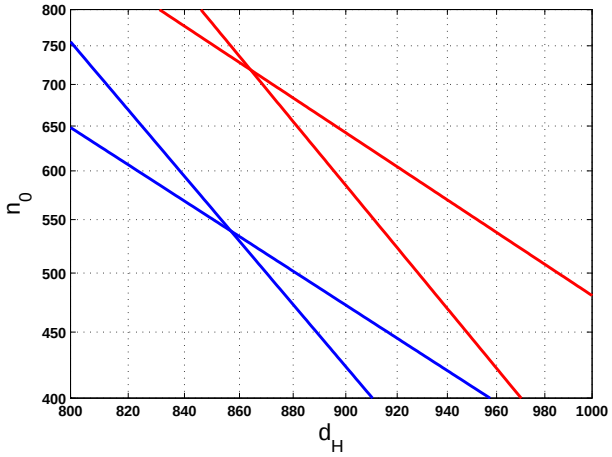

(b)

Figure 5.17: Bubble density distributions for $U_s = 27.5$ knots at $x/L = 1.0$. Data points: first cloud, Data points: second cloud. The lines are from least squares fits of straight lines to the experimental data. (a) full plot. (b): Blow up of the region around the intersection point (d_H, n_0).

surface. Also, it is interesting that the values of α are nearly the same for the two bubble clouds. In contrast, the values of β for the first (second) cloud shown in Figure 5.20(b) (the exponent for $d > d_H$) decrease dramatically (from -3.9 (-6.4) at $x/L = 0.5$ to -4.2 (-6.5) at $x/L = 1$) . The straight lines in the plot are least-square fits to the data. This large rate of decrease of β with x/L in both clouds indicates a significant reduction in the number of larger bubbles, probably due to the influence of degassing caused by their large buoyancy. The values of β are also nearly equal for the two clouds.

The variation with x/L of the exponent (α) in the bubble distribution equation for the 22.5-knots equivalent ship speed is shown in Figure 5.21 for both the first and second bubble clouds. Both slopes are practically constant and nearly equal to one another. Again, the nearly constant value of α is consistent with the idea that most of these small bubbles are not strongly affected by gravity and therefore remain in the flow.

5.3.2 Void Fraction Distribution

In order to obtain the void fraction distribution at each x/L location, the first step was to compute the volume of each bubble (assumed to be spherical) found in the shadowgraph images and then divide by the measurement volume associated with this bubble diameter ($A_v \times d_z$). From this data, the void fraction per unit bubble diameter, per unit bin width (void fraction distribution) was obtained using a logarithmic distribution of bin widths . The logarithmic bin-width distribution

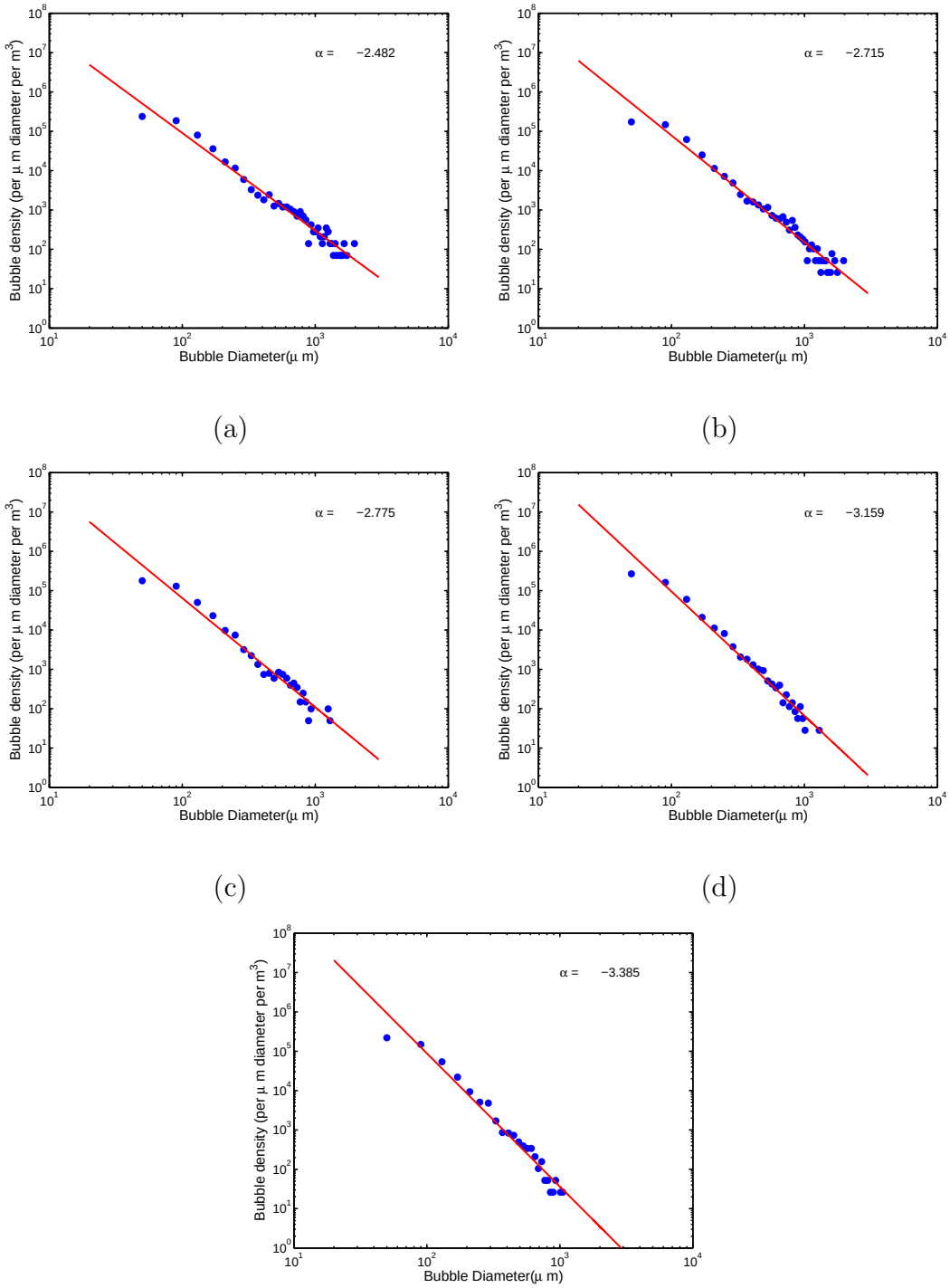

Figure 5.18: Bubble density distributions in log scales for a ship speed of 22.5 knots in the first cloud at five times corresponding to five positions along the ship hull ((a) $x/L = 0.5$, (b) $x/L = 0.63$, (c) $x/L = 0.75$, (d) $x/L = 0.87$, (d) $x/L = 1.00$).

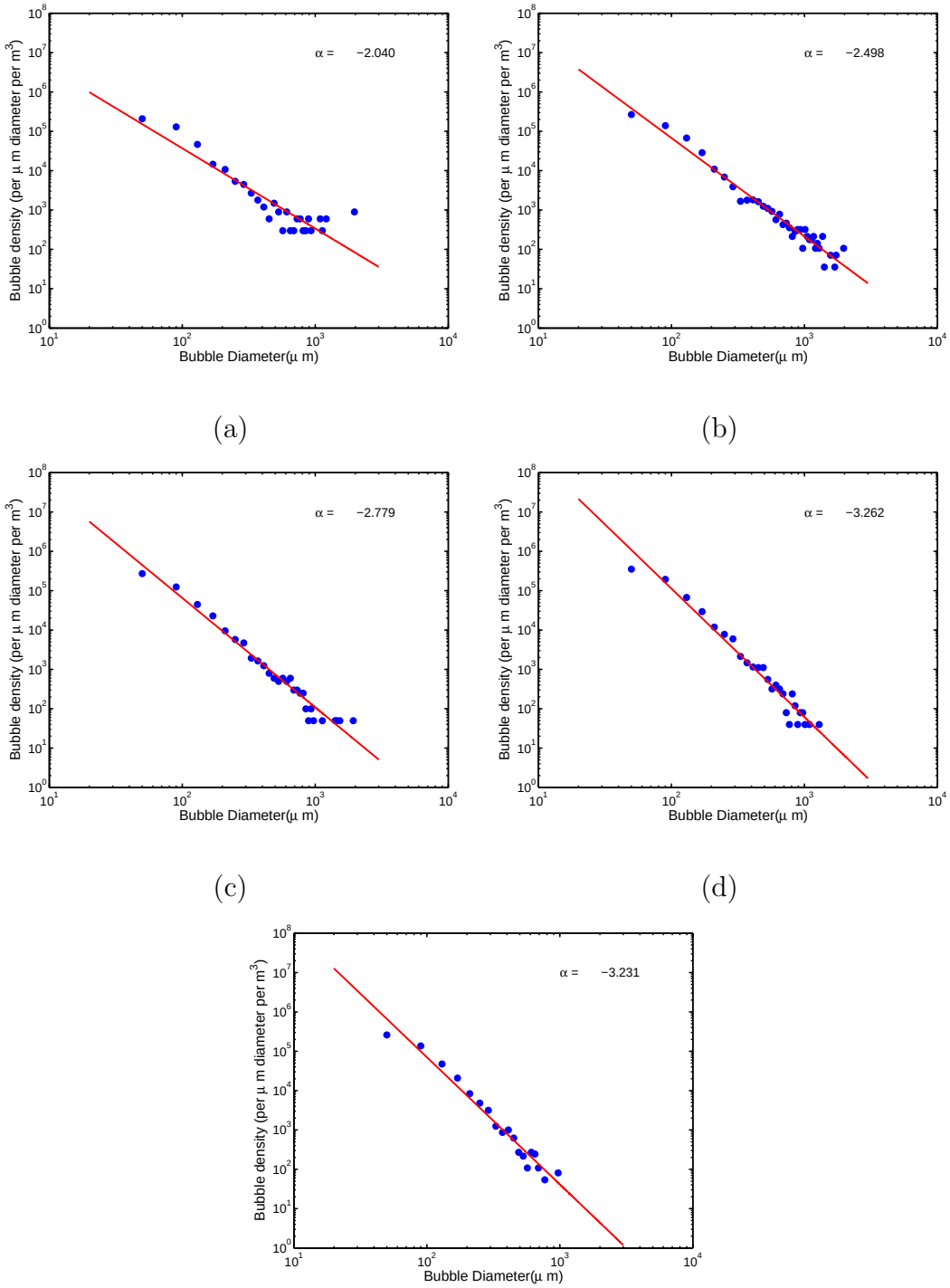

Figure 5.19: Bubble density distributions in log scales for a ship speed of 22.5 knots in the second cloud at five times corresponding to five positions along the ship hull ((a) $x/L = 0.5$, (b) $x/L = 0.63$, (c) $x/L = 0.75$, (d) $x/L = 0.87$, (d) $x/L = 1.00$).

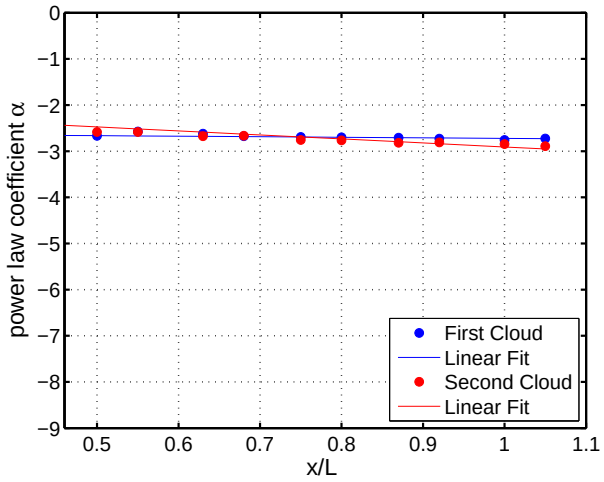

(a)

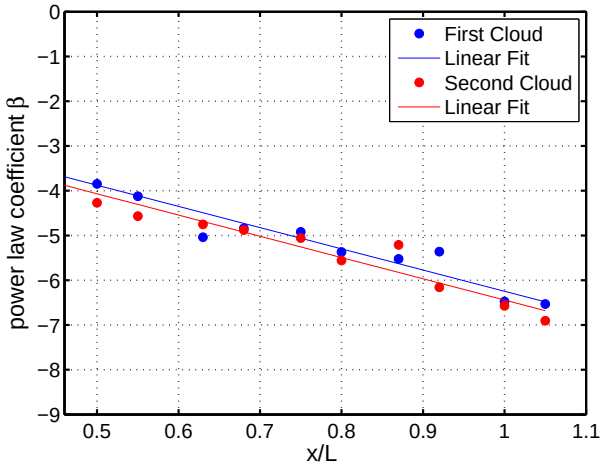

(b)

Figure 5.20: Variation of bubble diameter distribution exponents α (subplot (a)) and β (subplot (b)) with distance along the ship hull (x/L) for the 27.5-knot equivalent ship speed for the first and secend cloud.

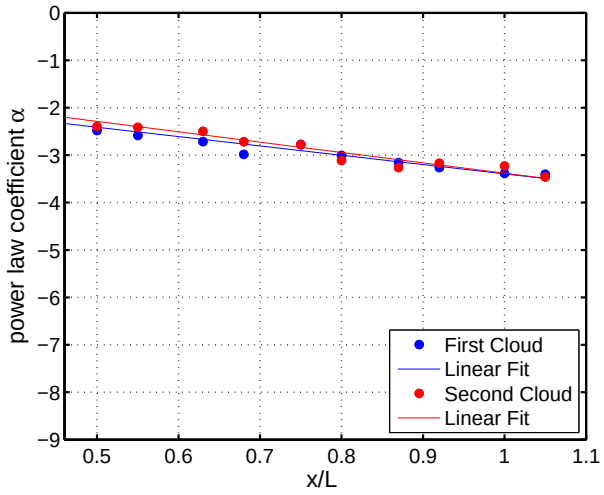

Figure 5.21: Variation of bubble diameter distribution exponents α) with distance along the ship hull (x/L) for the 22.5-knot equivalent ship speed for the first and second cloud.

was used because it has a large bin width at large bubble diameters were the void fraction distribution is large and the measurement sample only includes a few bubbles. Thus, the logarithmic bin-width distribution reduces the noise in the void fraction distribution at large bubble diameters. The normalized void fraction per unit bubble diameter per unit bin width was then obtained by dividing the void fraction distribution by the total void fraction at each position along the ship hull.

Figure 5.22 to 5.25 show the void fraction distributions (subplots (a)) and the normalized void fraction distributions (subplots (b)) at different locations along the ship hull. Figures 5.22 and 5.23 show the distributions for $U_s = 27.5$ *knots* for the first and second clouds, respectively., while Figures 5.24 and 5.25 show the corresponding data for $U_s = 22.5$ *knots*.

As you can see for 27.5-knot cases there is a strong double peak distribution

with d at roughly 150 μm for the first peak and about 800 μm for the second peak with a minimum between the peaks at roughly $d = 325$ μm for all positions along the ship hull. Initially the peaks at larger bubble diameter (second peaks) are bigger than the peaks at the smaller bubble diameters (first peaks), however the second peak drops much more rapidly than the first peak and eventually they become the same height. For the 22.5-knot case, there is plateau for the smaller bubble diameters and there is one peak for the larger bubble diameters. These peaks also drop very fast and become smaller than the void fraction for smaller bubble diameters. Also, the distributions are fairly independent of x/L for the small bubbles, but decrease rapidly with increasing x/L for the larger bubbles. This behavior is predictable from the bubble density distributions in Figure 5.14 and 5.15 , as is discuss below.

Comparing the bubble density distribution in Figure 5.14 to the void fraction distribution in Figure 5.22 it can be seen that the second peak in the void fraction distribution occurs roughly at $d = d_H$ and that the minimum between the two peaks in the void fraction distribution occurs at about the same bubble diameter as the slight dip in the bubble density distribution at d approx equal to 325 μm. Finally, the first peak in the void fraction distribution correspond to the slight curve in the bubble density distribution between d of 20 and 325 μm. To understand the behavior of the second peak we consider how the void fraction distribution is computed from the bubble density distribution. The void fraction within a bubble-diameter bin is defined as the ratio of the volume of air for the bubbles in that bin to the volume of the measurement region in space, and is given by

$$V - F = \frac{V_b}{V} = \frac{\pi}{6V} \int_{d_0}^{d_1} n_d d^3 \ \delta d \tag{5.5}$$

where V_F is the void fraction,V_b is the volume of air for bubbles within the bin with diameter d, V is the measurement volume,d_0 and d_1 , respectively, are the diameter of the largest and smallest bubbles present within the bin. The peak in the void fraction distribution at d_H (second peak) comes about because of the values of the exponents in the bubble density distribution, Figures 5.20. As shown above, the bubble density distribution scales as $d^{-\alpha}$ for $d < d_H$ and $d^{-\beta}$ for $d > d_H$ where α and β are positive constants.

Since bubble volume scales as diameter cubed, the scaling law for the size distribution (times d^3) determines whether large or small bubbles play a dominant role in determining the void fraction. For the 27.5-knot case, just to the right of d_H ($d > d_H$), the bubble density distribution is proportional to $d^{-\beta}$ and β is always bigger than 3 and starts at roughly (3.9) for mid ship and end up at (6.4) for stern, see Figures 5.20. Since the integrand of the above void fraction integral is $n_d d^3 = d^{3-\beta}$ and β is greater than 3, smaller bubbles dominate in determining the void fraction for $d > d_H$. Also, since β increases with x/L, the void fraction decays faster with increasing d as x/L increases. To the left hand side of the maximum at d_H ($d < d_H$), the bubble density distribution is proportional to $d^{-\alpha}$, and α is nearly constant with a value a little less than 3 for all x/L. In this case $n_d d^3 = d^{3-\alpha}$ and since α is smaller than 3, larger bubbles dominate in determining the void fraction. In the 22.5-knot case (Figure 5.21), where a single power law defines the bubble

density distribution, for $x/L < 0.75$, since $\alpha < 3$ the larger bubbles are dominant in the calculation of the void fraction. However, for $x/L > 0.75$, since $\alpha > 3$, the smaller bubbles are dominant.

Subplots (b) of figures 5.22 to 5.25 show the normalized void fraction for 27.5-knot and 22.5-knot cases for the first and second bubble clouds. In contrast to the void fraction plots (subplots (a)), the normalized void fractions at various x/L are different from each other in the range of small bubbles and close to each other for the larger bubbles. Also, the normalized void fraction distribution for the smaller bubble diameters increase with x/L; however, it decreases with x/L for the largest bubble diameters.

The vertical distributions of void fraction at various streamwise locations (x/L) for the first and second bubble clouds for 27.5-knot and 22.5-knot are given in Figure 5.26. For the 27.5 knot case, At all measurement locations there is a peak void fraction located between about 4 cm and 10 cm below the free surface. Below this peak the void fraction tends to zero as the depth increases. The void fraction begins to decrease as depth increase above the depth of maximum void fraction. The void fraction magnitudes and the depths of the void fraction peak are generally larger for smaller x/L.

Figure 5.27 shows the average void fraction for each of the two bubble clouds for the 27.5-knot (subplot (a)) and 22.5-knot (subplot (b)) equivalent ship speeds. As can be seen in Figure 5.27 (a), the average void fraction for the first (second) cloud in the 27.5-knot case decreases from $5.2 \times 10^{-4}(6.0 \times 10^{-4})$ at $x/L = 0.5$ to $2.5 \times 10^{-4}(3.4 \times 10^{-4})$ at $x/L = 1.0$. The straight lines in the plot, which have nearly

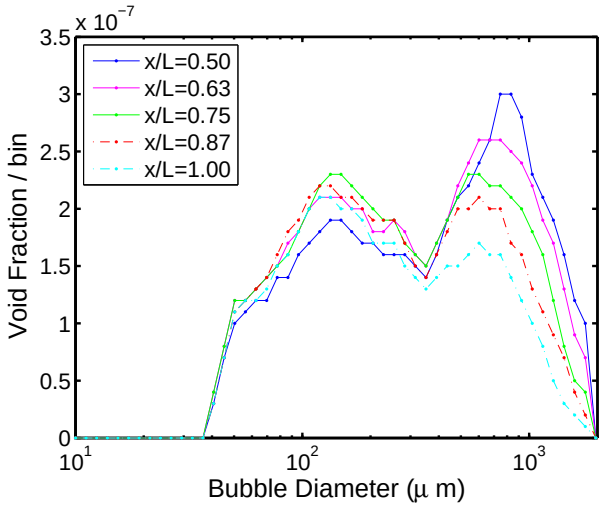

(a)

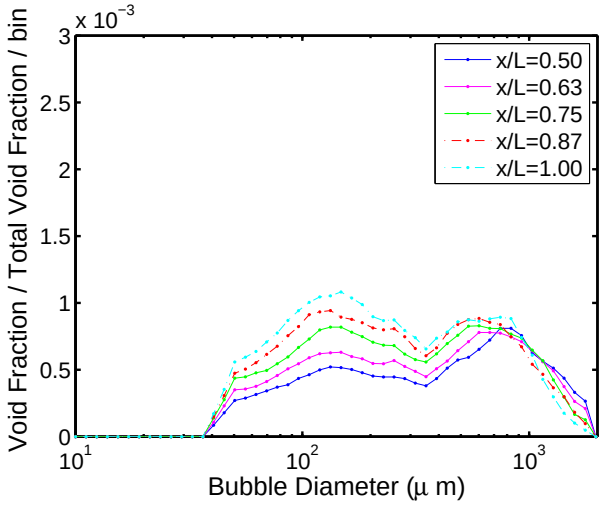

(b)

Figure 5.22: (a) Void Fraction and (b) Normalized void fraction distributions vsersus bubble diameter for a ship speed of 27.5 knots in the first bubble cloud for various values of x/L.

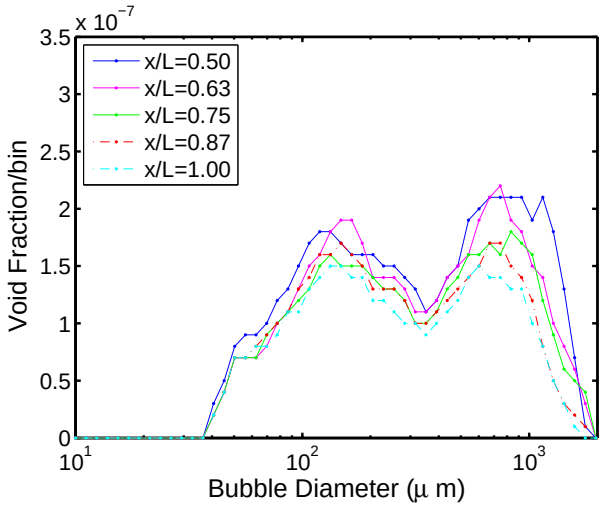

(a)

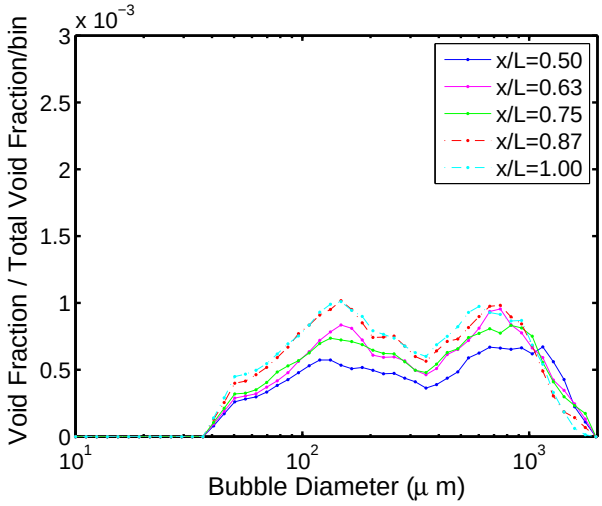

(b)

Figure 5.23: (a) Void Fraction and (b) Normalized void fraction distributions vsersus bubble diameter for a ship speed of 27.5 knots in the second bubble cloud for various values of x/L.

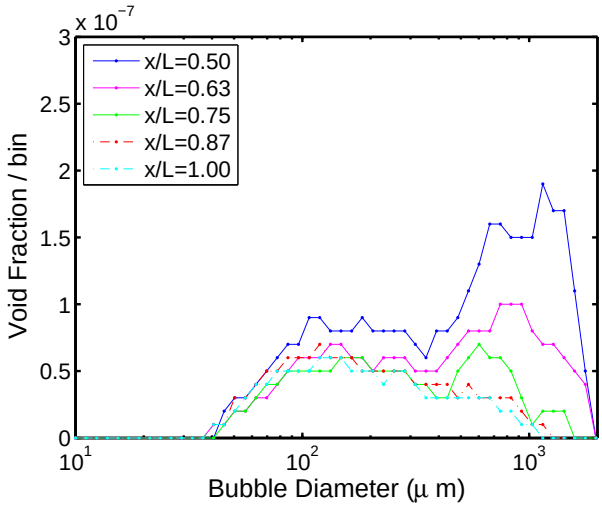

(a)

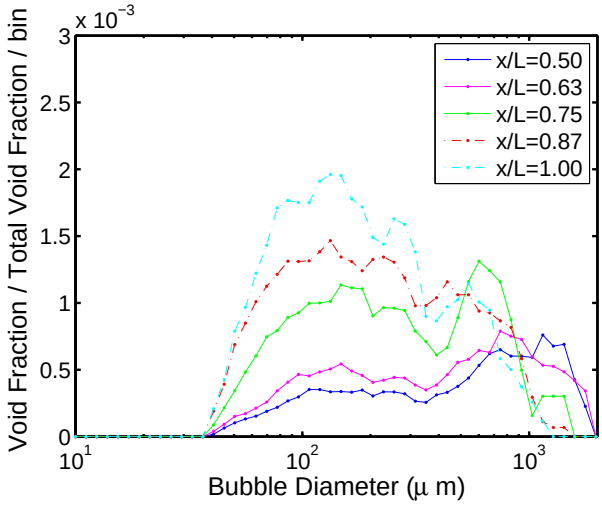

(b)

Figure 5.24: (a) Void Fraction and (b) Normalized void fraction distributions vsersus bubble diameter for a ship speed of 22.5 knots in the first bubble cloud for various values of x/L.

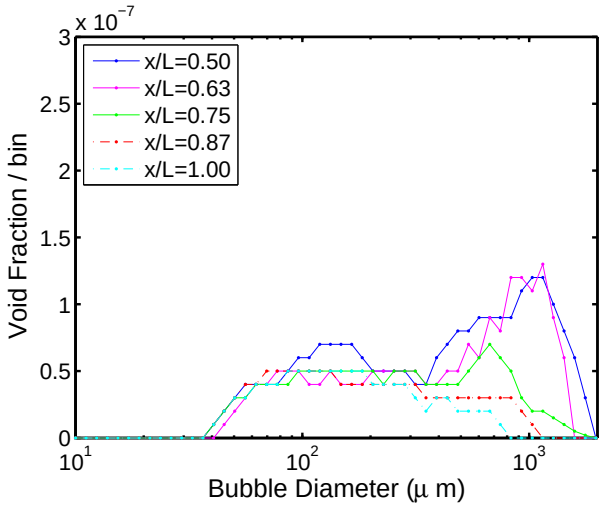

(a)

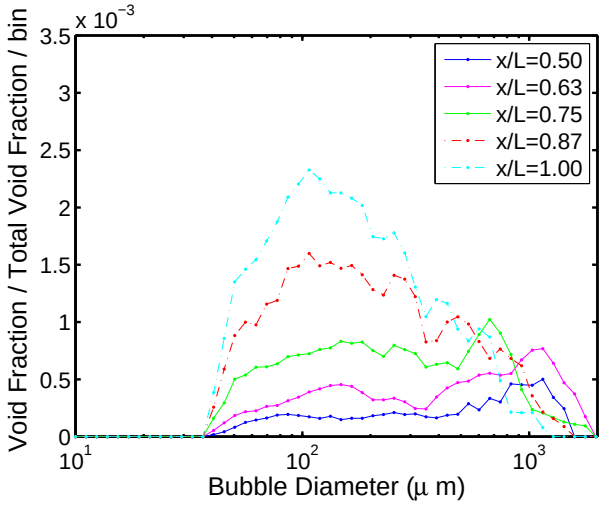

(b)

Figure 5.25: (a) Void Fraction and (b) Normalized void fraction distributions vsersus bubble diameter for a ship speed of 22.5 knots in the second bubble cloud for various values of x/L.

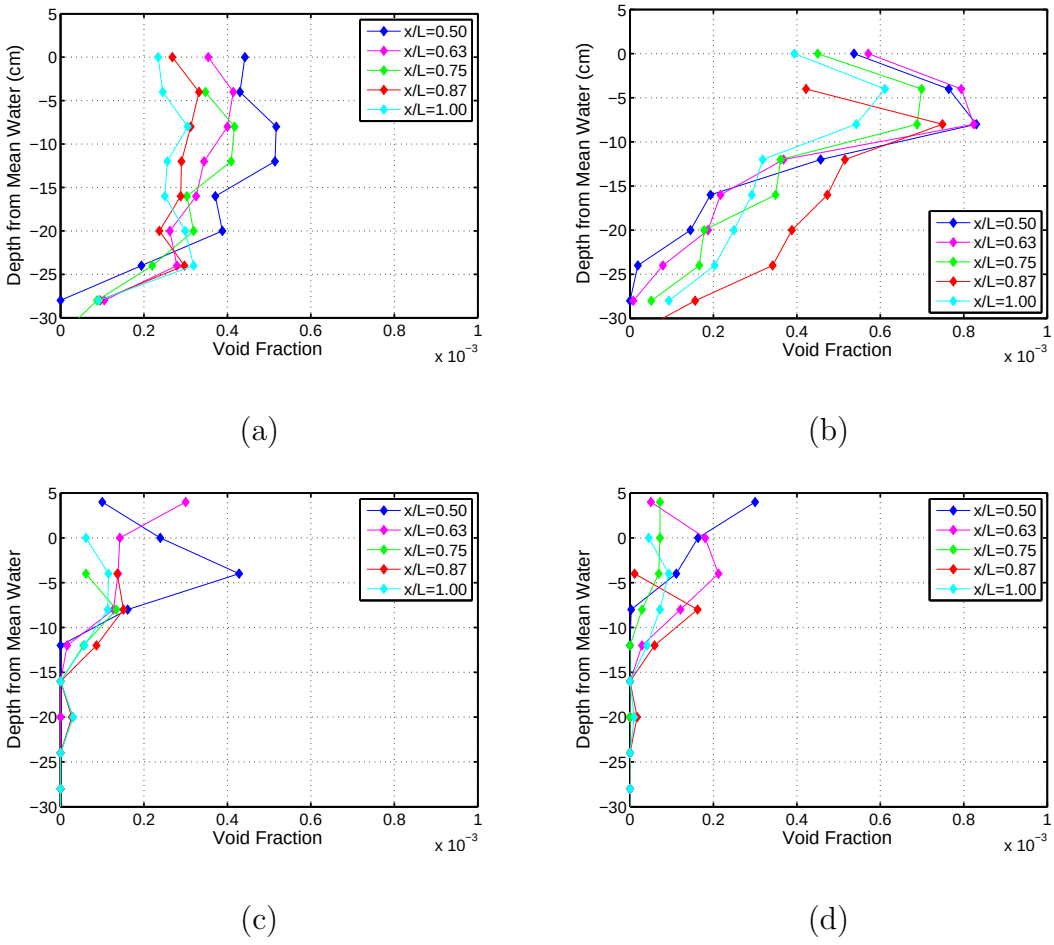

Figure 5.26: Void Fraction versus depth below the mean water level at various values of x/L. (a) 27.5 knots, first bubble cloud, (b) 27.5 knots, second bubble cloud, (c) 22.5 knots, first bubble cloud, and (d) 22.5 knots, second bubble cloud.

the same slope, are least-square fits to the data. The data indicates a nearly 50% reduction in void fraction over the last half of the ship and from the bubble density distributions in Figures 5.14 and 5.15 it can be seen that this void fraction reduction is due primarily to a reduction in the number of large bubbles. It is also interesting to note that the average void fraction of the second bubble cloud is greater than that of the first cloud by about 0.15×10^{-4} at all x/L. As can be seen in Figure 5.27(b), the average void fractions of the two bubble clouds in the 22.5-knot case are nearly equal at all x/L. The void fraction decreases linearly from about 3.5×10^{-4} at $x/L = 0.5$ to about 1.1×10^{-4} at $x/L = 0.75$ and thereafter decreases more slowly to about 0.9×10^{-4} at $x/L = 1.1$. This break in slope may indicate that most of the large bubbles have left flow by $x/L = 0.75$ and this hypothesis is explored below in the discussion of the distributions of the Sauter mean diameter.

Figures 5.28to 5.31 show the void fraction contours in planes of constant x/L for the first and second bubble clouds for the 27.5-knot (Figures 5.28 and 5.29) and 22.5-knot (Figures 5.30 and 5.31) cases for five different positions along the ship hull (x/L=0.5, 0.63, 0.75, 0.87, 1.0). It should noted that in spite of the very long measurement campaign in the present experiments, while there are many bubbles in the samples for the entire bubble clouds and in the distributions of various quantities with depth, the number is bubbles in a sample at a given y-z location at each x/L is much smaller, particularly for the numbers of larger bubbles. Thus, the average void fraction at each location is a bit noisy. In spite of this deficiency, some patterns can be detected in the contour plots. In particular, in the first cloud for the 27.5-knot case (Figure 5.28) the orientation of the void fraction contours are more or less

tilted at 45 degrees. This may be related in some way to the strong plunging jet in this case. This 45-degree orientation is not apparent in the contours for the second cloud of the 27.5-knot case (Figure 5.30) and this may be related to the more diffuse entrainment process under the splash. No specific patterns are identifiable in the contours for either cloud in the 22.5-knot case.

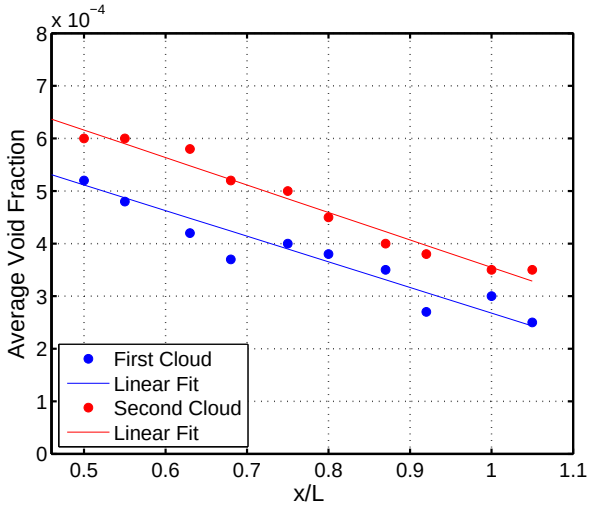

(a)

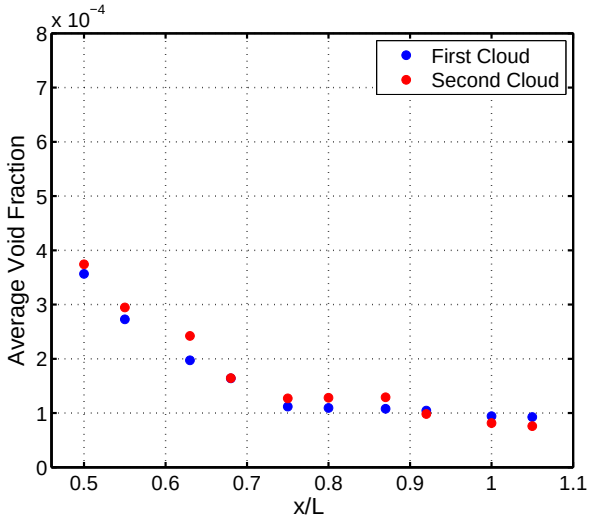

(b)

Figure 5.27: (a) Void Fraction and (b) Normalized void fraction distributions vsersus bubble diameter for a ship speed of 22.5 knots in the second bubble cloud for various values of x/L.

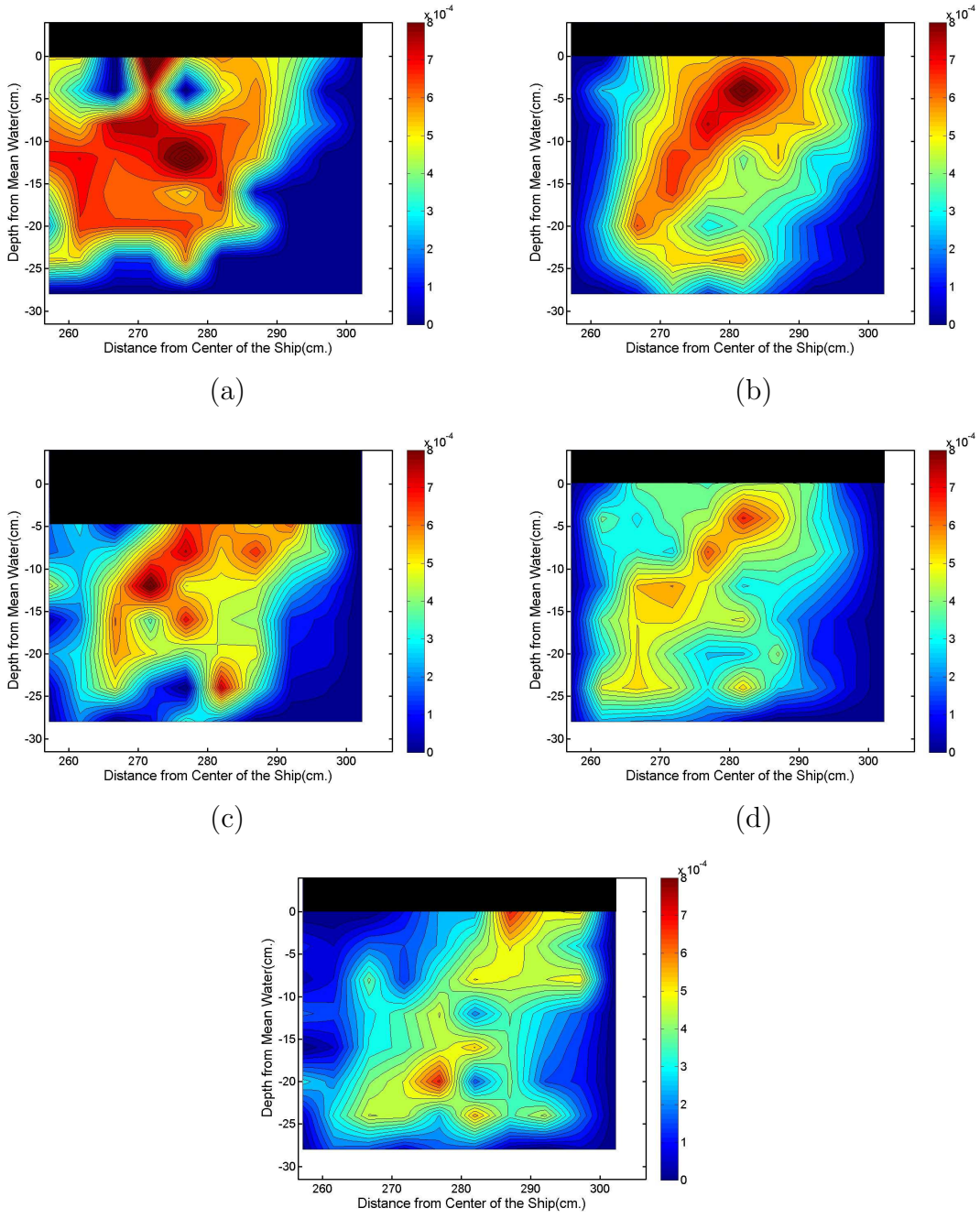

Figure 5.28: Void fraction contours in $y-z$ planes for $U_s = 27.5$ knots in the first bubble cloud for values of ((a) $x/L = 0.5$, (b) $x/L = 0.63$, (c) $x/L = 0.75$, (d) $x/L = 0.87$, (d) $x/L = 1.00$).

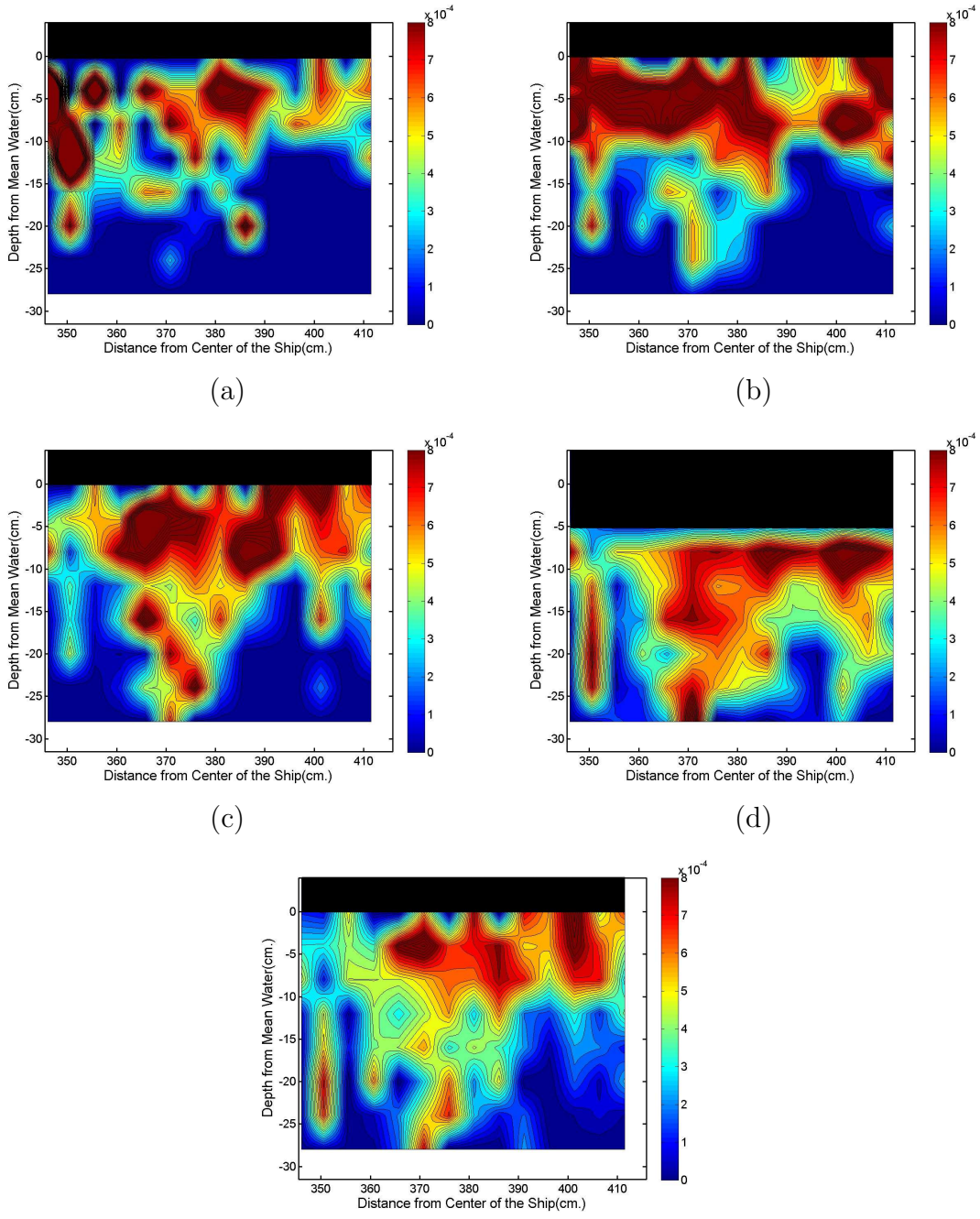

Figure 5.29: Void fraction contours in $y-z$ planes for $U_s = 27.5$ knots in the second bubble cloud for values of ((a) $x/L = 0.5$, (b) $x/L = 0.63$, (c) $x/L = 0.75$, (d) $x/L = 0.87$, (d) $x/L = 1.00$).

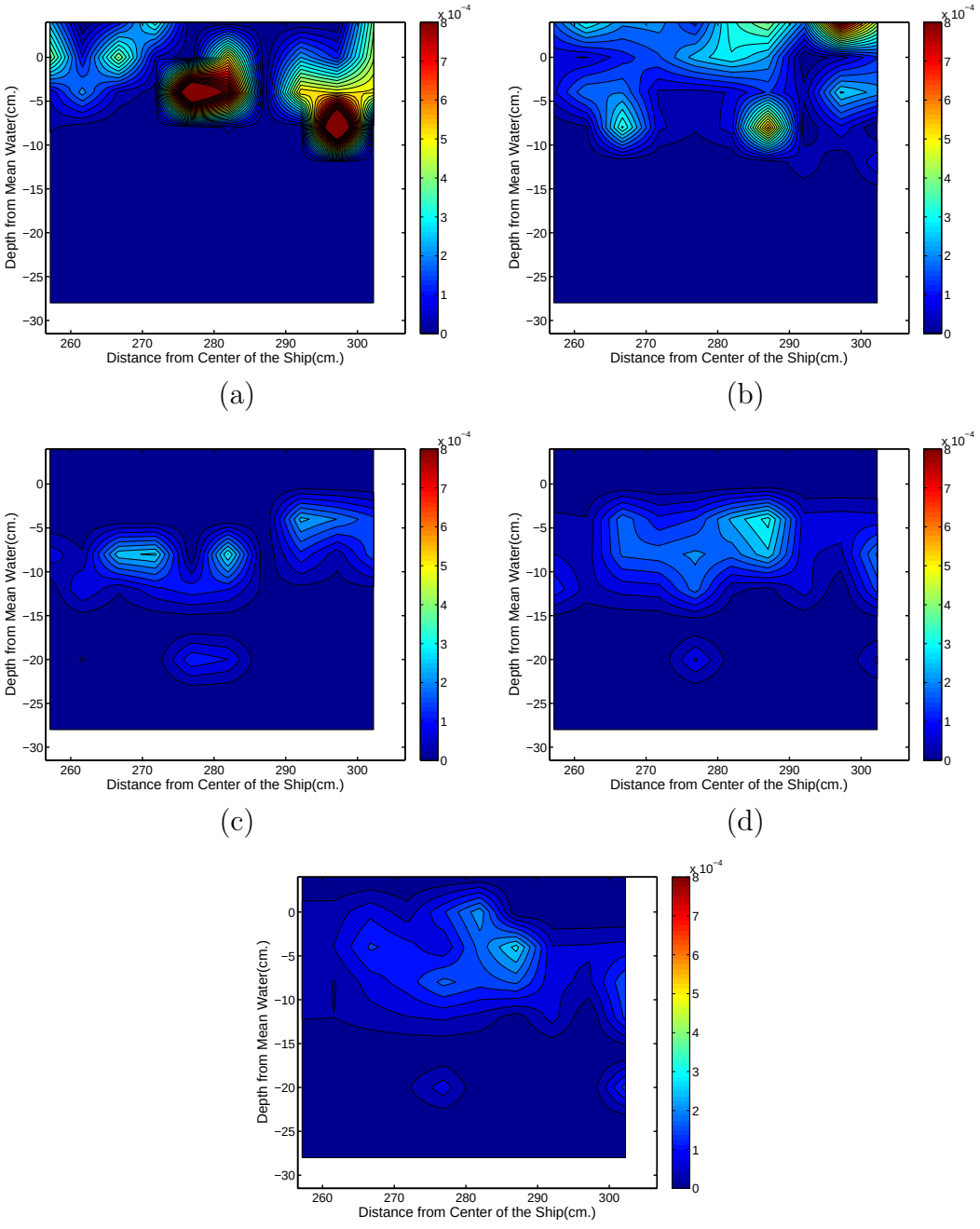

Figure 5.30: Void fraction contours in $y-z$ planes for $U_s = 22.5$ knots in the first bubble cloud for values of ((a) $x/L = 0.5$, (b) $x/L = 0.63$, (c) $x/L = 0.75$, (d) $x/L = 0.87$, (d) $x/L = 1.00$).

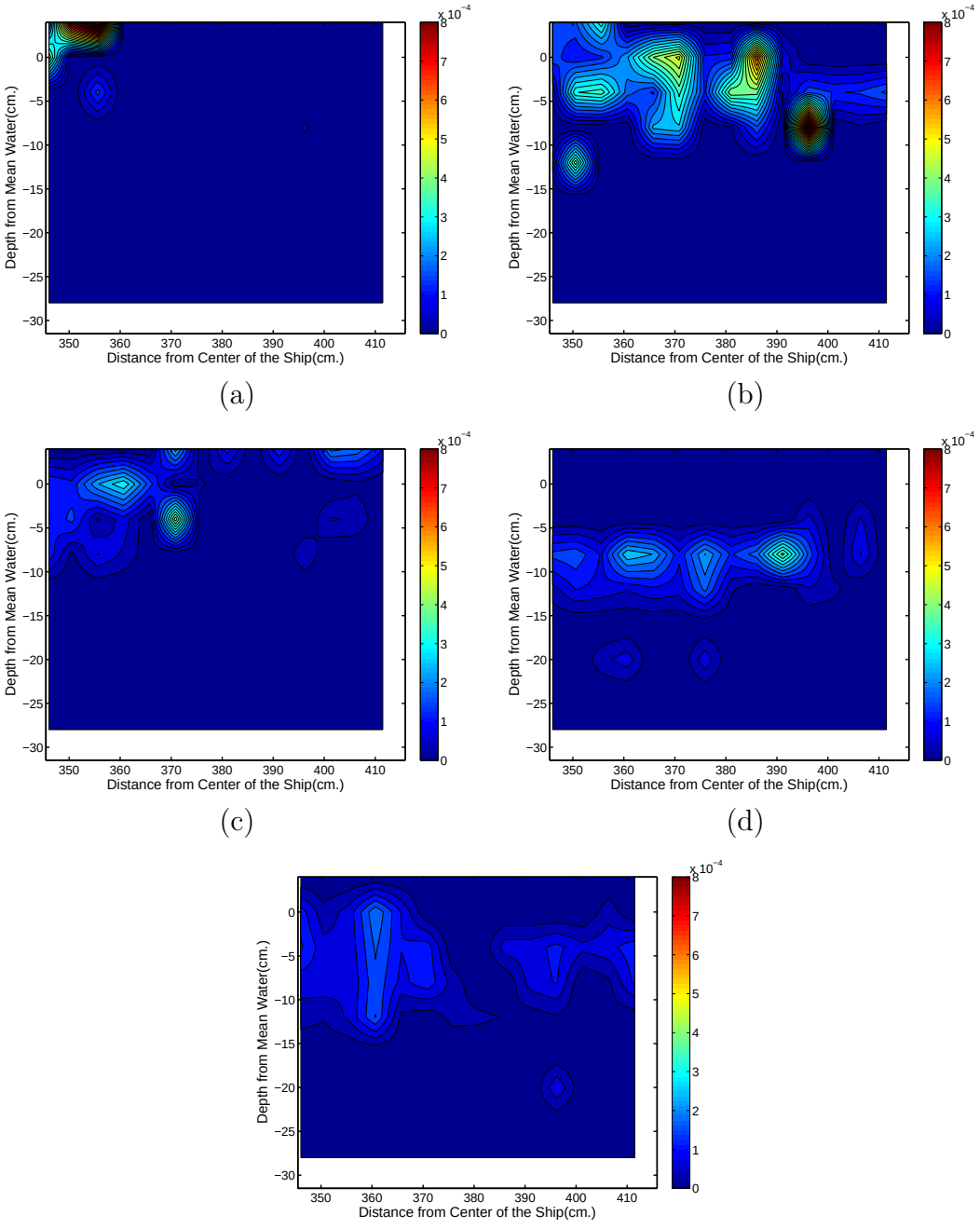

Figure 5.31: Void fraction contours in $y-z$ planes for $U_s = 22.5$ knots in the second bubble cloud for values of ((a) $x/L = 0.5$, (b) $x/L = 0.63$, (c) $x/L = 0.75$, (d) $x/L = 0.87$, (d) $x/L = 1.00$).

5.3.3 Mean Diameters Distribution

There are several methods to calculate the mean diameter of the bubbles,. Here we compute both the arithmetic mean diameter (called the mean diameter below) and the Sauter mean diameter. The mean diameter was calculated from the bubble diameter measurements by summing the diameter of each bubble in a give sample and dividing by the number of bubbles. The Sauter mean diameter is called "volume-surface mean diameter", and is commonly abbreviated as " d32" or "SMD". It is defined as 6 times the diameter of a sphere that has the same $volume/surface$ area ratio as the bubble sample of interest. The SMD is computed by first computing the the surface diameter, ds, where

$$d_s = \sqrt{\frac{A_b}{\pi}} \tag{5.6}$$

and A_b is the sum of the surface areas of all the bubbles in sample, and d_v, where

$$d_v = (\frac{6V_b}{\pi})^{\frac{1}{3}} \tag{5.7}$$

and V_b is the sum of all the bubble volumes in the sample. The Suter mean diameter of the given bubble sample is then given by

$$SMD = d_{32} = \frac{(d_v)^3}{(d_s)^2} = \frac{6V_b}{A_b} \tag{5.8}$$

In the present experiment, the mean diameter is dominated by the small bubbles since the number of small bubbles is many times larger than the number of

large bubbles, see the bubble density distributions in Figures 5.14 to 5.13. On the other hand, the Sauter mean diameter is dominated by larger bubbles since it is computed from the bubble volumes and surface areas and these are dominated by the larger bubbles.

Figure 5.32 and 5.33 show the mean diameter and the Sauter mean diameter versus x/L for the first and second bubble clouds for U_s equal to 27.5 knots and 22.5 knots, respectively. As can be seen in the plots, the mean diameter and the Sauter mean diameter are a little larger in the first cloud. Further, the plots show that the mean diameter and Sauter mean diameter decrease with increasing x/L. For $U_s = 27.5$ knots, Figure 5.32, the mean diameter (subplot(a)) and the Sauter mean diameter (subplot (b)) decrease nearly linearly with increasing x/L. The mean diameter decreases by about 10% from $x/L = 0.5$ to 1.0 in both bubble clouds. However, over the same range of x/L, the Sauter mean diameter decreases by about 40%. The nearly constant mean diameter and the large decrease in the Sauter mean diameter are consistent with the number of larger bubbles decreasing and the number of smaller bubbles being relatively unchanged with increasing x/L as was seen in the bubble distributions in Figures 5.14 and 5.15. For $U_s = 22.5$ knots, Figure 5.33, the mean diameter decreases nearly linearly with increasing x/L, but the Sauter mean diameter at first decreases rapidly until $x/L = 0.75$ and then more slowly. Similar behavior was seen the plot of average void fraction versus x/L in Figure 5.27(b) which is also for $U_s = 22.5$ knots.

Vertical distributions of the mean diameter and Sauter mean diameter for $U_s = 27.5$ and 22.5 knots at various values of x/L between 0.5 and 1.0 are shown

in Figures 5.34 and 5.35, respectively. At $U_s = 27.5$ knots, the shapes of the distributions for the mean diameter and the Sauter mean diameter are similar. For the first could the dimeters are relatively constant with depth until about $z = 24\ cm$ while for the second cloud, there is a maximum at $z \approx\ 4\ cm$ to 10 cm below the undisturbed water level. This means that the average diameter of the small bubbles is nearly constant with depth inside the bubble cloud while the average diameter of the larger bubbles increase, i.e., there are more larger bubbles, as the surface is approached from below. Similar curve shapes were found in the corresponding plots of void fraction versus depth, see Figures 5.26(a) and (b).

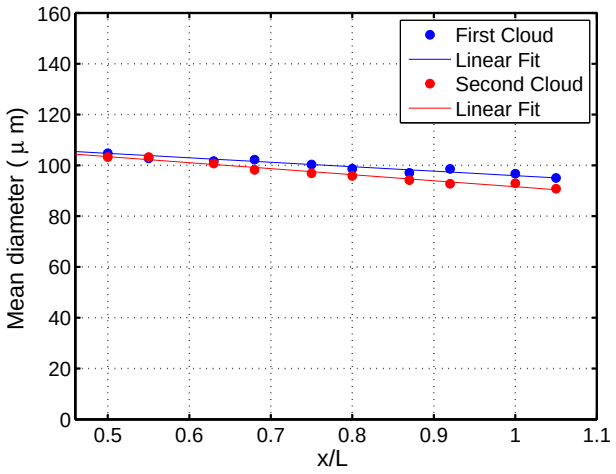

(a)

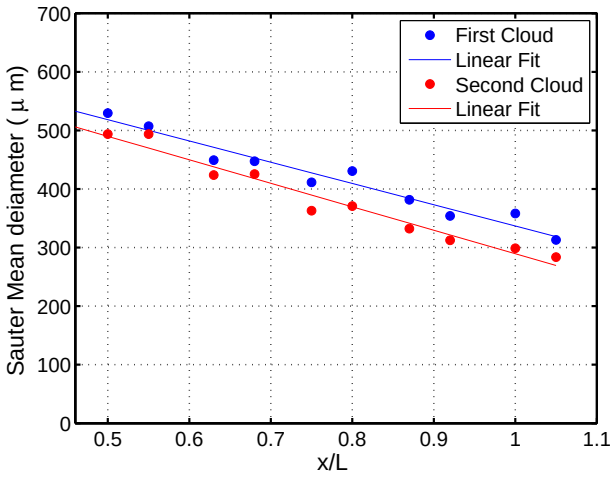

(b)

Figure 5.32: (a) Mean diameter and (b) Sauter mean diameter versus x/L for $U_s =$ 27.5 knots for the first and second bubble clouds.

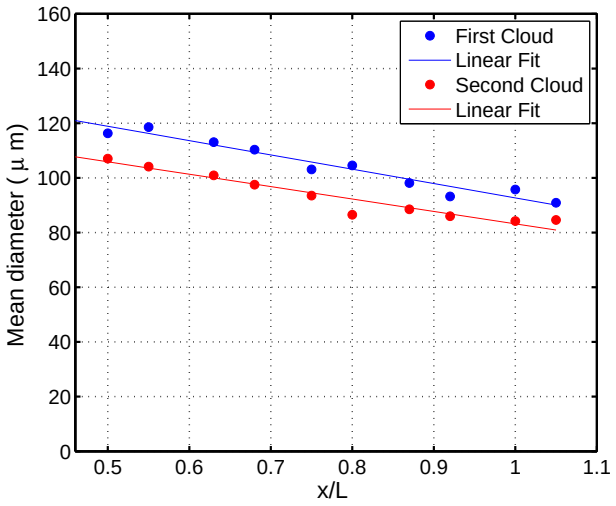

(a)

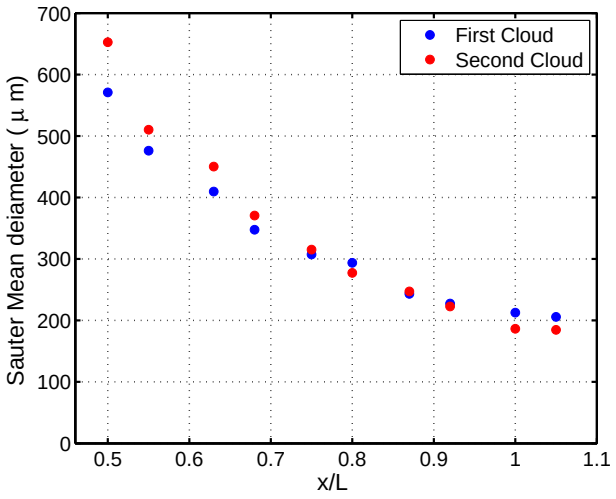

(b)

Figure 5.33: (a) Mean diameter and (b) Sauter mean diameter versus x/L for $U_s =$ 22.5 knots for the first and second bubble clouds.

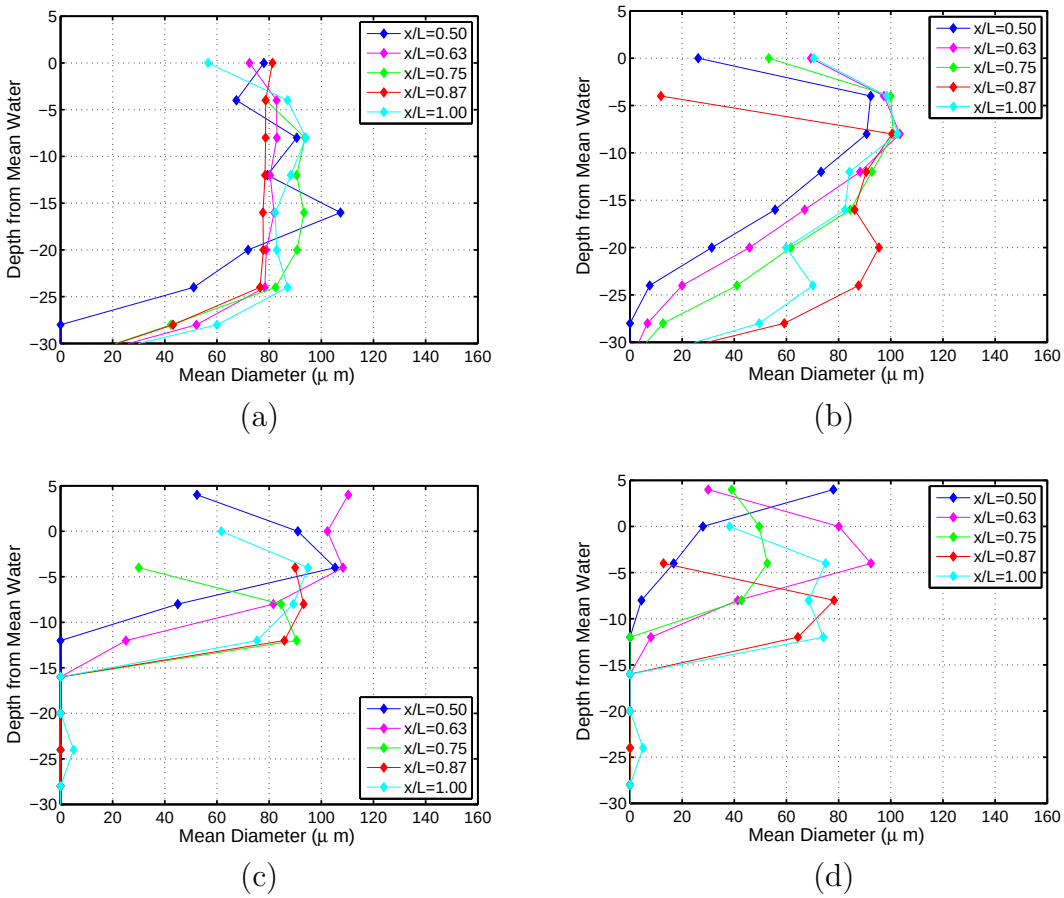

Figure 5.34: Mean Diameter vs. depth below the water surface at five times corresponding to five positions along the ship hull (a) 27.5 knots, first cloud, (b) 27.5 knots, second cloud, (c) 22.5 knots, first cloud, (d) 22.5 knots, second cloud.

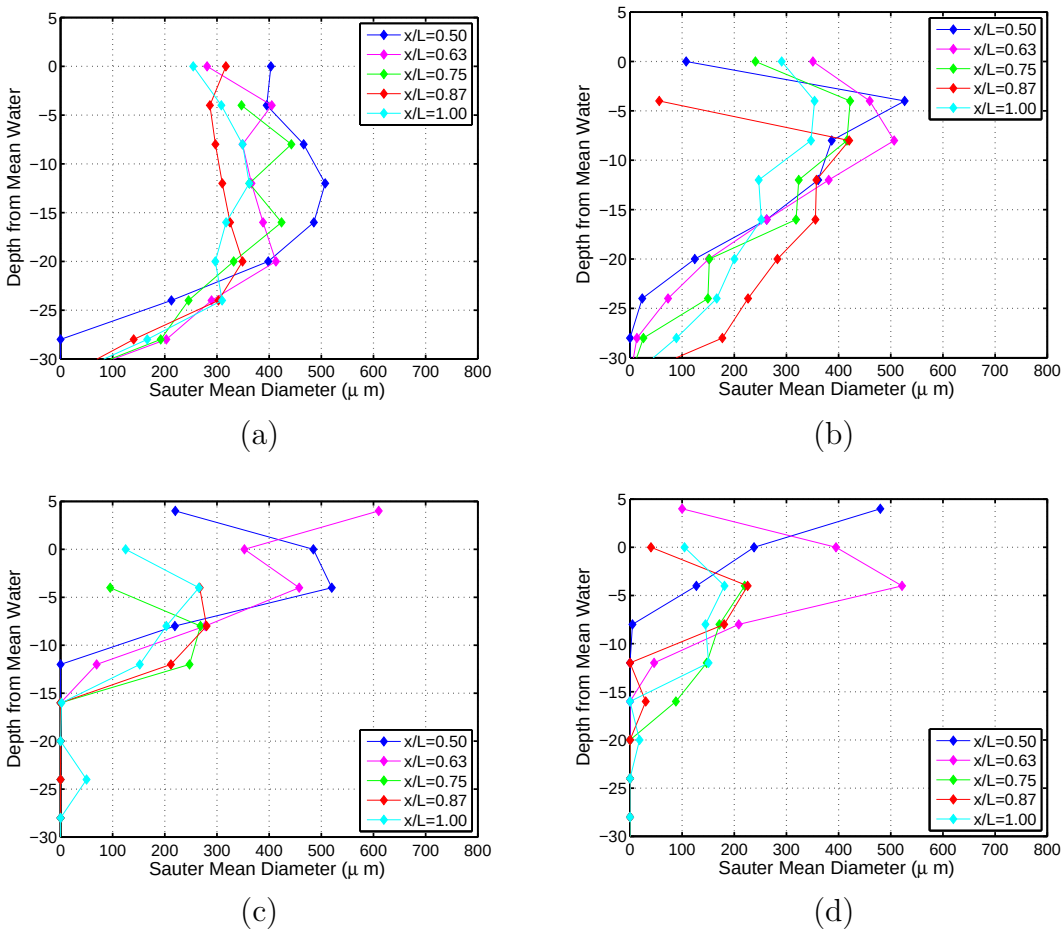

Figure 5.35: Sauter Mean Diameter vs. depth below the water surface at five times corresponding to five positions along the ship hull (a) 27.5 knots, first cloud, (b) 27.5 knots, second cloud, (c) 22.5 knots, first cloud, (d) 22.5 knots, second cloud.

5.3.4 Velocity Distribution

To calculate the velocity distributions at each x/L, the horizontal and vertical velocities of the bubbles in each diameter bin are summed and divide by the number of bubbles in that bin. Figures 5.36 and 5.37 show the horizontal and vertical velocity distributions with bubble diameter at different locations along the ship hull. Subplots (a) and (b) show the distributions for $U_s = 27.5$ knots for the first

and second clouds, respectively, while subplots (c) and (d) show the corresponding data for $U_s = 22.5$ knots. As can be seen in the plots, for all cases the horizontal and vertical velocities are relatively constant for the smaller bubble diameters; however, they start to fluctuate at the larger bubble diameters. This fluctuation is caused by the fact there are only a small number of the larger bubbles in each bin. The logarithmic bin-width distribution was used because it has a large bin width at large bubble diameters were the void fraction distribution is large and the measurement sample only includes a few bubbles. Since there are so many smaller bubbles than larger bubbles, see Figure 5.10 and 5.11, the average velocity of each bubble cloud is roughly equal to the average velocity of the smallest bubbles.

Figure 5.38 and 5.39 show the average horizontal and vertical velocity (subplots (a) and (b), respectively) versus x/L for the 27.5-knot and 22.5-knot cases, respectively, in both the first and second bubble clouds. The general trend is for the horizontal velocity to decrease with increasing x/L for all cases, while the vertical velocity generally increases with increasing x/L. For the 27.5-knot case, Figure 5.38, the horizontal velocity decreases significantly and then becomes constant after $x/L = 0.75$ for both clouds. By subtracting the horizontal velocity of the second cloud from that of the first cloud, the relative velocity of the two clouds was calculated and ploted in Figure 5.38 (a), for the 27.5-knot case. As can be seen in the figure, the relative velocity is nearly zero initially, increases until about $x/L = 0.75$ and then becomes constant. This positive relative velocity distribution means that the two bubble clouds are moving apart with a speed that increases initially but then settles down to a nearly constant value.

It is well known that the smaller bubbles tend to follow the water flow while larger bubbles, due to large buoyancy forces, large added mass, and other effects, do not. This can be seen in the bubble velocity distributions of Figures 5.36 and 5.37 where bubbles with diameters below about 150 μm all move with the same velocity, which must be the velocity of the water flow. The largest bubbles that will move with the water can be estimated by determining the largest bubbles that can follow the smallest scales of the turbulent flow. When the flow is turbulent, the smallest scales are described by the Kolmogoroff length and time scales. The Kolmogoroff time scale can be expressed as:

$$t_s = (\frac{\nu}{\varepsilon})^{\frac{1}{2}} \tag{5.9}$$

where ν is the kinematic viscosity (0.013 cm^2/s) and ε is the rate of dissipation of turbulence kinetic energy per unit mass of fluid. Reliable measurements of ε in the present flow are exceedingly difficult and were not attempted here. A rough estimate of ε can be calculated in the following manner. As a measure of the total mechanical energy of the wave, the estimate of Longuet-Higgis (1975) for the maximum energy of a single wavelength of a two-dimensional uniform wave train is used:

$$E = 0.8088\pi\rho g\lambda a^2 \tag{5.10}$$

where ρ is the density of the water and λ and a are the length and amplitude of the wave, respectively. In the 27.5-knot case, $\lambda \approx 2\ m$ and $a \approx 0.36\ m$ (Shakeri et al. 2009). In this case, if it is estimated that 40% of the total energy of the wave

is dissipated in a breaking event (Lamarre and Melville (1991)) over a time of one period ($T = 1.13\ sec$, which is calculated base on linear wave theory) and that the turbulent region has a size of 50 cm by 32 cm for the first cloud and 90 cm by 32 cm for the second cloud (measured dimensions of the bubble clouds from white light images, see Figure 4.11), then the estimated dissipation rate is:

$$\varepsilon = \frac{E \times 40\%}{(90 \times 32 + 50 \times 32) \times 1.13} = 5.041 \times 10^3 \frac{cm^4}{s^3} \tag{5.11}$$

The estimated Kolmogoroff time scale t corresponding to this dissipation rate is then $t_s = 1.59$ ms which is equal to a frequency of $f = 622$ Hz.

To determine the ability of the bubbles to follow the fluid motion, the work of Kiger (1995) was used. Base on this work, the motion of particles in a turbulent flow was studied theoretically. It was found that the bubbles would closely follow the fluid if the Stokes number,

$$St = \frac{d^2 f}{18\nu\gamma} \tag{5.12}$$

(where ν is kinematic viscosity of the fluid, γ is the ratio of the fluid density to bubble density and f is the frequency of the velocity fluctuations), is smaller than 10^{-4} . For the present case, with $f = 622$ Hz and $\gamma = 1000$ and $\nu = 0.013$ cm^2/s, it was found that bubbles with diameters smaller than about 69 μm should follow the turbulent flow quite well. This estimate is roughly a factor two of below the values of the limiting bubble diameter (150 μm) as determined from the bubble velocity distributions in Figures 5.36 and 5.37. This rough level of agreement is

to be expected based on the rough approximation of the energy dissipation in the theory.

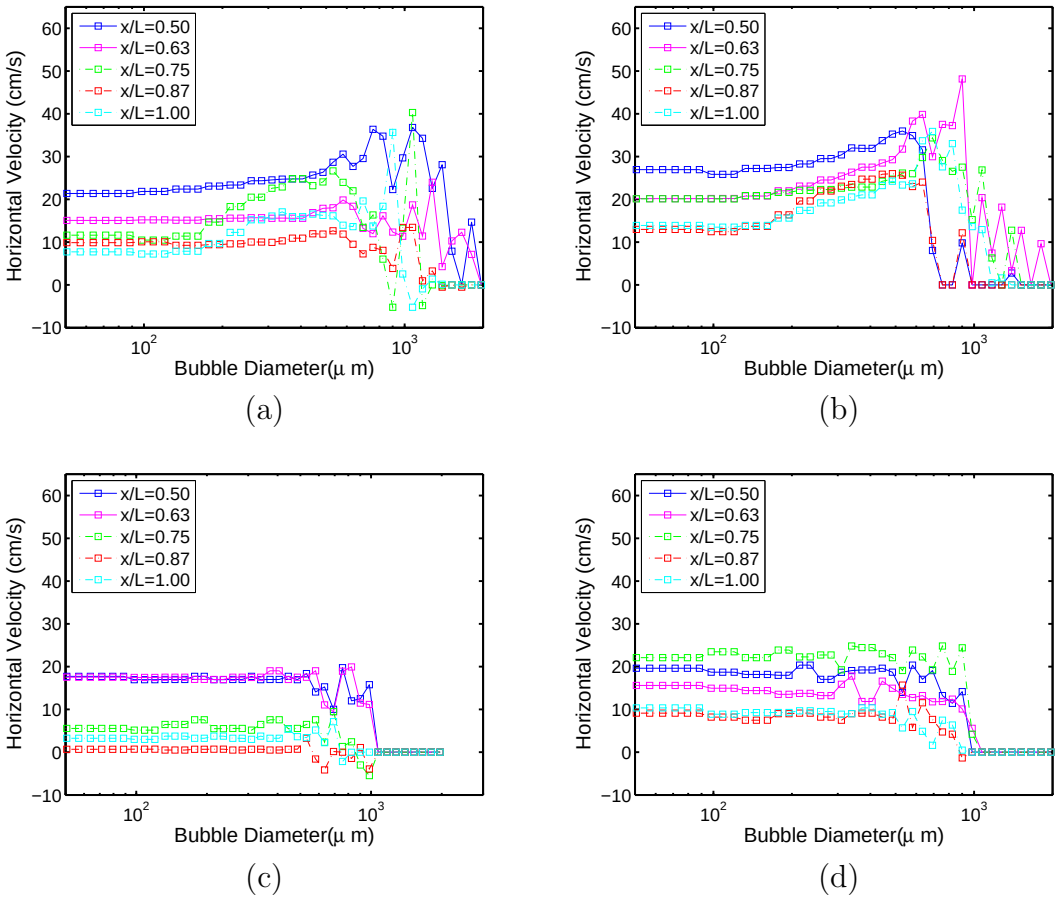

Figure 5.36: Horizontal velocity components versus bubble diameter at five times corresponding to five positions along the ship hull. (a) 27.5 knots, first cloud, (b) 27.5 knots, second cloud, (c) 22.5 knots, first cloud, (d) 22.5 knots, second cloud.

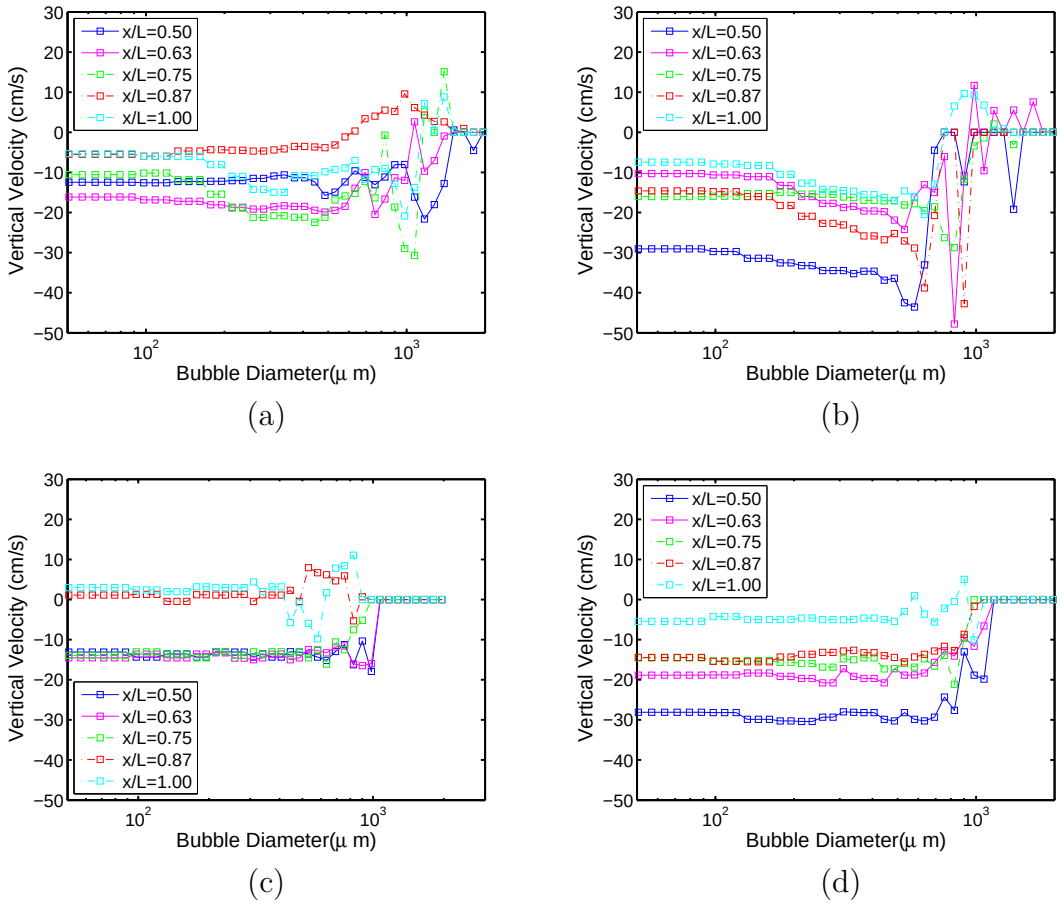

Figure 5.37: Vertical velocity components versus bubble diameter at five times corresponding to five positions along the ship hull. (a) 27.5 knots, first cloud, (b) 27.5 knots, second cloud, (c) 22.5 knots, first cloud, (d) 22.5 knots, second cloud.

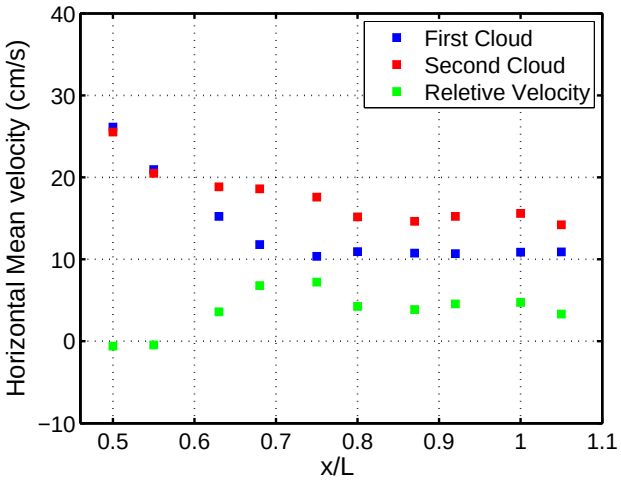

(a)

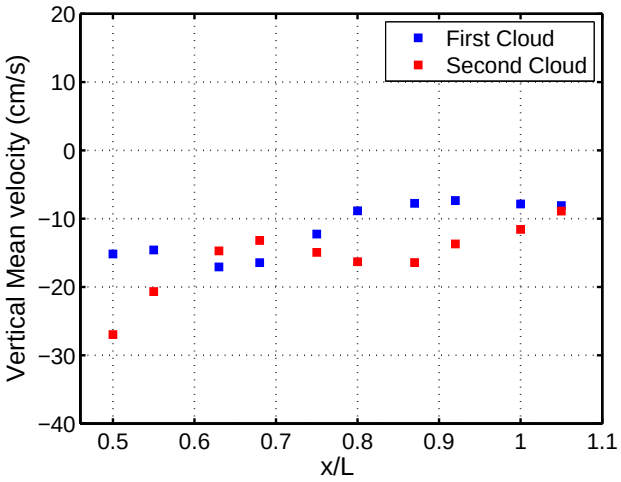

(b)

Figure 5.38: : Mean Velocities versus position along the ship hull at first and second cloud for 27.5 knot equivalent ship speed (a) Horizontal mean velocity (b) Vertical mean velocity.

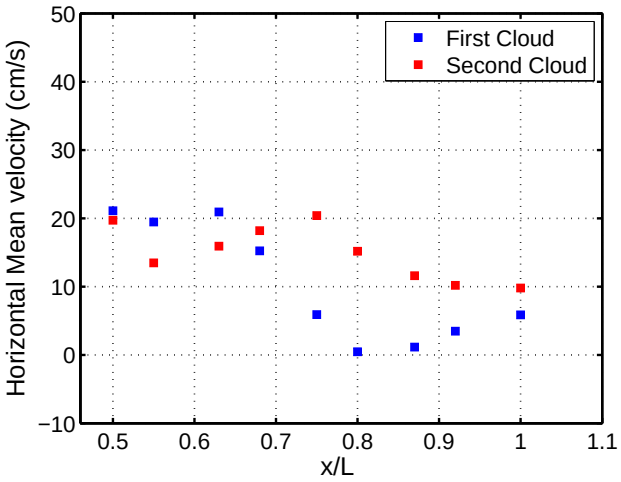

(a)

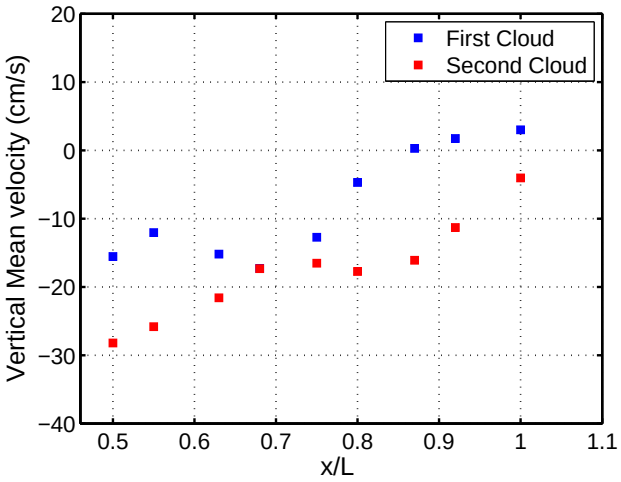

(b)

Figure 5.39: : Mean Velocities versus position along the ship hull at first and second cloud for 22.5 knot equivalent ship speed (a) Horizontal mean velocity (b) Vertical mean velocity.

Figure 5.40 and 5.41 show the average horizontal velocity and vertical velocity, respectively, versus x/L for different ranges of bubble diameters. In each figure, subplots (a) and (b) are for the first and second bubble clouds, respectively, for $U_s = 27.5$ knots and subplots (c) and (d) are for the first and second bubble clouds,

respectively, for $U_s = 22.5$ knots. As was discussed above, the bubbles smaller than 150 μm in diameter have the same velocity and it can be assumed that this is the velocity of the water. For $U_s = 27.5$ knots (subplots (a) and (b) in both figures), data is presented with velocities averaged separately over bubbles with various ranges of bubble diameters (all the bubbles, $d \leq 150$ μm, 300 μm $\leq d \leq 700$ μm, $d \geq 700$ μm and $d \geq 1000$ μm). For $U_s = 22.5$ knots (subplots (c) and (d) in both figures), data is presented with velocities averaged separately over bubbles with various ranges of bubble diameters (all the bubbles, $d \leq 150$ μm, and $d \geq 500$ μm).

As can be seen in the figures, since there are so many more bubbles with diameters less than 150 μm, the average velocity of all the bubbles is nearly equal to the velocity averaged over of all the bubbles with diameters less than 150 μm. The velocities of the various ranges of bubble diameters greater than 150 μm differ from the water velocity by as much as 30 cm/s in the vertical velocity component and 14 cm/s in the horizontal velocity component for the 27.5-knot case. In the 22.5-knot case, the velocities of the all bubbles with diameters larger than 500 μm also differ from the water velocity by as much as 10 cm/s in the vertical velocity component and 5 cm/s in the horizontal velocity component. These differences are greatest for the largest bubbles and increase with increasing x/L for both ship speeds. In all cases, the horizontal velocity of the larger bubbles are less than the water velocity, while the vertical velocity of the larger bubbles are greater than the water velocity. In contrast, the bubbles with diameter 300 μm $\leq d \leq 700$ μm in the 27.5-knot case generally have a horizontal velocity component that is bigger than the water velocity and a vertical velocity component that is smaller than the water

velocity. Thus, it seems that there is a transition region between the velocities of bubbles with small diameter ($d \leq 300$ μm) and the velocities of bubbles with larger diameter ($d \geq 700$ μm).

The slip velocity of the larger bubble relative to the water can be calculated by subtracting the velocity of the bubbles smaller than 150 μm from the velocity of the larger bubbles. Figure 5.42 and 5.43 show the vertical slip velocity (rise velocity) for the large bubbles for the 27.5-knot and 22.5-knot ship speeds, respectively, for the first and second bubble clouds. As can be seen in the figures, the rise velocity in both cases increases with increasing x/L. In the 27.5-knot case, the rise velocity is calculated for the bubbles larger than 700 μm and the bubbles larger than 1000 μm and as expected the larger bubbles (1000 μm) have the larger rise velocity.

Figure 5.44 to Figure 5.47 show the velocity fields in planes of constant x/L for the first and second bubble clouds for the 27.5-knot case (Figure 5.44 and 5.45) and the 22.5-knot case (Figure 5.46 and Figure 5.47) for five different positions along the ship hull (x/L=0.5, 0.63, 0.75, 0.87, 1.0). It should noted that in spite of the very long measurement campaign in the present experiments, while there are many bubbles in the samples for the entire bubble clouds, the number of bubbles in a sample at a given y-z location at each x/L is much smaller. Thus, the average velocity vector at each location is a bit noisy. In spite of this deficiency, some patterns can be detected in the velocity vector plots. In all cases, the velocity vectors at x/L=0.5 and x/L=0.63 have roughly the same direction and magnitude in all locations. However, at x/L=1.00 the flow appears more random in all cases and the velocity vectors change in both direction and magnitude. This contrast may

indicate that the flow fields at the smaller values of x/L are dominated by the wave motion, while those at larger x/L show a stronger influence of the turbulent flow field.

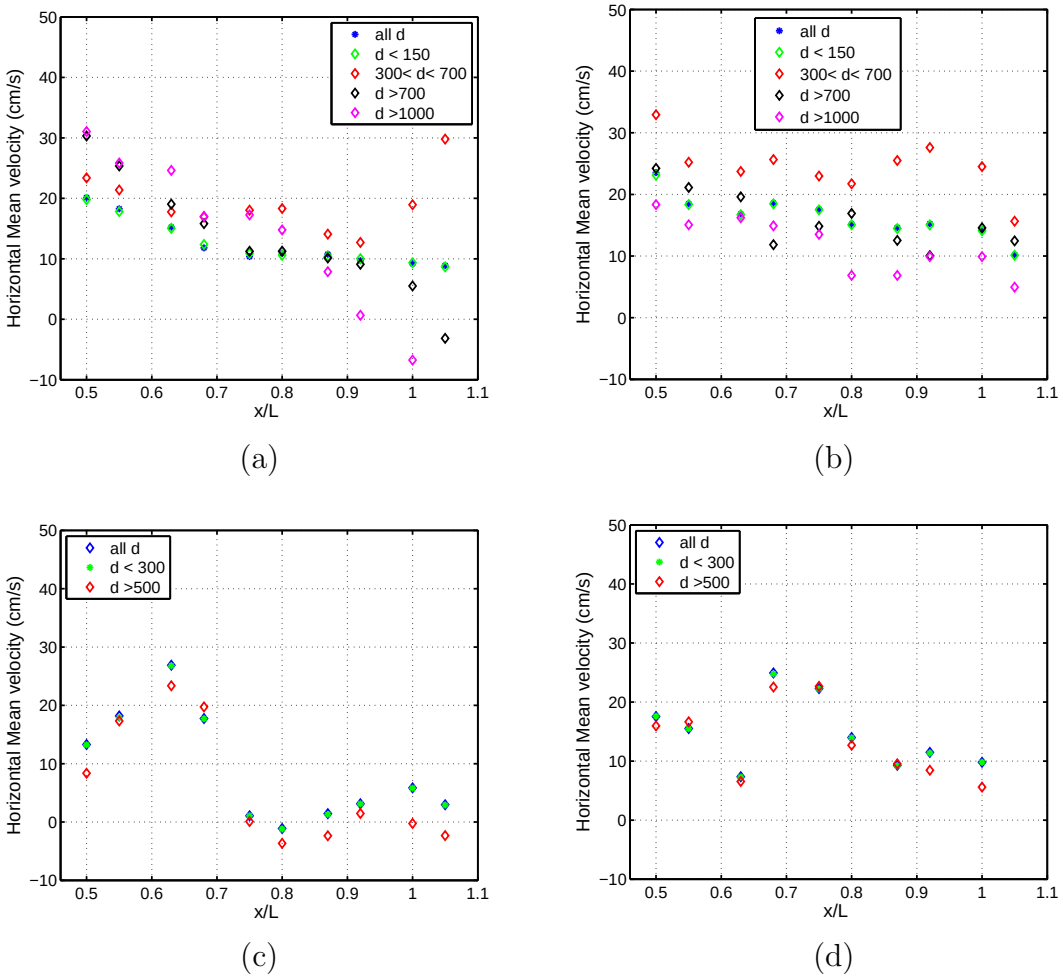

Figure 5.40: Horizontal velocity components versus x/L. (a) 27.5 knots, first cloud, (b) 27.5 knots, second cloud, (c) 22.5 knots, first cloud, (d) 22.5 knots, second cloud. Data is shown for averages over various ranges of bubble diameters.

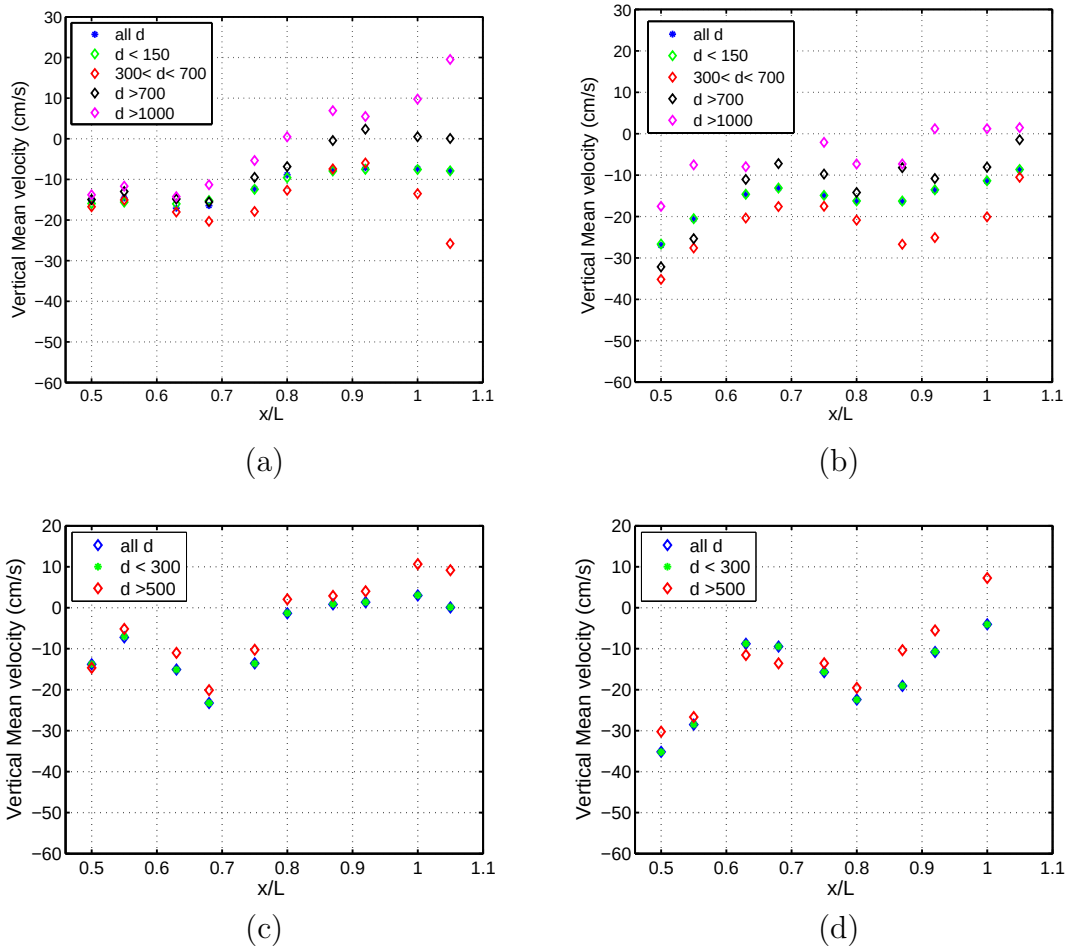

Figure 5.41: Vertical velocity components versus x/L. (a) 27.5 knots, first cloud, (b) 27.5 knots, second cloud, (c) 22.5 knots, first cloud, (d) 22.5 knots, second cloud. Data is shown for averages over various ranges of bubble diameters.

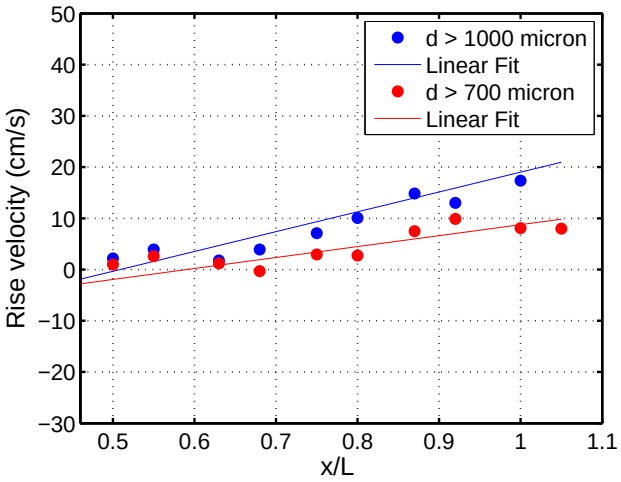

(a)

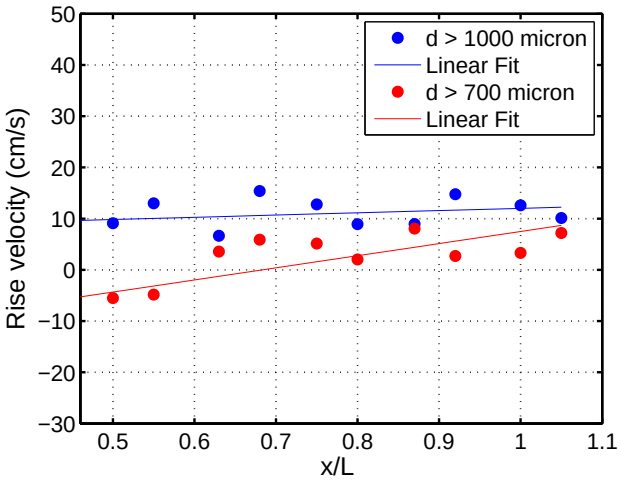

(b)

Figure 5.42: Rise Velocities (relative to the water) versus x/L for $U_s = 27.5$ knots for bubbles with diameters larger than 1000 μm and bubbles with diameters larger than 700 μm at (a) the first bubble cloud and (b) the second bubble cloud.

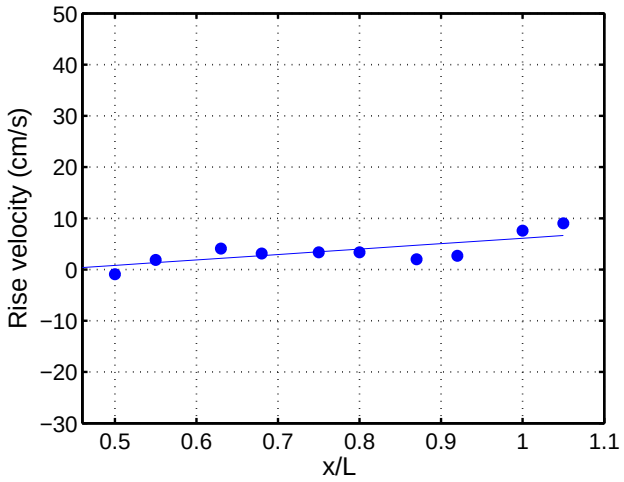

(a)

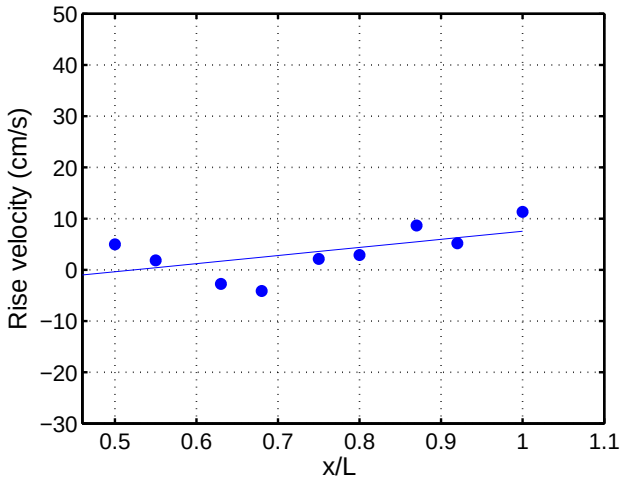

(b)

Figure 5.43: Rise Velocities (relative to the water) versus x/L for $U_s = 22.5$ knots for bubbles with diameters larger than 1000 μm and bubbles with diameters larger than 700 μm at (a) the first bubble cloud and (b) the second bubble cloud.

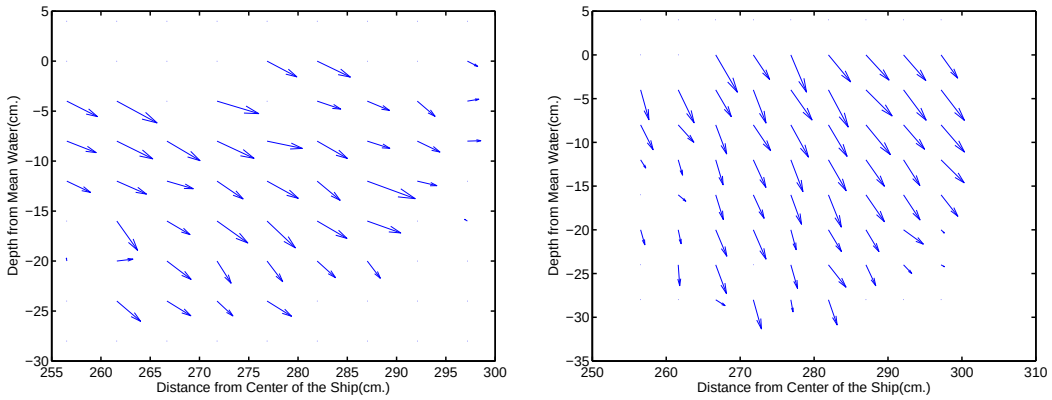

(a)

(b)

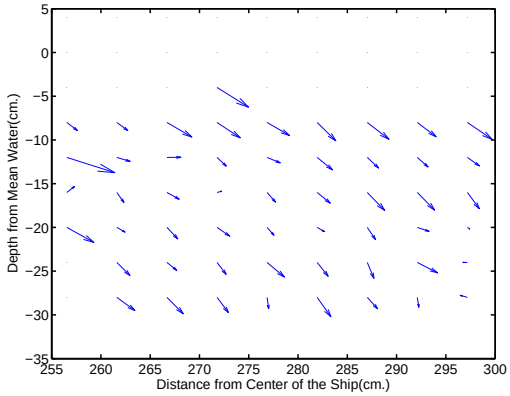

(c)

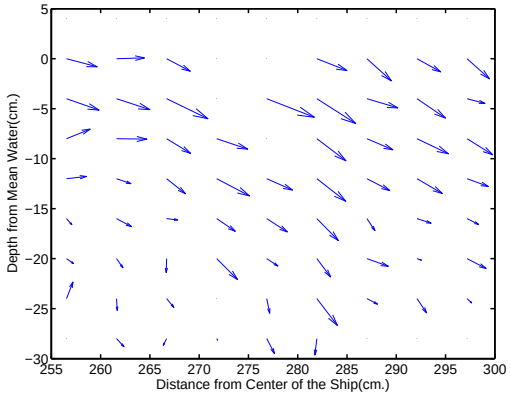

(d)

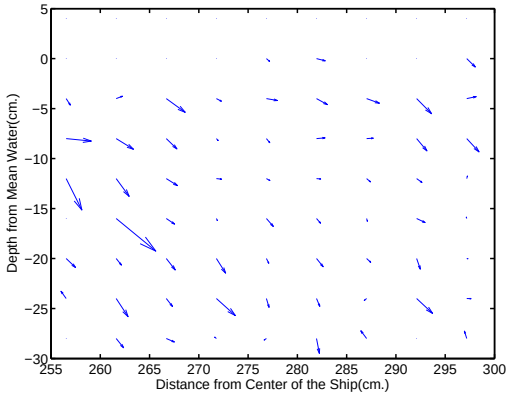

(e)

Figure 5.44: Velocity vectors in $y-z$ planes for $U_s = 27.5$ knots in the first bubble cloud: (a) $x/L = 0.5$, (b) $x/L = 0.63$, (c) $x/L = 0.75$, (d) $x/L = 0.87$, (d) $x/L = 1.00$.

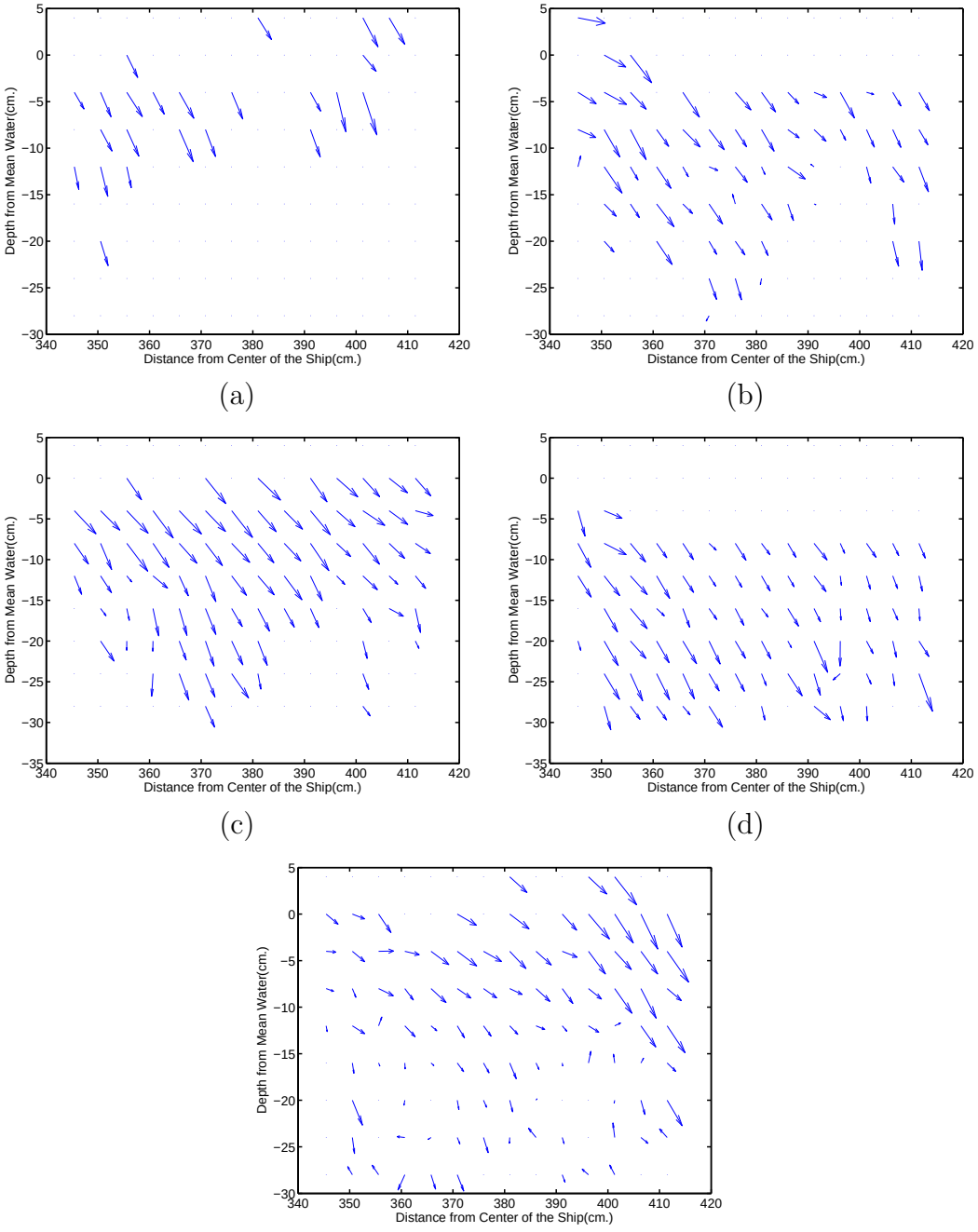

Figure 5.45: Velocity vectors in $y-z$ planes for $U_s = 27.5$ knots in the second bubble cloud: (a) $x/L = 0.5$, (b) $x/L = 0.63$, (c) $x/L = 0.75$, (d) $x/L = 0.87$, (d) $x/L = 1.00$.

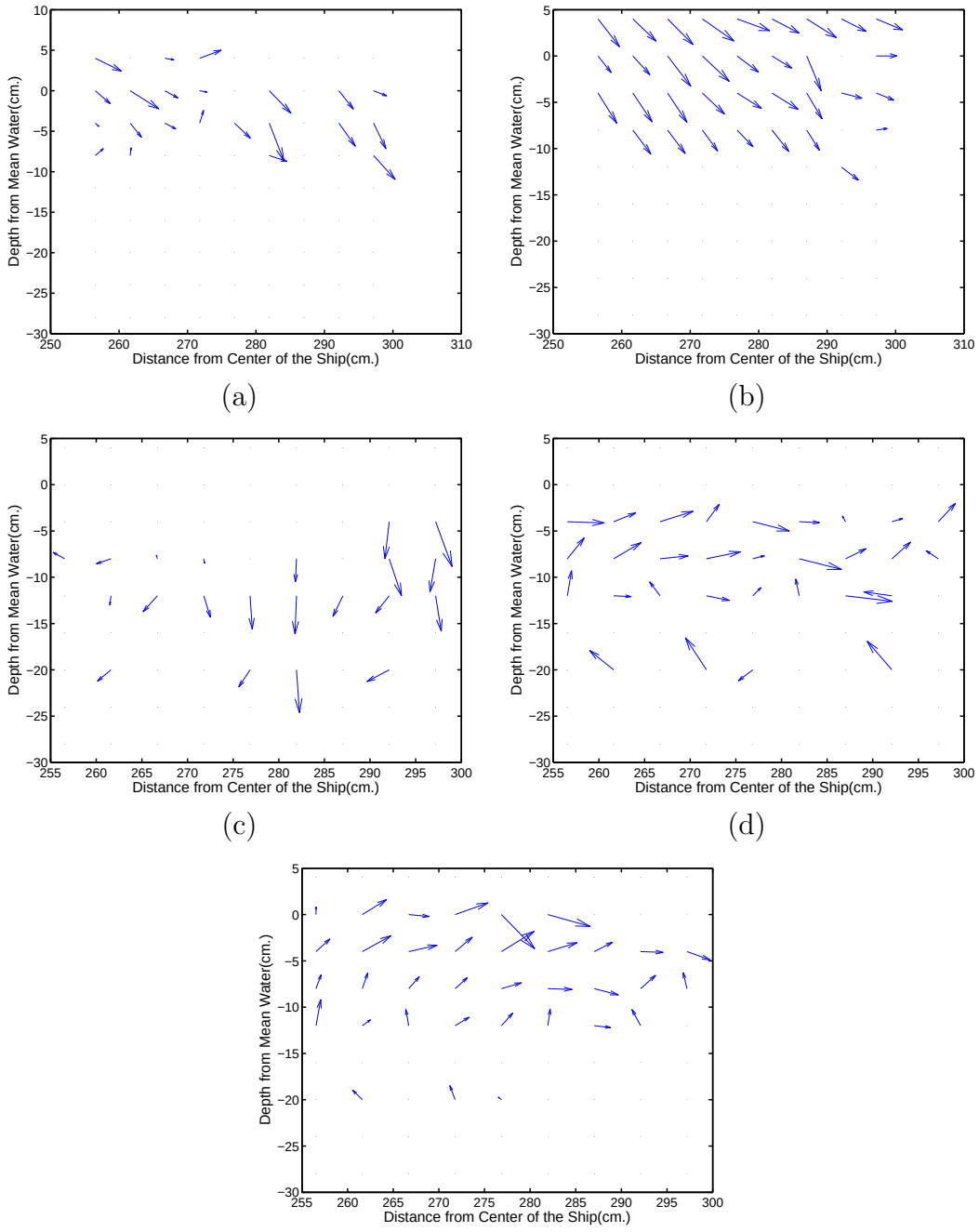

Figure 5.46: Velocity vectors in $y-z$ planes for $U_s = 22.5$ knots in the first bubble cloud: (a) $x/L = 0.5$, (b) $x/L = 0.63$, (c) $x/L = 0.75$, (d) $x/L = 0.87$, (d) $x/L = 1.00$.

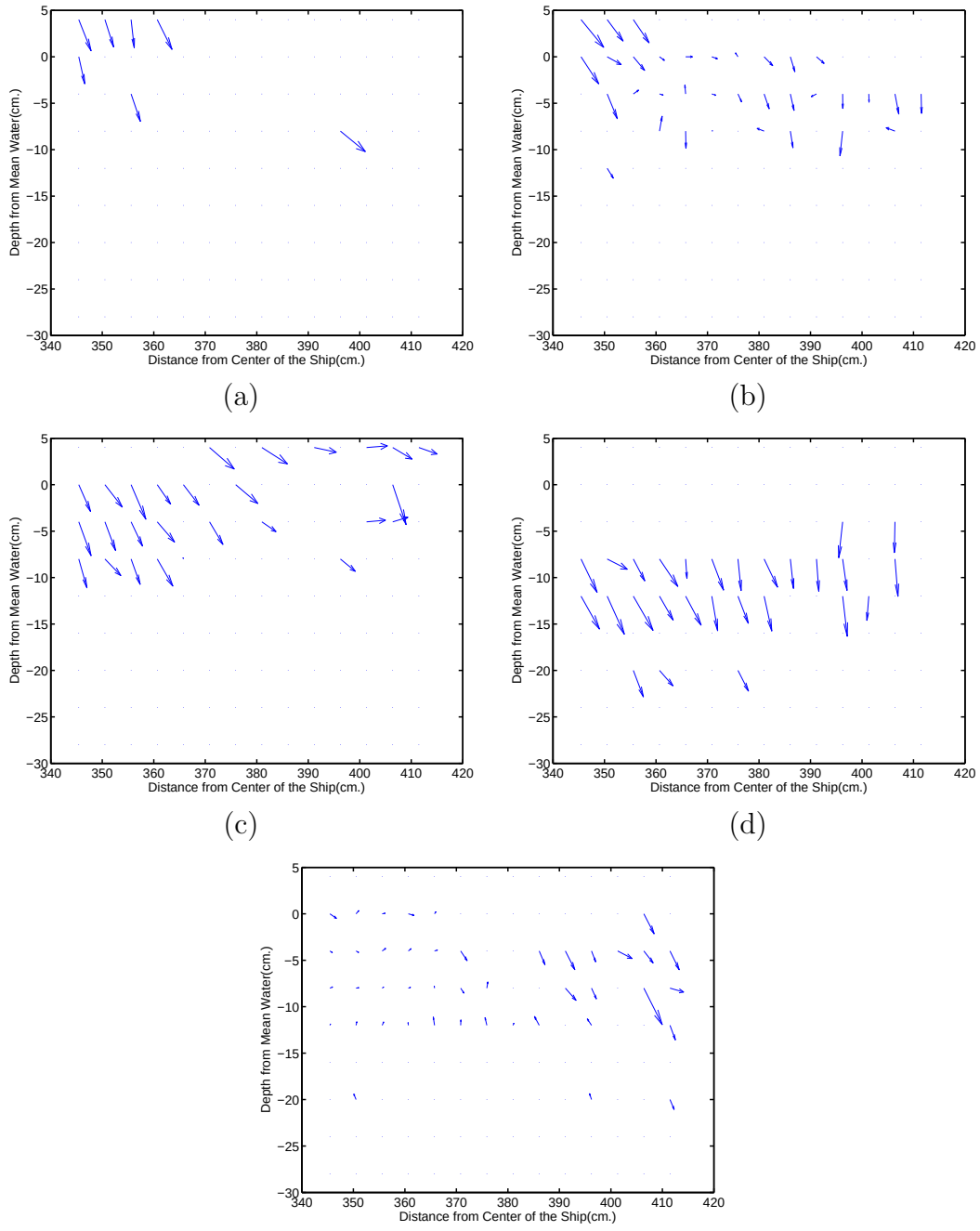

Figure 5.47: Velocity vectors in $y-z$ planes for $U_s = 22.5$ knots in the second bubble cloud: (a) $x/L = 0.5$, (b) $x/L = 0.63$, (c) $x/L = 0.75$, (d) $x/L = 0.87$, (d) $x/L = 1.00$.

Chapter 6

Conclusions

6.1 Summary

In this thesis, a technique known as 2D+T that is used in numerical analysis was adapted to the laboratory in order to produce waves that are large enough to correctly model the effects of surface tension and therefore produce realistic air entrainment. In the 2D+T technique, a two-dimensional wave maker moves horizontally and deforms in a manner that mimics the time varying profile of the intersection of one side of a three-dimensional ship model hull moving forward at constant speed, U, and a fixed imaginary vertical plane oriented perpendicular to the ship's path. The wave profile at each instant in time (t with $t = 0$ the time of passage of the ship model stem) corresponds to the wave profile in the three-dimensional ship model at a cross-stream plane located at $x = Ut$. The experiments were performed in artificial sea water, which is known to dramatically increase the number of small bubbles when compared to fresh water.

For the equivalent full-scale ship speeds, U_s, chosen in this study, the primary mechanisms responsible for air entrainment in the 2D+T experiments are the entrapment of a large air bubble under the wave crest at the instant when the plunging jet hits the front face of the wave and the turbulent flow and impact of the splash created by the plunging jet impact. Qualitative observations of the air entrainment

process were made using white-light back-lit high-speed movies and measurements of the diameters and velocities of the entrained bubbles were made using shadowgraph images captured by two PIV cameras viewing the flow through the clear plastic wall of the wave tank and using a parallel light beam from a PIV laser for illumination. An extensive series of measurements were made for two equivalent full-scale ship speeds, $U_s = 22.5$ and 27.5 knots. Detailed accomplishments and conclusions of this work are given below.

- For $U_s = 22.5$ knots, a weak plunging breaker with a small plunging jet was found. (If U_s is reduced to 20 knots, a strong spilling breaker is found.) The bubbles entrained by this breaking wave are distributed in a relatively uniform bubble distribution in a narrow band near the water surface reaching a depth of about $D/6$, where D is the keel depth of the 2D+T wave maker.

- For $U_s = 27.5$ knots, the highest ship speed available with the 2D+T wave maker, a very strong plunging breaker with a large plunging jet is found. The air entrainment process produces two clouds of bubbles near the free surface. The bubble cloud closest to the wave maker (called the first bubble cloud) is due to air entrapped under the wave crest by the impact of the plunging jet and the bubble cloud farthest from the wave maker (called the second bubble cloud) results from the turbulent motion and impact of the splash. Bubbles are entrained to depths approximately equal to about $D/3$.

- For $U_s = 27.5$ knots, the bubble cloud from the splash moves away from the wave maker at a higher speed than the bubble cloud created under the crest by

the impact of the plunging jet; therefore, the separation between the bubble clouds increases as time goes on.

- Bubble density distributions (number of bubbles, n, per unit volume per unit bin width versus bubble diameter, d) in log-log coordinates form approximately straight lines. For $U_s = 27.5$ knots, the data show two distinct regions ($d < d_H$ and $d > d_H$) where the data roughly follows separate straight lines, $n = n_0(d/d_H)^\alpha$ for $d < d_h$ and $n = n_0(d/d_H)^\beta$ for $d > d_H$. For $U_s = 22.5$ knots, there are only a small number of large bubbles and the data approximately fit a single straight line $n = n_0(d/d_H)^\alpha$.

  - Conclusions for $U_s = 27.5$ knots:

    * The value of d_H was found to be about 800 μm for both the first and second bubbble clouds.

    * At a bubble diameter $d = d_H$, the number of bubbles per unit volume in the second bubble cloud is about 30% greater than that in the first bubble cloud.

    * The values of α are nearly the same in the two bubble clouds. The values of β are nearly same as well.

    * The exponent α is nearly independent of x/L in both clouds, indicating that though these small bubbles may move about due to the fluid motion, the effect of buoyancy is insufficient to cause them to leave the flow through the free surface.

    * There is a large rate of decrease of the exponent β with x/L in

both clouds indicating a significant reduction in the number of larger bubbles, probably due to the influence of degassing caused by their large buoyancy.

  - Conclusions for $U_s = 22.5$ knots:

    * The power law exponent α for both measurement regions (termed the first and second bubble clouds even though they are part of a single layer of bubbles) are practically constant and nearly equal to one another.

- Void fraction distributions.

  - For $U_s = 27.5$ knots, the average void fraction of the second bubble cloud is about 20% greater than that of the first bubble cloud.

  - For $U_s = 27.5$ knots, the void fraction is relatively constant with depth to about 20 cm below the mean water level for the first bubble cloud, but shows a strong peak at 4 to 10 cm below the undisturbed water level for the second cloud. This is probably due to the very different entrainment mechanisms in the two bubble clouds: entrapment by the jet impact for the first bubble cloud and more diffuse entrainment in the splash for the second bubble cloud. The void fraction magnitudes and the depths of the void fraction peak generally decrease with increasing x/L.

  - For $U_s = 22.5$ knots, the layer of appreciable void fraction extends to a depth of about 10 to 15 cm with a peak generally at about 4 cm. The void

fraction magnitudes and the depths of the void fraction peak generally decrease with increasing x/L.

  - The data indicates a nearly 50% reduction in void fraction over the last half of the ship. From the bubble density distributions for both speeds, this void fraction reduction is due primarily to a reduction in the number of large bubbles.

- Bubble diameters.

  - The mean diameter and the Sauter mean diameter decrease nearly linearly with increasing x/L for both speeds. The mean diameter decreases by about 10% from midship to stern in both bubble clouds. However, over the same range of x/L, the Sauter mean diameter decreases by about 40%. The nearly constant mean diameter and the large decrease in the Sauter mean diameter are consistent with the number of larger bubbles decreasing and the number of smaller bubbles being relatively unchanged with increasing x/L.

  - The ratio of the Sauter mean diameter to the mean diameter is about 5 at $x/L = 0.5$ but decreases to about 3 at $x/L = 1.0$.

- Bubble velocity:

  - For both ship speeds, the bubble velocity distributions indicate that for bubbles with diameters below about 150 μm move with the same velocity, which must be the velocity of the water flow.

- The rise velocity for the larger bubbles (larger than 500 μm for U_s = 22.5 knots and larger than 700 μm for U_s = 27.5 knots) relative to the water (i.e., the vertical component of the bubble slip velocity) increases with x/L.
- For U_s = 27.5 knots, the rise velocity for bubbles with diameters larger than 1000 μm is bigger than that of the bubbles larger than 700 μm and increases with x/L.

6.2 Future Work

As mentioned before, this thesis is part of a larger project. A few ideas for future work are listed as below:

- A detailed investigation of air entrainment by scaling with geometric hull shape parameters for ships with flat side walls at various angles of inclination to the undisturbed water surface using the current wave maker.
- Flow field measurements in the breaking waves using particle image velocimetry.
- Employment of a bore scope system to see inside the cavity under the plunging jet in order to obtain information about the jet thickness and the air entrainment process.
- Employment of the holographic PIV system for bubble size and motion measurements.

- Development of an impedance-based probe for bubble measurements in the early stages of breaking when large bubbles exist in the flow.

Bibliography

[1] Baba, E., 1969, An new component of viscous resistance of ships,*Journal of the Naval Architecture of Japan* ,**125** : 9-34.

[2] Banner, M. L., D. H. Peregrine, 1993, Wave breaking in deep water,*Annual Review of Fluid Mechanics*, **25**: 373-397.

[3] Battjes, J. A. and T. Sakai, 1981, Velocity field in a steady breaker,*Journal of Fluid Mechanics*, **111**: 421-437.

[4] Blanchard, D.C, A.H. Woodcock, 1957, Bubble formation and modification in the sea and its meteorological significance. *Tellu*, **9(2)**: 145-158.

[5] Blenkinsopp, C. E. and J. R. Chaplin, 2007, Validity of small-scale physical models involving breaking waves. In Proc. 22nd Int. Workshop on Water Waves and Floating Bodies, Plitvice, Croatia.

[6] Blenkinsopp, C. E. 2007, Air entrainment, splash and energy dissipation in breaking waves. PhD thesis, School of Civil Engineering and Environment, University of Southampon.

[7] Bonmarin, P. 1989, Geometric properties of deep-water breaking waves. *Journal of Fluid Mechanics*,**209**: 405433.

[8] Carrica, P.M. et al. 1998, A polydisperse approach to the two phase flow around a ship. Lyon, France, Third International Conference on Multiphase Flow.

[9] Cartellier, A. and J. L. Achard, 1991, Local phase detection probes in fluid/fluid two-phase flows. *Rev. Sci. Inst.*, **62**: 279303.

[10] Cartmill, J. W. and M.Y. Su, 1993, Bubble size distribution under saltwater and freshwater breaking waves.*Dyn. Atmos. Oceans*,**20**: 2531.

[11] Chabot, J., S. L. P. Lee, A. Soria, and H. I. de Lasa, 1992, Interaction between bubbles and fiber optic probes in a bubble column. *Can. J. Chem. Eng.*, **70**): 6168.

[12] Chanson, H., S. Aoki, and A. Hoque, 2006, Bubble entrainment and dispersion in plunging jet flows: freshwater vs. seawater.*J. Coast. Res.*, **22**: 664677.

[13] Cointe, R. and M. P. Tulin, 1994, A theory of steady breakers,*Journal of Fluid Mechanics*, **276**: 1-20.

[14] Commander, K. W. and A. Prosperetti, 1989, Linear pressure wave in bubbly liquids: Comparision between theory and experiments. *J. Acoust. Soc. Am.*, **85**: 732-746.

[15] Couriel, E. D., Horton, P. R. and D. R. Cox, 1998, Supplementary 2-D physical modelling of breaking wave characteristics. Technical Report 98114, Water Research Laboratory, Sydney, Australia:University of New South Wales.

[16] Cox, D. T. and S. Shin, 2003, Laboratory measurements of void fraction and turbulence in the boreregion of surf zone waves.*J. Eng. Mech.*, **129**: 11971205.

[17] Dabiri, D. and M. Gharib, 1997, Experimental investigation of the vorticity generation within a spilling water wave, *Journal of Fluid Mechanics*, **330**: 113-139.

[18] Deane, G. B. 1997, Sound generation and air entrainment by breaking waves in the surf zone. *J. Acoust. Soc. Am.*, **102**: 26712689.

[19] Deane, G. B. and M. D. Stokes, 2002, Scale dependence of bubble creation mechanisms in breaking waves.*Nature*, **418**: 839844.

[20] Delhommeau, G., F. Noblesse, H. Y. Kim and C. Yang, 2009, Bow waves of a family of fine ruled ship hulls with rake and flare, *Journal of Ship Research*, in review.

[21] Dong, R. R., J. Katz, and T. T. Huang, 1997, On the structure of bow waves on a ship model, *Journal of Fluid Mechanics*, **346**: 77-115.

[22] Duncan, J. H., 1981, An experimental investigation of breaking waves produced by a towed hydrofoil,*Proceedings of the Royal Society of London*, Series A, **377**: 331-348.

[23] Duncan, J. H., 1983, The breaking and nonbreaking resistance of a twodimensional hydrofoil, *Journal of Fluid Mechanics*, **126**: 507-520.

[24] Duncan, J. H., H. Qiao, H. Behres, and J. Kimmel, 1994, The formationof spilling breaker,*Physics of Fluids*, **6(8)**: 2558-2560.

[25] Duncan, J. H., H. Qiao, V. Philomin, and A. Wenz, 1999, Gentle spilling breakers: crest profile evolution,*Journal of Fluid Mechanics*, **379**: 191-222.

[26] Duncan, J. H., 2001, Spilling reakers,*Annu. Rev. Fluid Mech.*, **33**: 519-547.

[27] Farmer, D. M., C. L. McNeil, and B. D. Johnson, 1993, Evidence for the importance of bubbles in increasing air-sea gas flux. *Nature*, **361**: 620-623.

[28] Farmer, D. M., S. Vagle and A. D. Booth, 1998, A free-flooding acoustical resonator for measurement of bubble size distributions. *J. Atmos. Oceangr. Tech.*, **15**: 11321146.

[29] Haines, M. A., and B. D. Johnson, 1995, Injected bubble populations in seawater and fresh water measured by a photographic method. *J. Geophysical Research*, **100**: 70577068.

[30] Hong, M., A. Cartellier and E. J. Hopfinger, 2004, Characterisation of phase detection optical probes for the measurement of the dispersed phase parameters in sprays.*Int. J. Multiphase Flow*, **30**: 615648.

[31] Hoque, A. 2002, Air bubble entrainment by breaking waves and associated energy dissipation. PhD thesis, Department of Architecture and Civil Engineering. Toyohashi University of Technology, Toyohashi, pp. 151.

[32] Hoque, A. and S. Aoki, 2005, Distributions of void fraction under breaking waves in the surf zone. *Ocean Engineering*, **32**: 18291840.

[33] Horrocks, W.H, 1907, Experiments made to determine the conditions under which specific bacteria derived srom sewage may be present in the air to ventilating pipes, drains, inspection chamber, and sewers.*Proc. R. Soc. London*, **79B**: 255-266

[34] Hwung, H. H., J. M. Chyan and Y. C. Chung, 1992, Energy dissipation and air bubbles mixing inside surf zone. *In 23rd Int. Conf. on Coastal Engineering (ASCE), Venice*, Italy, **1**: 308321.

[35] Inui, T., 1970, Wave patterns and hull forms of ships, JUBILEE Memorial, NSMB.

[36] Inui, T., H. Kajitani and H. Myiata, 1979, Experimental investigation of the wave making in the near field of ships, *Journal of the Naval Architecture of Japan*, **173**.

[37] Jahne, B. and P. Giebler, 1994, Proceedings of the Conference on Computer Vision and Pattern Recongnition, Seattle, 20-23 June.

[38] Jochum, M. and R. Murtugudde, 2006, Physical Oceanography, developing since 1950. Springer. New york.

[39] Kalvoda, P. M., L. Xu and J. Wu, 2003, Macrobubble clouds produced by breaking wind waves: a laboratory study. *J. Geophysical Research*, **108**: 3207.

[40] Kerman, B.R, 1988, Sea surface sound natural mechanisms of surface generated noise in the ocean. Kluwer Academic, 639pp.

[41] Kiger,T. K., 1995, Particle Dispersion and Inter-Phase Kinetic Energy Transfer in a Turbulent Two-Phase Shear Layer, PhD Dissertation, Department of Mechanical Engineering, University of California,San Diego.

[42] Kobus, H. and H.P. Koschitzky, 1991, Local surface aeration at hydraulic structures. In Air entrainment in free-surface flows, IAHR hydraulic structures design manual no. 4, hydraulic design considerations (ed. I. R. Wood), p. 149. Rotterdam, The Netherlands: A. A. BalkemaPublications.

[43] Lamarre, E. and W. K. Melville, 1991, Air entrainment and dissipation in breaking waves. *Nature*, **351**: 469472.

[44] Lamarre, E. 1993, An experimental study of air entrainment by breaking waves. PhD thesis, Department of Civil and Oceanographic Engineering. Cambridge, MA: MIT Press.

[45] Lamarre, E. and W. K. Melville, 1994, Void-fraction measurements and sound-speed fields in bubble plumes generated by breaking waves.*J. Acoust. Soc. Am.*, **95**: 13171328.

[46] Ledesma, R. G. 2004, An experimental investigation on the air entrainment by plunging jets. PhD thesis, Department of Mechanical Engineering, University of Maryland, Maryland, pp. 192.

[47] Leifer, I. and G. De Leeuw, 2006, Bubbes generated from wind-steepened breaking waves: 1. Bubble plumes, and wave characteristics.*J. Geophysical Research*, **111**: C06021.

[48] Leifer, I., G. Caulliez and G. De Leeuw, 2007, Characteristics of bubble plumes, bubble-plume bubbles and waves from wind-steepened wave-breaking..*Journal of Marine systems*, **66**: 61-70.

[49] Lin, J. C. and D. Rockwell, 1994, Instantaneous structure of a breaking waves,*Physics of Fluids*, **6:(9)**: 2877-2879.

[50] Lin, J. C. and D. Rockwell, 1995, Evolution of a quasi-steady breaking waves,*Journal of Fluid Mechanics*, **302**: 29-44.

[51] Loewen, M. R., M. A. ODor and M. G. Skafel, 1996, Bubbles entrained by mechanically generated breaking waves.*J. Geophysical Research* **101**, 20 75920 770. *Journal of Fluid Mechanics*, **302**: 29-44.

[52] Loewen, M. R., M. H. K. Siddiqui, 2006, Detecting microscale breaking waves.*Meas. Sci. Technol.* **17**, 771-780.

[53] Longuet-Higgins, M. S. and J. S. Turner, 1974, An entraining plume model of a spilling breaker,*Journal of Fluid Mechanics*, **63**: 1-20.

[54] Longuet-Higgins, M. S. and 1975, Integral Properties of Periodic Gravity Waves of Finite Amolitude,*Proc. R. Soc. Lond. A*, **342**: 157-174.

[55] Longuet-Higgins, M. S., 1995, On the disintegration of the jet in a plunging breaker, *Journal of Physical Oceanography*, **25**: 2458-2462.

[56] Maxeiner, E., 2009, Physics of Breaking Bow Waves: A Parametric Investigation using a 2D+T Wave Maker, PhD Dissertation, Department of Mechanical Engineering, University of Maryland.

[57] Medwin, H. 1977, In situ acoustic measurements of microbubbles at sea. *J. Geophysical Research*, **82**: 971-976.

[58] Melville, W.K. 1996, The role of surface wave breaking in air sea interaction .*Annual Review of Fluid Mechanics*, **28**: 279-321.

[59] Michell, J. H., 1898, The wave resistance of a ship, *Phil. Mag.*, **45**(5): 106-123.

[60] Miller, N. and R. E. Mitchie, 1970, Measurement of local voidage in liquid/gas two-phase flow systems. *J. Br. Nuclear Energy Soc.*, **9**: 94100.

[61] Miyata, H. and T. Inui, 1984, Nonlinear ship waves,*Advances in Applied Mechanics*, **24**: 215-288.

[62] Miyata, H., 1980, Characteristics of nonlinear wavesin the near-field of ships and their effects on resistance, Proceedings of the 13th Symposium on Naval Hydrodynamics, 335-351. Shipbuilding Research Association of Japan.

[63] Monahan, E.C. 1986, The ocean as a source for atmospheric particles, in The Role of Air-Sea Exchange in Geochemical Cycling, edited by P. Baut-Menard,pp. 129-163, Sprinber, New york.

[64] Monahan, E.C. and M.A. Van Patten, 1989, Climate and health implications of bubble mediated sea air exchange. Connecticut sea grant collage program.

[65] Mori, N., T. Suzuki and S. Kakuno, 2007, Experimental study of air bubbles and turbulence characteristics in the surf zone., *J. Geophysical Research*, **112**: (C05014).

[66] Murzyn, F., D. Mouaze and J. R. Chaplin, 2004, Optical measurements of bubbly flow in hydraulic jumps.*Int. J. Multiphase Flow*, **31**: 141154.

[67] Noblesse, F., D. Hendrix, L. Faul and J. Slutsky, 2006, Simple analytical expressions for the height, location and steepness of a ship bow wave, *Journal of Ship Research*, **50**(4): 360-370.

[68] Noblesse, F., G. Delhommeau, M. Guilbaud, D. Hendrix, L. Faul and C. Yang, 2008, Simple analytical relations for ship bow waves, *Journal of Fluid Mechanics*, **600**: 105-132.

[69] Oguz, H. N., A. Prosperetti and A. R. Kolaini, 1995, Air entrainment by a falling water mass.*Journal of Fluid Mechanics*, **294**: 181207.

[70] Olivieri, A., F. Pistani, R. Wilson, E. F. Campana and F. Stern, 2007, Scars and vortices induced by ship bow and shoulder wave breaking, *Journal of Fluids Engineering*, **129**: 1445-1459.

[71] Pletzer, R.D. 1984, White water wake characteristics of surface vessels. NRL Memorandum report 5335. Naval research laboratory, Washington, D.C.

[72] Peregrine D. H. and I. A. Svendsen, 1978, Spilling breakers, bores, and hydrolic jumps, 16th International Conference on Coastal Engineering, Hamburg, New York, Aug. 27-Sep. 3, pp. 540-550.

[73] Prosperetti, A. and H. N. Oguz, 1997, Air entrainment upon liquid impact. *Phil. Trans. R. Soc. Am.*, **355**: 491506.

[74] Roth, G. L., D. T. Mascenik and J. Katz, 1999, Measurements of the flow structure and turbulence within a ship bow wave, *Physics of Fluids*, **11(11)**: 3512-3523.

[75] Sarpkaya, T. and P. Suthon, 1991, Interaction of a vortex couple with a free surface, *Experiments in Fluids*, **11**: 205-217.

[76] Serdula, C. D. and M. R. Loewen, 1998, Experiments investigating the use of fibre-optic probes for measuring bubble-size distributions. *IEEE Journal of Oceanic Engineering*, **23**: 385399.

[77] Shakeri, M., 2005, An experimental 2D+T investigation of breaking bow waves, PhD Dissertation, Department of Mechanical Engineering, University of Maryland.

[78] Shakeri, M., M. Tavakolinejad, and J. H. Duncan, 2009, An experimental examination of divergent bow waves, *Journal of Fluid Mechanics*, **634**: 217-243.

[79] Shakeri, M., E. Maxeiner, T. Fu and J. H. Duncan, 2009, An experimental examination of the 2D+T approximation, *Journal of Ship Research*, **53**: 59-67(9).

[80] Siddiqui, M. H. K., M. R. Loewen, W. E. Asher and A. T. Jessup, 2004, Coherent structures beneath wind waves and their influence on air- water gas transfer. *J. Geophysical Research*, **109**, C3, C03024.

[81] Stokes, M. D. and G. B. Deane, 1999, A new optical instrument for the study of bubbles at high void fractions within breaking waves, *IEEE Journal of Oceanic Engineering*, **24(3)**: 300-311.

[82] Stokes, G. G., 1847, On the theory of oscillatory waves, *Trans. of the Cambridge Philosophical Society*, **8**: 441.

[83] Stokes, G. G., 1880, Consideration relative to the greatest height of oscillatory irrotational waves which can be propagated without change of form,*Mathematical and Physical Papers*, **1**: 225-228, Cambridge University Press.

[84] Tulin, M. and M. Wu, 1997, Divergent Bow Waves, *Proceedings of the 21st Symposium on Naval Hydrodynamics*, Trondheim, Norway, 661-679.

[85] Vagle, S. and D. M. Farmer, 1998, A comparison of four methods for bubble size and void fraction measurements. *IEEE IEEE Journal of Oceanic Engineering*, **23**: 211222.

[86] Waniewski, T., C. Brennan, and F. Raichlen, 1997, Experimental simulation of a bow wave, Proceedings of FEDSM 2007, ASME Joint U.S.-European Fluids Engineering Summer Meeting, June 22-26, 2006.

[87] Waniewski, T., 1999, Air entrinment by bow waves,PhD Dissertation, Division of Engineering and Applied Science, California institute of Technology.

[88] Waniewski, T., C. Brennan, and F. Raichlen, 2001, Measurements of air entrainment by bow waves,*Journal of Fluids Engineering*, **123**: 57-63.

[89] Waniewski, T., C. Brennan, and F. Raichlen, 2002, Bow wave dynamics, *Journal of Ship Research*, **46(1)**: 1-15.

[90] Wildt, R., 1946, Acoustic theory of bubbles, *Physics of Sound in Sea*, **8**: Department of Defense 546 pp.

[91] Zappa,C. J., W. E. Asher, A. T. Jessup, J. Klinke and S. R. Long, 2004, Microbreaking and the enhancement of air- water gas transfer velocities.*J. Geophysical Research*, **109**, C8, C08S16.